Spring 2019

Heterogeneous Catalysis for the Upgrading of Biomass Derived Chemicals via Hydrodeoxygenation

Elizabeth Barrow

HETEROGENEOUS CATALYSIS FOR THE UPGRADING OF BIOMASS DERIVED CHEMICALS VIA HYDRODEOXYGENATION

by

Elizabeth Barrow

Bachelor of Science
Charleston Southern University, 1998

Master of Science
University of Miami, 2000

Submitted in Partial Fulfillment of the Requirements

For the Degree of Doctor of Philosophy in

Chemical Engineering

College of Engineering and Computing

University of South Carolina

2019

Accepted by:

Jochen Lauterbach, Major Professor

Andreas Heyden, Committee Member

John Regalbuto, Committee Member

Donna Chen, Committee Member

John Weidner, Committee Member

Cheryl L. Addy, Vice Provost and Dean of the Graduate School

DEDICATION

This work is dedicated to my boys, Shedrick and William. May they see the importance of education, the benefit of hard work, and the strength that comes from a family's love.

ACKNOWLEDGEMENT

I am extremely grateful to my PhD advisor Jochen Lauterbach. He accepted me into his research group believing that I had potential. Considering that this course of study was a completely new field to me, it could not have been an easy task for him to give me the time and resources to learn to be an engineer. Without his continued patience, I would not have been able to proceed through this transition to engineering.

Practically adopting me for 7 months, Kiyotaka Asakura welcomed me into his group for my internship at Hokkaido University. I am grateful to him and his group for not only teaching me the delicate ways of surface science but also making certain that my family adapted to life in Japan. He, Miwa-san, and Hamigami-san, constantly stood in the gap for my boys. They even made it possible for my older child to attend snow camp!

I would also like to thank members of SAGE, both past and present. Entering the laboratory with no research experience meant that I had a great amount to learn. The members of SAGE that were there when I started guided me in learning the basic skills of chemical hygiene and the use of the analytical equipment. They began the work of helping me to think and present as an engineer. The current SAGE members are also important to me. New talent brings new ways of thinking, and I have learned vital lessons from each and every one of my group mates.

A special thanks is given to my family and friends. Words cannot possibly describe the sacrifices they have made for me or the support they have given.

ABSTRACT

An important step in the upgrading of biomass derived chemicals is the removal of excess oxygen. The works reported here are focused on studying the heterogeneous catalysts that can be utilized for that upgrading through hydrodeoxygenation. This work begins with a discussion of the alkylation of short chain platform chemicals for chain growth and also demonstrates the proof of concept of combining alkylation and hydrodeoxygenation in a single step. Then, because of the promising nature of ReO_x-Pd/CeO_2 for selective hydrodeoxygenation, a detailed study of ReO_x/CeO_2 is presented. Finally, a new surface structure interpretation is presented for P/Ni(111) which could be used for understanding Ni_2P, a catalyst used for hydrodeoxygenation.

First, the production of long-chain hydrocarbons (C8+) from 2-methylfuran(2MF) and butanal in a single step reactive process is demonstrated by utilizing a bi-functional catalyst with both acid and metallic sites. A solid acid, Al-MCM-41, is utilized for the alkylation function and as a support for the transition metal, Pt. The Pt/Al-MCM-41 catalyst showed 96% yield for C8+ hydrocarbons, and the catalytic performance was stable over four reaction cycles of 20 hours each. The oligomerization of 2MF is also studied over solid catalysts. An aluminosilicate catalyst with Si/Al=20 is developed that demonstrates 40% conversion of 2MF in a pressurized batch reactor. This produces a mix of carbohydrates with the major components being the 2MF trimer and tetramer.

Both the tetramer and the trimer are known to perform well under hydrodeoxygenation to form C15 and C20 hydrocarbons.

Second, to lead towards an explanation of the unique catalytic activity of ReO_x-Pd/CeO_2 for simultaneous hydrodeoxygenation of vicinal OH groups, the structure of ReO_x/CeO_2 is compared to the structure of ReO_x on other oxides. Though the ReO_x surface structure has been well characterized on SiO_2, Al_2O_3, ZrO_2 and TiO_2 supports, the ReO_x surface structure on CeO_2 has not been rigorously studied. Several catalytic characterization techniques for structural determination are employed. It has been discovered that the structure of ReO_x supported on CeO_2 is unlike any previously studied supported ReO_x. One of the main differences is that ReO_x is chemisorbed on the surface of CeO_2 in ambient conditions instead of being hydrolyzed by surface water. Additionally, instead of vaporizing as is commonly reported, it is shown that with high loadings of ReO_x, crystalline Re_2O_7 is formed and remains on the surface even after calcination at 500^{o}C. When ReO_x is supported on an oxide, crystalline Re_2O_7 has never before been reported. It is shown that with the lowest loadings studied, 0.5wt%Re, Re has a +VII oxidation state, and ReO_x is present with both tetrahedral and octahedral coordination. Using an $^{18}O_2$ isotope exchange, it is shown that the tetrahedrally coordinated portion of ReO_x/CeO_2 has a single terminal oxygen. Upon reduction with H_2, the octahedrally coordinated portion of ReO_x reduces at a lower temperature than the tetrahedrally coordinated portion.

Lastly, a surface science study using LEED interpretation of phosphorous dosed on a Ni(111) single crystal is presented. A phase diagram of the surface P adsorbed on Ni(111) is developed showing distinct overlayer structures based on loading and

annealing temperature. At low coverage, amorphous P was observed. At annealing temperatures below 400°C and coverages above 0.1 ML, a $\sqrt{7}x\sqrt{7}R19.1$ structure was observed. Above 400°C, another complex structure was created. These structures seemed to correlate with each other and the $\sqrt{7}x\sqrt{7}R19.1$ structure of P adsorbed on Ni(111) is therefore reinterpreted to have a rectangular unit cell. The new rectangular structure is discussed in relation to the Ni_2P local structure.

TABLE OF CONTENTS

LIST OF TABLES

LIST OF FIGURES

List of Abbreviations

2MF 2-methylfuran

AES ..... Auger Electron Spectroscopy

ARUPS ..... Angle Resolved Photoelectron Spectroscopy

BE ..... Binding Energy

BET ..... Brunauer-Emmett-Teller

BJH ..... Brunauer-Joyner-Halenda

BUT ..... Butyraldehyde

CCD ..... Charge Coupling Device

DFT ..... Density Functional Theory

DI ..... De-Ionized

DRIFTS ..... Diffuse Reflectance Infrared Fourier Transform Spectroscopy

EDS ..... Energy Dispersive X-ray Spectroscopy

EXAFS ..... Extended X-ray Absorption Fine Structure

FID ..... Flame Ionization Detector

FTIR ..... Fourier Transform Infrared Spectroscopy

FWHM ..... Full-Width-Half-Max

GC ..... Gas Chromatography

HDO ..... Hydrodeoxygenation

HDTMACl ..... Hexadecyl Trimethyl Ammonium Chloride

HPLC ..... High Performance Liquid Chromatograph

ICP-OES ..... Inductively Coupled Plasma Optical Emission Spectrometry

KE ..... Kinetic Energy

LEED ..... Low-Energy Electron Diffraction

MBA 2-methyl-2-butanol

MBE 2-methyl-2-buten-2-ol

MBY 2-methyl-3-butyn-2-ol

ML ..... Mono Layer

MS ..... Mass Spectroscopy

NMR ..... Nuclear Magnetic Resonance

NPT ..... National Pipe Tapered

PID ..... Proportional Integral Derivative

PTFE ..... Polytetrafluoroethylene

RPM ..... Revolutions Per Minute

SEM ..... Scanning Electron Microscopy

SS ..... Stainless Steel

STM ..... Scanning Tunneling Microscopy

TCD ..... Thermal Conductivity Detector

TDS ..... Thermal Desorption Spectroscopy

TEAOH ..... Tetraethyl Ammonium Hydroxide

TEM ..... Transmission Electron Microscopy

THF ..... Tetrahydrofuran

TMACL ..... Trimethyl Ammonium Chloride

TPD ..... Temperature Programmed Desorption

TPR ..... Temperature Programmed Reduction

UHV ..... Ultra-high Vacuum

XAFS ..... X-ray Absorption Fine Structure

XANES .....X-ray Absorption Near Edge Structure

XPS ..... X-ray Photoelectron Spectroscopy

XRD ..... X-ray Diffraction

CHAPTER 1

OVERVIEW

A catalyst is a substance which is neither consumed nor permanently changed in a chemical reaction but increases the rate of that chemical reaction[1]. A heterogeneous catalyst is one in which the catalyst phase is different from that of the reactants. The majority of heterogeneous catalysts are solids used with liquid or gas reactants[2]. On a solid surface, reactants adsorb and an intermediate or series of intermediates are formed on the surface[3]. The final product then desorbs. These heterogeneous catalysts may lose activity through coking, sintering, and poisoning[4]. Heterogeneous catalysis is greatly important as is seen by their use in the works of Nobel prize winners Fritz Haber, Carl Bosch, Irving Langmuir, and Gerhard Ertl [5]–[8]. Today, heterogeneous catalysis is widely used in industry due to the fact that it can be easily separated from the reaction products. Herein, I will discuss a couple of the specific uses of heterogeneous catalysts and the work that I have done.

1.1 Long chain hydrocarbons for transportation fuel

Currently, the US imports about 10 million barrels of crude oil per day.[9] Of the nearly 20 million barrels of crude used daily in the US, 72% is used for transportation, over 7 billion barrels per year. [10] Though it may not be enough to eliminate imports, using transportation fuels derived from biomass can decrease our nation's dependency on imported oil [11]. Skeptics are concerned that biomass derived fuels will cause land use

change that competes with crop land for food production. If transportation fuels are developed from biomass that is currently considered waste, it will not compete with food. Furthermore, the use of waste biomass can assist in closing the CO_2 cycle [12]. The U.S. Billion Ton Update [13] reports that over 400 million dry tons of biomass waste is available each year. This has the annual energy equivalence of over a billion barrels of oil [14].

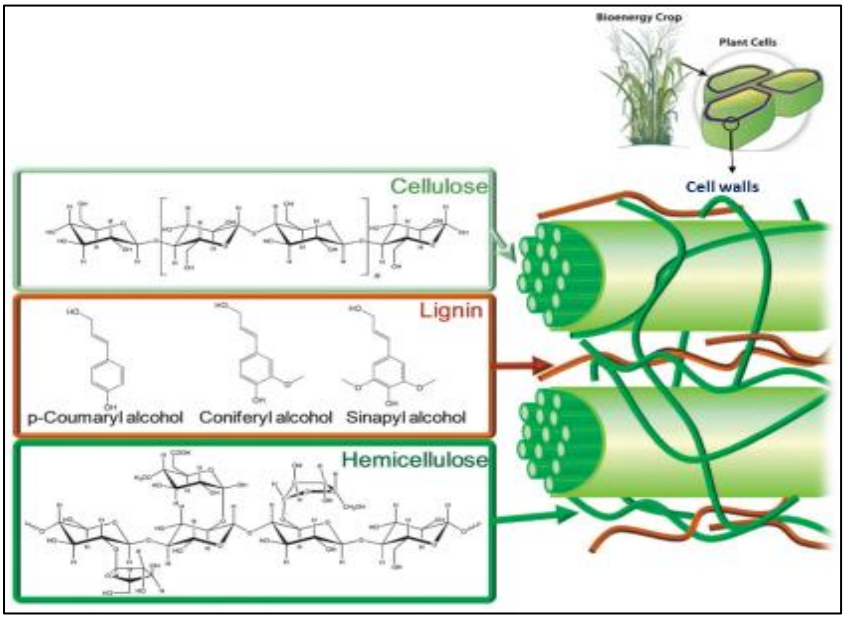

Figure 1.1 Primary Composition of Plant Cell Wall adapted from [15].

Raw biomass is composed primarily of cellulose, hemicellulose, and lignin (See Fig 1.1) [15]. Cellulose, 22-55 (dry wt.)% of biomass, is a well ordered polymer of the C6 sugar glucose. Lignin, 7-35% of biomass, is the polymer credited for allowing plants to support themselves. Hemicellulose, making up the remaining 15-40% of biomass, is an assortment of polymers of C5 and C6 sugars with a low degree of polymerization (Ca. 200) [16]. The exact ratio of pentose to glucose found in the hemicellulose varies by plant [17]. Waste biomass is predominantly barky material that tends to have high percentages

of hemicellulose (40 dry wt %) [18]. The hemicellulose found in barky material has a relatively large pentose to hexose ratio compared to the hemicellulose in soft wood (See Fig.1.2) [17].

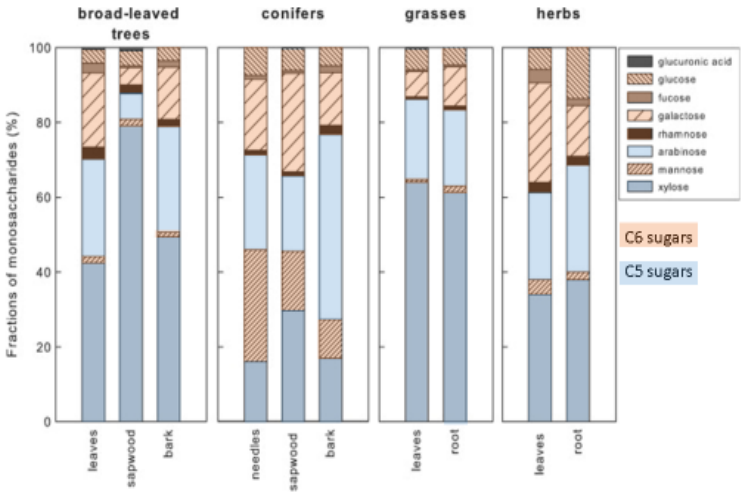

Figure 1.2 Composition of hemicellulose in various biomass, adapted from [17].

Of possible paths to alkane crude substitutes, chemical dissolution is the preferred treatment for hemicellulosic material when compared to pyrolysis or gasification. The process conditions of pyrolysis break some of the C-C bonds found in plants resulting in 45% heat loss from the biomass [19], and gasification breaks all C-C bonds resulting in 50-60% energy loss for fuels made through Fischer-Tropsch [20]. Through hydrothermal dissolution, raw biomass can be separated into cellulose, lignin and hemicellulose streams allowing for them to be processed individually [21], [22]. Cellulose can be fermented to ethanol to assist in meeting the U.S. ethanol demand of over 5 billion gallons a year [23]. Lignin, though highly valued for epoxy and fine chemicals [24], can be burned for process heat. Hemicellulose, due to its inconsistent nature, is traditionally wasted in biomass fuel production [25].

To increase fuel yield from biomass, a scalable fuel-related use of the C5 sugars from hemicellulose must be developed. Much research has already been devoted to the conversion of C5 sugars to platform chemicals such as furfural and 2-methylfuran. Since 1921, Furfural has been produced in batch reactions catalyzed by aqueous sulfuric acid. Quaker Oats developed the process, still in use today, in which oat hulls are cooked through a flow of steam at 153^{o}C for 5 hours resulting in 53% theoretical yield. It has recently been demonstrated on lab scale that furfural can be produced in a continuous reaction at 98% yield. This is done in a two-liquid-phase (aqueous toluene) reactor over mordenite and requires 260^{o}C and 55 ATM [26]. Furfural in toluene can be hydrogenated in a gas-phase reaction at 252^{o}C over Cu/Fe catalyst to produce 2-methylfuran with 98% yield [26]. Utilizing methods to convert 2- methylfuran or other high yield pentose derived platform chemicals into fuels or fuel additives would increase the overall fuel yield from biomass.

Long chain hydrocarbons can be synthesized from biomass platform chemicals such as furfural or 2-methylfuran (2MF). Recent studies have shown that long chain hydrocarbons, C9-C35, derived from biomass can be used as a replacement for crude oil in fuel refineries [27]–[29]. Biomass derived long chain hydrocarbons are stable enough to be piped to refineries and mixed directly with the refinery's feedstocks as "drop-in" replacements to then be refined into fuels that meet the various standards of their locality. Light crude oil feedstocks consist of C9-C25 while heavy crude oil feedstocks consist of C15-C35 [27], [30]. Due to the overlap in light and heavy crude oil feedstocks, C15-C25 hydrocarbons are versatile enough to be used as feedstocks for either stream.

To convert C5 platform chemicals into long chain hydrocarbons, the carbon backbone must be increased in length through addition reactions of the platform chemicals to create a precursor carbohydrate with the desired quantity of carbons. Then, through hydrogenation and hydrodeoxygenation (HDO) of the carbohydrate, long chain hydrocarbons are produced [31]–[34]. Many researchers have reported alkane production of predominantly C9-C16 using processes that require solvents and involve two distinct reactors for carbohydrate formation, and hydrogenation/hydrodeoxygenation [34]–[37]. Some researchers reported processes requiring a third reactor by performing the hydrogenation and hydrodeoxygenation steps separately [27], [38]. Huber et al. [27] reports the ability to tune his alkane production to produce hydrocarbon mixes up to C31, but this requires tedious steps including a week long chilled aging step between reactions. Utilizing multiple steps for long chain alkane production will lead to expensive scale up processes due to the multiple reactors.

Lab scale carbohydrate formation from carbon chain growth reactions of C5 platform chemicals such as furfural or 2MF has been widely reported [34], [35], [37], [39]–[41], but the reported processes are not easily scalable. Such processes often require high levels of dilution and the use of corrosive chemicals. For example, Huber et al. [27] uses aldol condensation of furfural and acetone in a 2:1 ratio to produce a C15 precursor at 96% yield. This reaction requires furfural, acetone, tetrahydrofuran (THF) water and NaOH with an organic:aqueous ratio of 5.1:1. The furfural-acetone-furfural (FAF) condensation product is solid at room temperature, so it must remain in the THF until after further processing. When developing a plan to use this method for the treatment of hemicellulose in the pilot scale production of transportation fuels from biomass, the

authors comment that the water treatment required for this step is a large amount of the cost [41]. From the chemical process standpoint, carbohydrate formation would be more scalable if it required little or no dilution and used a heterogeneous catalyst.

Corma et al. [37] demonstrates that a variety of diesel precursors can be produced from 2-methylfuran and either an aldehyde or ketone using either homogenous or heterogeneous acids catalysts. A thorough catalyst screen for the alkylation of 2-methylfuran with butanal was performed. A 98% yield of 1,1-bissylvylbutane was achieved with high dilution of hydrochloric acid, but the authors acknowledge that the high dilution would not be feasible for industrial use. In an attempt to use less water, concentrated hydrochloric acid was tested in the reaction, resulting in a drop of yield to 73%. In an effort to conform this reaction to industrial requirements, solid acids were screened. Zeolite Beta and zeolite Y were chosen for being strong acid zeolites. By adjusting the Si:Al ratios, it was found that lowering the aluminum content increased conversion. As zeolite beta has a pore size close to that of 1,1- bissylvylbutane, the pore size of the zeolite beta was increased in an attempt to improve accessibility of the acid sites resulting in increased conversion. This led to testing Al-MCM-41 for its large pore size, but found lower conversion due to the lower acid strength of the catalyst. Lastly, ITQ-2, a delaminated zeolite, was tested and found that the combination of site accessibility and acid strength contributed to a 90% yield. In further attempts to perform carbon chain growth with an easily scalable method, the Corma group studied the trimerization of 2-methylfuran, because removing the need for the addition of an aldehyde or ketone would remove a process step. This trimerization precursor was obtained with 75% yield using sulfuric acid as the catalyst and 38% water by mass.

However, since sulfuric acid is a homogeneous catalyst that requires a batch reaction process, it is a technical barrier for large scale fuel production compared with a continuous fixed bed reaction, and it also increases the cost due to the separation and hazardous waste handling.

To augment the work reported by the Corma group, Yati et. al. [42] screened solid acids for the 2-methylfuran trimerization. It was reported that using solid acids in 3 hour, 85°C, batch reactions with 2-methylfuran produced both the 2MF trimer and its tetramer. A simultaneous study was performed on the addition of water to effect selectivity. Without water, catalyzing 2MF with Amberlyst-15, Nafion-NR50, and Nafion-SAC-13, produced 5%, 17%, and 2% selectivity to the trimer with 38%, 43%, and 42% conversions respectively. With the addition of 15 wt% water, the trimer selectivity increased to 91%, 42%, and 22% respectively, but the conversions dropped to 12%, 20% and 18%. Though this was a study to improve the scalability of the trimerization of 2MF, the scalability of the overall process of converting to alkanes was disregarded. The low thermal stability of Nafion restricts its use to the precursor formation step. To further improve the industrialization ability of these reactions, a catalyst should be chosen that is capable of withstanding hydrodeoxygenation temperatures (at least 170^{o}C [36]) so that these steps can be combined. Therefore, it is in the best interest of future process improvements to study the selectivity of thermally stable solid catalysts for precursor formation.

After carbon chain growth, the resulting precursors have double bonds and oxygen that must be removed through hydrogenation and hydrodeoxygenation to form alkanes of suitable length for crude oil substitution. Li et al [38] studied the

hydrogenation and hydrodeoxygenation of a C15 precursor containing 3 furan rings. First the carbohydrate was hydrogenated, and then the hydrodeoxygenation was performed using 4% Pt on four acid supports: SiO_2, Nb_2O_5, SiO_2-Al_2O_3, and ZrP. Reactions were performed in a fixed bed reactor at 350^oC with a liquid feedstock flow rate of 0.02 mL/min and H_2 flow rate of 60 mL/min. Pressure was not reported. Monitoring the exit gas of the reactor, no CO_2 or CO was detected with any of the reactions and all of the liquid products were fully deoxygenated. It was found that ZrP is the best support for maintaining the carbon length as it produced 50% more C15 than the other catalysts. This is attributed to either the high Brønsted:Lewis ratio of ZrP or to the fact that the average particle size of the Pt on the ZrP was higher than that of the Pt on the other supports.

Chemical dissolution of biomass and separation of hemicellulose followed by carbon chain growth and the hydrogenation and hydrodeoxygenation of the hemicellulose derived chemicals is a proven path to synthetic diesel length alkanes [31], [43] which can be used as crude oil substitutes [21], [28], [30]. However, there are common concerns about this process of chemical dissolution, carbon chain growth, hydrogenation and hydrodeoxygenation for alkane production from hemicellulose. These concerns include the number of process steps from biomass to alkanes and the vast volume of water or other solvents required. Many such processes require 3 separate steps for carbon chain growth, hydrogenation and hydrodeoxygenation plus separation steps between them. Recent studies have shown that the carbon chain growth of hemicellulosic derived platform chemicals can be performed in solvent free conditions with solid acids; however, little has been done to reduce the solvents required in the hydrodeoxygenation step.

The work in this thesis discusses the use of biomass derived chemicals including 2MF to produce C8+, 72% nonane, in a single, solvent free, fixed bed reactor.[43] Producing C8+ in a single continuous step showed that chain growth and HDO can be performed in a scalable fashion. This process is scalable by being a continuous, solvent free reaction making this a successful proof of concept. The C8+ alkanes are not long enough to be considered a crude substitute[30], but they are of suitable length to be added to the light crude oil processing at a refinery. In an attempt to build on this concept, a screening was performed to choose a potential bifunctional catalyst and reactants for the single step, continuous reactor that would produce longer hydrocarbons. Focus is then given to a catalytic study for the oligomerization of 2MF. Included are a catalyst screening followed by optimization of an aluminosilicate for the production of the 2MF trimer and tetramer. Initial results from a high pressure batch reaction show the feasibility of using 2MF for single step production of a crude replacement.

1.2 Selective vicinal hydrodeoxygenation

An important step in the conversion of biomass derived chemicals to fuels and value added chemicals is the removal of excess oxygen atoms. Recent studies have focused on the selective hydrodeoxygenation (HDO) of vicinal OH groups, such as those found in xylitol as well as other sugar alcohols [44]–[48] . Specifically, interest has been focused on the bifunctional catalysts comprised of an oxophilic promoter and a highly reducible metal over reducible metal oxide, ReO_x-Pd/CeO_2.[44], [49], [50] This practice of removing vicinal pairs of alcohol groups allows for more control of reaction products over HDO of single alcohol groups. ReO_x-Pd/CeO_2 is known to be effective for the HDO of vicinal OH groups with reported yields as high as 99% in the batch production of

tetrahydrofuran (THF) from 1,4-anhydroerythritol. ReO_x-Pd on oxides other than CeO_2 have been reported to be drastically less effective[44], [51].

Noticing the potential of simultaneous HDO, work was begun to confirm literature reports by first building the batch reactor detailed in section 2.2.2.3. Then the model reaction of THF to 1,4-anhydroerythritol was confirmed. In the initial studies to optimize the THF model reaction, a colleague, Blake MacQueen, noted that within his condition set the simultaneous HDO had a zero-order dependence on pressure. The simplicity of the THF reaction does not provide confirmation of literature reports that ReO_x-Pd/CeO_2 removes vicinal OH groups in pairs. However, monitoring the various products of the HDO of xylitol and using the knowledge that pressure dependence was zero order for the THF study, it was shown that the predominant products are formed from simultaneous HDO and scalable conditions were found for value added products. Through the selective partial deoxygenation of xylitol ($0.15/g) products are formed that are drastically value added such as 1,2,5-pentanetriol ($47/gram) and 1,2-dideoxypentitol ($800/g). Details of this study can be found here [52].

1.3 Fundamental studies of supported Rhenia

ReO_x on Ceria has been reported to be more active for simultaneous hydrodeoxygenation of hydrocarbons than ReO_x on other supports [44], [51]. Though this benefit could simply be from the oxygen storage properties of the support or from the PdO crystallite size, it is natural to presume that this could be the result of a structural difference of the ReO_x when supported on the cubic fluorite CeO_2. [53] The structure of ReO_x on other supports has been widely studied, but the structural determination of ReO_x on Cerium Oxide has scarcely been studied. Recently a DFT study was performed on

ReO_x/CeO_2 using a fully hydroxylated support surface.[54] DFT calculations show that, at elevated temperatures in hydrogen atmosphere, the ReO_x has a tridentate structure with one terminal Re=O bond. At temperatures below 100°C, it was shown that the most stable species has a hydroxyl site. Raman peeks at 972, 882 and 830 cm^{-1} for calcined 2 wt% ReO_x/CeO_2 have been reported[51], but the peak assignments were incomplete. To make a comparison of the structure of ReO_x on CeO_2 vs other supports, a more thorough study of ReO_x/CeO_2 is needed.

1.3.1 Rhenia Reference Species

Reference spectra of unsupported Rhenia species can be useful for understanding bands of supported Rhenia. Original works used here include the vibrational spectra for Re_2O_7 vapor [55] and that of $NaReO_4$[56]. Other references are found summarized and compiled in works that report the structure of ReO_x on other supports [57], [58]. ReO_4^- has C4 symmetry with 3 Raman peaks[58]. The symmetric stretch is found at 971 cm^{-1}. The antisymmetric stretch is found at 916 cm^{-1}, and two bending modes are both at 332 cm^{-1}. The distorted tetrahedron found in $NaReO_4$ has two antisymmetric bands at 928 cm^{-1} and 890 cm^{-1}[56]. The bending modes for the distorted tetrahedron are at 369 cm^{-1} and 331 cm^{-1}. Gas phase Re_2O_7 has symmetric peak at 1009 cm^{-1}, antisymmetric peak at 972 cm^{-1}, a small bending Re-O-Re band at 456 cm^{-1} and bending modes at 341 cm^{-1} and 185cm^{-1} [55]. Crystalline Re_2O_7 is composed of both octahedral ReO_6 and tetrahedral ReO_4[57], [58]. The units are linked by oxygen bridges in a double layer structure. The weak van der Waals forces between the layers produce the complicated spectral pattern.[57]

1.3.2: Studies of Rhenia supported on Al_2O_3, ZrO_2, TiO_2, and SiO_2

The importance of drying samples *in situ* for Raman and IR was discussed by Vuurman et al. with a study presenting the structure of Rhenium oxide on various oxide supports including Al_2O_3, ZrO_2, TiO_2 and SiO_2. [58] Surface structure determinations were made solely on the characterization techniques of Raman, IR, and TPR. For ambient conditions on all supports, Raman spectra were similar to that of aqueous perrhenate ions. For alumina, 3 peaks were observed at 982, 920, and 332 cm^{-1} which were assigned to the symmetric, anti-symmetric, and bending modes respectively. The other supports had bands around 330 cm^{-1}, so the rhenium oxide bending mode could not be observed. These observed rhenium oxide peaks were independent of coverage. It is reported that due to the surface water in ambient conditions, the surface rhenium oxide species are practically in aqueous medium.

Upon dehydrating the samples for 30 minutes at 450^oC, the symmetric Re=O band shifts to slightly higher wave number and an 885-890 antisymmetric band becomes apparent for Al_2O_3 and ZrO_2. Also of importance is the fact that higher Re loadings result in a second surface species for all of the reported supports. This second species is attributed to a second isolated ReO_4 that is adsorbed to a different support site than the first. This article emphasizes the importance of having a dry sample to see loading effects. It also discusses the use of Raman and IR together to aid in elucidating surface species and discusses that bands will split as symmetry decreases. IR spectra in ambient conditions are not reported, and the author discusses that the Re=O symmetric stretch would not be active in IR until the ReO_x had adsorbed to the surface.

For all of the supports studied, the reduction temperature of the rhenia decreased with increased loading. Though multiple species were identified through spectroscopy, all samples had single TPR peaks. The reduction temperature of the single peak decreased with loading. The decreased reduction temperature was used as confirmation that higher Re loadings require that the ReO_x attach to weaker sites. The fact that a single peak was observed is attributed to auto-catalytic reduction of ReO_x. In other words, the reduction of any ReO_x induces the reduction of all the other.

1.3.3 Isotopic studies of ReO_x/ZrO_2 and ReO_x/Al_2O_3

Isotopic labeling studies were performed on supported ReO_x/ZrO_2 by Weckhuysen et al [59] and also on ReO_x/Al_2O_3 by Lwin et al. [60]. The study reported on ZrO_2 included several transition metal oxides supported on ZrO_2. Here, 3wt% ReO_x was used. Pretreatment for Raman spectroscopy included heating in the cell at 550^{o}C for 2 hrs in flowing oxygen. Samples were then subjected to cycles of reduction and reoxidation with $^{18}O_2$ at 450^{o}C. After each reduction, the Raman spectra was featureless. Cycles continued until the reoxidized spectra allowed clear distinction of the isotope substituted bands. The results showed that the non-substituted peaks at 1000cm^{-1} and 890cm^{-1} decreased in area consistent with the area of new peaks at 945cm^{-1} and 840cm^{-1}. It was concluded from this information that only one terminal oxygen band was present. Had two terminal oxygens been present on one Re, the result would have included 2 new peaks: one for the exchange of one oxygen, and also a band for the exchange of both oxygens. Likewise, a trioxo species would have formed 3 new bands: the substitution of 1 oxygen, the substitution of 2 oxygens, and the substitution of all 3. The band at 1000cm^{-1} was observed in both Raman and IR and was assigned to the symmetric stretch

of the terminal oxygen. The band at 890cm^{-1} was observed in Raman but not in IR and was assigned to the cross-linkage of Re-O-Re in Re_2O_7. Had the 890 cm^{-1} peak belonged to an anti-symmetric stretch, it would have been more pronounced in IR.

The isotopic study reported by Lwin et. al. [60] was specifically focused on the surface ReO_x sites on Al_2O_3. In addition to Raman of isotope exchanged samples, the authors employ the experimental techniques of UV-vis, XANES and EXAFS, in situ Raman and IR. The experimental data is compared with theoretical data and it is concluded that ReO_x/Al_2O_3 has two terminal Re=O bonds and two Re-O-Al bonds.

In situ Raman and DRIFTS were performed on dehydrated catalysts. The catalysts were dried in O_2 at 600^{o}C for Raman and 500^{o}C for DRIFTS. Spectra for Raman were taken between 100-200^{o}C, while spectra for DRIFTS were reported at mostly 200^{o}C. These temperatures were considered low enough to reduce fluorescence in Raman and spectral thermal broadening in DRIFTS. For low Re coverage (<5%) the Raman possessed peaks at 1002, 970, 879, and 340cm^{-1}. These were assigned to Vs(Re=O), Vas (Re=O), Vs(Re-O-AL), and δ(O-Re-O) respectively. The higher loading samples had additional peaks at 1012 cm^{-1} and 976 cm^{-1} which are attributed to a second surface rhenia species. The absence of Re-O-Re bands support that these are isolated rhenia species. It is reported here that using 15% Ta_2O_5/Al_2O_3 as a support blocks formation of the first rhenia species to have samples that contain only the second species. These samples were used in catalytic studies to aid in the selection of the active species. Due to support interference, DRIFTS spectra of the Re=O bands were only available in the overtone region. The Vs and Vas peaks of the first species were observed at 1996cm^{-1} and 1962cm^{-1}. The second species were observed at 2020cm^{-1} and 1971cm^{-1}. The *in*

situ IR was also used to study the surface hydroxyls. It was observed that with low loadings, the μ1 hydroxyls are consumed. As Re coverage increases and the μ1 hydroxyls are no longer available, additional hydroxyls are consumed. This is used to support the theory of multiple ReO_x species. No new peaks in the hydroxyl region were formed with increased ReO_x loading.

The isotope study was performed with $H_2{}^{18}O$. After the sample was dried, the water isotope was injected into a flow of 10% $^{16}O_2$/Ar. The $^{16}O_2$ was said to minimize sample darkening. The sample sell was maintained at 200^{o}C and all lines were heated to 150^{o}C. As with the study of ReO_x/ZrO_2[59], the formation of new peaks was observed. For both surface species, the Vs band split into 3 bands which is consistent with a dioxo species. The new peak formation from the Vs(Re-O-Al) peak at 880 cm^{-1} did not provide usable information because the 880 cm^{-1} became too week to see.

In this thesis, the structure of ReO_x/CeO_2 is discovered to change with both temperature and loading. ReO_x has unique characteristics when supported on CeO_2 including that it is not hydrolyzed in surface water in ambient conditions and that agglomerations of ReO_x form with high Re loadings. These characteristics and others are discussed here-in with the use of XRD, FTIR, Raman, TPR and XPS. An oxygen exchange with $^{18}O_2$ is used with 2 loadings of Re to assist in assigning of the structure.

CHAPTER 2

CHARACTERIZATION TECHNIQUES AND EXPERIMENTAL SETUP

Over the course of this work, several techniques and various equipment were utilized to characterize catalysts, run reactions and analyze reaction results. To understand the whole process and draw meaningful conclusions, it is important to understand the methods used to gather data. Hence, descriptions and relevant explanations are provided here. First, techniques used to characterize catalysts will be summarized. Next, the reactors used to compare catalyst activity will be described in detail. Lastly, the techniques used to analyze reaction products will be explained. As some of these techniques and equipment are used with more than one method, project specific details will be described in the relevant project chapters.

2.1 Catalyst characterization techniques

2.1.1 Powder X-Ray Diffraction, XRD

XRD was utilized to identify or confirm the crystal structure and grain size of the crystallites present in the catalysts. A Rigaku MiniFlex II powder X-ray diffractometer was used to record the XRD patterns. It was equipped with a silica strip D/teX Ultra detector with Cu Kα radiation source (λ=1.54Å). The instrument was calibrated weekly using a Si crystal.

XRD is a bulk technique in which a tungsten filament emits monochromatic X-rays onto a sample. When the X-rays strike the sample, they are diffracted from adjacent

crystallite planes. The angle between the sample and the detector is changed. When the angle is such that the distance between adjacent lattice planes has a pathlength that is a multiple of wavelength λ, the diffraction will be constructive. This is referred to as Bragg diffraction, illustrated in Fig 2.1. This relationship between wavelength λ, angle of incidence θ, and distance between lattice planes d is described by Bragg's Law, equation 2.1. When the angle of incidence is such that constructive interference is detected, a peak is recorded in the XRD pattern.

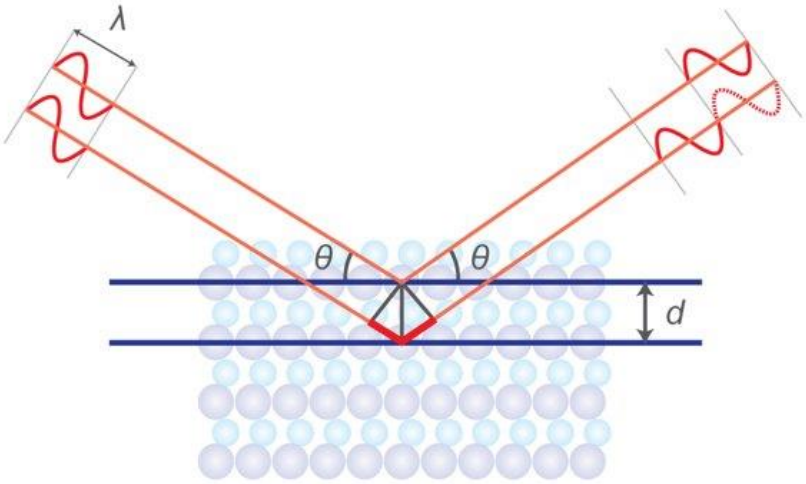

Figure 2.1 Illustration of Bragg diffraction. Image source: [61]

$$n\lambda = 2d(sin\theta) \qquad (2.1)$$

XRD patterns can be compared to literature to confirm the crystal phases that are present. The understanding of Bragg's Law and the fact that λ is constant necessitate that a peak location increase must be from a lattice spacing decrease. This fact was used in this work to determine effect on pore sizes of structured mesopores as synthesis conditions were altered. Another important use of XRD is calculation of grain size. This is done with Scherrer's equation, eqn 2.2, where t is the average grain size, K is an estimation for shape factor which is 0.9 in this work for round particles, β is the width of

a diffraction peak that is measured at half of the peak height. This is referred to as full-width-half-max (FWHM). Scherrer's equation shows that as the FWHM decreases, the grain size increases. This is also used for the general understanding that broad diffraction peaks are formed when the powder is not very crystalline.

$$t = \frac{K\lambda}{\beta cos\theta} \quad (2.2)$$

2.1.2 X-Ray Photoelectron Spectroscopy, XPS

Unlike the bulk technique of XRD, X-ray photoelectron spectroscopy is a surface analysis technique obtaining information from only the top few nanometers of the sample [62]. Samples under vacuum are irradiated by X-rays of constant energy, hv, and photoelectrons are emitted fro the surface. The kinetic energy, KE, of the photoelectrons is characteristic of the element it originated from. Peak intensity and position provide chemical state and quantitative information. The binding energy, BE, of a photoelectron is related to the measured photelectron KE by the relation BE=hv-KE [63]. Evaluation of XPS spectra involves not only peak location, but also areas. This information provides chemical state and volume fraction of a phase [64].

In this work, the XPS spectra were recorded on a Kratos Axis Ultra DLD instrument equipped with a monochromatic Al Kα X-ray source (hv=1486.7 eV)operated at 15 keV and 150W and a hemispherical analyzer. The X-rays were incident at 45^{o} with respect to the surface. The pass energy was a fixed 40 eV. Powder samples were pressed into a Mo sample holder. Pretreatments were performed in-situ and transferred to the XPS without exposure to the air.

2.1.3 ^{27}Aluminum Nuclear Magnetic Resonance, Al-NMR

Nuclear magnetic resonance (NMR) techniques are utilized for characterizing the chemical bonds of a specific element. In a static magnetic field, samples are excited with a radiofrequency pulse producing a macroscopic magnetization of the nuclei in the direction of the magnetic field. Through repeated pulsing and relaxation, phase coherence develops and the decay of magnetization is detected. After applying a Fourier transform, a spectrum is received of intensity vs a dimensionless value for chemical shift. These spectra can be analyzed by comparing them to several published tables of peek shifts.

In the characterization of aluminosilicates, aluminum is studied in a Bruker Avance III HD 500 Mhz system with 1.9 mm solid-state MAS probe. Rotors are spun at 10kHz and 10^{o} flip angles. The irradiation power applied is 63 kHz. At least 512 scans are acquired for each spectrum with a recycle time of 10 s. Octahedrally coordinated aluminum produces a peak at 0ppm whereas tetrahedrally coordinated aluminum produces a peak at 55ppm [65]. Any aluminum that is incorporated into the Al-MCM-41 framework will be tetrahedrally coordinated, but aluminum outside of the framework will be octahedrally coordinated [65].

2.1.4 Nitrogen adsorption

The adsorption of Nitrogen is used to estimate the surface area, pore volume, and pore diameter of the catalysts and is conducted in a Micromeritics ASAP 2020 surface area and porosimetry analyzer. A catalyst sample weighing approximately 0.02 g is loaded into a pre-weighed glass tube and degassed at 403 K for 3 hours under vacuum. After degassing, the tube and catalyst are weighed together to calculate the weight of the

degassed sample. The sample is then analyzed by the ASAP 2020 using Nitrogen gas at its saturation temperature of 77K. The adsorption/desorption of N2 is measured at pressures ranging from 0.0048<P/P0<0.9859. By adjusting the pressure and calculating the volume of nitrogen physisorbed at each pressure, the ASAP 2020 produces adsorption and desorption isotherms for the nitrogen. It then uses the Brunauer-Emmett-Teller (BET) equation [66] along with the cross sectional area of nitrogen, $0.162nm^2$, to calculate surface area of the sample. Pore volume and pore diameter calculations use the Barrett-Joyner-Halenda (BJH) formula [67] and the assumption that pores are cylindrical.

2.1.5 Transmission Electron Microscopy (TEM)

Transmission Electron Microscopy is a powerful imaging technique achieving magnifications up to 1 million times. Electrons are emitted from a lanthanum hexaboride filament. Interaction of these electrons with the sample leads to scattering, while lack of interaction leads to the transmission of other electrons. An image is obtained by focusing the transmitted electrons on a fluorescent screen and images are captured using a charge coupled device (CCD) camera [68]. Materials with lesser densities will scatter less of the electrons producing brighter images than those of higher densities.

In this work, TEM was utilized to image the pores of mesoporous materials. This work was done on a Hitachi H-8000 TEM operated at 200kV. It has resolution of approximately 1 nm.

2.1.6 Scanning Electron Microscopy / Energy Dispersive X-ray spectroscopy (SEM/EDS)

Like TEM, SEM uses a high energy beam of electrons. Though many detectors are available for SEM, the one used for imaging in this work is the secondary electrons detector. When the beam of electrons strikes the sample, secondary electrons are created

when the electrons experience inelastic scattering. The secondary electron detector can produce high resolution images of sample surfaces with resolution less than 1 nm. As the electron beam strikes the sample, the electrons can also experience elastic scattering and can create characteristic x-rays. These x-rays are used for elemental alanlysis in a technique known as Energy Dixpersive X-Ray spectroscopy (EDS). EDS is used in this work for chemical analysis of the sample surfaces (about 5 nm) [69].

Two SEMs were used for the work discussed here. They are the Tescan Vega-3 SBU and the Zeiss Ultraplus Thermal Field Emission Scanning Electron Microscope. Both are equipped with SEM. The Tescan was chosen for work with the mesoporous aluminosilicates due to its option of a low vacuum environmental mode. This mode reduced charging that is customary on insulating materials such as oxides. The Zeiss was chosen for the ReO_x/CeO_2 project because it is equipped with apparition correction. To reduce charging, samples were plated with gold when the Zeiss was used.

2.1.7 Inductively Coupled Plasma Optical Emission Spectroscopy (ICP-OES)

ICP-OES is used for bulk elemental analysis of the catalysts. The ICP-OES used is a Perkin-Elmer Optima 2000. The plasma used is generated by sparking argon that has been passed through a quartz tube that is energized by applying a radio frequency to a coil around the tube. To use the ICP-OES the element being tested must be in solution. To analyze a solution, the auto sampler uses a peristaltic pump to draw the sample into a nebulizer which converts it into an aerosol that is then sprayed at the plasma. In the plasma, the aerosol breaks apart. The individual elements are excited in the plasma. Each atom emits a light, characteristic of the element, as it returns to ground state from the excited state. The emission intensity for each element is compared to the standards

and concentration is calculated. This uses the fact that light absorption at low atomic concentrations is linearly related to the concentration. [70]

To achieve accurate results with this technique, careful preparation work is required. Calibration solutions are made by diluting the standards to the proper ppm. Samples in this work were prepared with acid digestion. Pt was digested in aqua regia and Re was digested in HCl. The samples were heated overnight to 115^{o}C in closed digestion tubes containing the sample and the acid. After cooling, the samples were diluted to the correct ppm and filtered. As this technique is concentration dependent, it is important in all steps to be cautious of mass loss. An alternate method for sample digestion is fusion [70] which is sometimes used for alumino-silicates. For fusion, samples are melted with sodium peroxide over a Bunsen burner. After samples are completely melted, they are diluted with nitric acid and heated overnight at 115^{o}C. This method has been shown to work with ZSM-5 [71], unfortunately, complete digestion was not achieved for the mesoporous aluminosilicates used in this work. Due to the incomplete digestion, ICP was not used for the Si or Al content. An alternative method of digestion would have been HF, but the exact Si:Al ratios were not necessary for the work.

During analysis, a 5ppm Y internal standard was used, and an Mn solution was used for optical alignment. Three point calibration curves were made at the time of analysis and repeated 3 times. A quality check was performed with the middle calibration solution with a limit of error of 10%.

2.1.8 Temperature Programmed Desorption (TPD)

Thermal analysis methods such as reduction and desorption are used for both qualitative and quantitative analysis of catalysts. Temperature Programmed Desorption (TPD) involves adsorbing a probe molecule such as ammonia onto the surface of the catalyst and then monitoring its desorption as the temperature is increased. Comparing the desorption temperature of the adsorbate from multiple samples allows a qualitative comparison of the strength of the acid sites because stronger acid sites require a higher temperature for desorption. The reasons for using NH_3 are that it is small enough to reach internal acid sites, it will not react with itself, and one molecule of NH_3 will adsorb per acid site. Using this stoichiometry, measurement of desorbed ammonia provides quantitation of acid sites.

To use the NH_3-TPD, 0.3g of catalyst is loaded into a 3/8" quartz tube in a tube reactor. First the catalyst is dried at 115^oC under Ar flow, 50mL/min. Then the sample is dosed with 50mL/min NH_3 at 115^oC for approximately 30 minutes. After stopping the NH_3, Ar flow continues to purge the system of any non-adsorbed NH_3. The reactor is then set to increase the temperature to 800^oC using a 10 degree/min ramp. As the temperature increases, a mass spec is used to record the partial pressure of the NH_3 and a thermocouple records the temperature of the catalyst bed. The mass spec observes mass 16 for NH_3 because water could produce some mass 17. After the temperature programmed desorption is complete, a calibration of partial pressures is performed so that partial pressures can then be quantified as moles of NH_3 because the system is maintained at a constant flow of 50mL/min. Upon integrating the graph of moles of NH_3 vs Temperature, the total number of moles of NH_3 adsorbed can be calculated. This is then

divided by the mass of the catalyst, 0.3g, to know the moles of ammonia adsorbed per gram of catalyst.

2.1.9 Temperature Programmed Reduction (TPR)

Temperature Programed Reduction is used qualitatively to determine the temperature necessary to reduce a catalyst. With proper calibration, it can be used to quantify active sites by measuring the quantity of the reductive gas that is consumed.

TPR was performed on Micromeritics AutoChem II 2920 with a thermal conductivity detector (TCD). Catalysts, 0.2g, were supported on quarts wool as they were loaded into the u-tube. Samples were dried for an hour at 120^{o}C under the flow of H_2. The temperature was ramped from 40^{o}C to 800^{o}C at 5^{o}/min.

2.1.10 Fourier Transform Infrared Spectroscopy (FTIR) and Raman Spectoscopy

Raman and FTIR can be used hand-in-hand to aide in the determination of structure. [55], [72] Though the resulting spectra are often similar, they are different techniques and have different selection rules. This means peaks from one technique might not be active in the other or the relative intensities could be different.

Infrared spectroscopy detects the wavenumbers of infrared radiation that interact with a sample due to its vibrational states. FTIR makes use of an interferometer, which utilizes a stationary mirror and a precisely moved mirror to make an interferogram. This interferogram undergoes a Fourier Transform which results in the final spectra. In Raman spectroscopy a laser strikes a sample and the inelastic scattering, or Raman scattering, is detected. Only about 1 in 10^7 scattered photons are scattered inelastically, so the detected intensity is far lower than that of the laser. Being inelastic, these scattered photons either gain or lose energy. This energy difference is equal to the energy of a

transition the struck molecule undergoes. Whereas FTIR bands depend on the change in dipole moment caused by the separation of the electric charge between atoms, Raman bands depend on the change in molecular polarizability caused by the deformation of the electronic charge of the molecule. Intensities of both are proportional to the square of the change in either dipole moment or polarizability.

Examples of the different relative intinsities can be seen with O-H bonds and aromatic rings. O-H bonds have a strong stretching mode in IR but not in Raman. This is because two atoms involved have a large difference in electronegativity, but the electronic density deformation is small. Similarly, aromatic ring stretching produces intense peaks in Raman but negligible in FTIR.

In this work, FTIR spectra were generated on a Bruker Vertex 70 using an RT-DLaTGS detector. The software to record the FTIR spectra was Opus Version 7.8. FTIR spectra were recorded with $4cm^{-1}$ resolution using the Blackman-Harris 3-term apodization function. Raman spectra were recorded with a Horiba XploRA Plus Raman microscope.

2.2 Reactors

Throughout the course of this work, four reactors were utilized. They include: atmospheric batch, impellor stirred pressurized batch, magnetically stirred pressurized batch, and plug flow. These reactors will be discussed here along with their pros, cons, and operating procedures.

2.2.1 Atmospheric batch reactors

When ambient pressure is either desired or acceptable for a batch reaction, then a flask can serve as the reactor. With proper setup, a flask can be used for reactions that

are heated, stirred, and refluxed. Though not done in this work, flasks can have their atmosphere exchanged with a flowing gas. A majority of the atmospheric refluxed batch reactions in this work utilized 50 mL round flasks

2.2.1.1 Heating methods for atmospheric batch reactors

Flasks can be held in an oil bath for consistant heating. An oil bath may be as simple as placing a dish of oil on a hot plate with a temperature controller. For a temperature controller, the thermocouple may be placed in the oil or in the solution being heated. Often, the thermocouple is in the oil to reduce possible contamination in the reaction and to not interfere with the stir bar. By lowering the flask into the oil, the reaction can be surrounded by its heat source. Oil baths do not need to be stirred to maintain even heat because the heated oil has Brownian motion. Though oil baths are known for consistent heating, they are notorious for their weaknesses. The oil is messy when the flask is removed from the oil. If any water drips into hot oil, it can cause splattering. If water is spilled in an oil bath, it will boil out violently when the oil is heated. Aside from the messes involved, oil baths are difficult to heat. They are often heated by a hot plate, but if an oil bath is large, it can be difficult for the hotplate to heat. This causes large ramp times and strain on the hotplate. Instead of heating a dish of oil on a hot plate, a sturdier solution is to use an Ace Glass Instatherm Oil Bath. It is essentially a dish wrapped in its own heating mantle.

Heating mantles are a cleaner alternative to oil baths. Thermocouples may be placed between the flask and the mantle. Though the lack of oil is a huge benefit, heating mantles also have their downside. Heating mantles are often short, so the heating is

predominantly from the bottom. This could cause heat fluctuations in the reactor. If there is any spill on the mantle, the heating element may have a short.

A sand box is another clean alternative to oil baths. Like with oil, the flask can be placed deep inside the sand to be surrounded by heat. The high heat capacity of sand allows it to maintain even heating across the box. As sand is less expensive than oil, this is an inexpensive way to evenly heat multiple items at once. In our lab, we had a 12" x 12" x 2" aluminum cake pan filled with sand and placed on a Torrey Pines five position stir plate. While it was working, it had all the benefits of an oil bath plus the convenience of being able to evenly heat 5 reactions at once. Unfortunately, the mass was too much for the hot plate. The hot plate burned out in less than two months. A better heating source for the sand box might be heat tape.

2.2.1.2 Stirring of atmospheric batch reactors

Though overhead stirrers, or impellors, are available, the atmospheric batch reactions performed in this work were magnetically stirred. Magnetic stirrers often function a couple inches above the stir plate. This allows for the contents of a flask to be stirred while the flask is in one of the above heating options. If the researcher chooses to stir an oil bath, the stir bars may be cascaded.

2.2.1.3 Refluxing for atmospheric batch reactors

When heating liquid reactions, there is often the concern of evaporation. To minimize this, condensers may be used. However, it is important to choose the correct condenser for the process as some will not condense fast enough yet others may cause flooding. There are 2 types of glass condensers available for use in our labs: Graham condensers and coil condensers. At first glance, these condensers look the same; both

have a spiral tube inside the outer tube. In a Graham condenser, the reaction vapors are inside the spiral and the spiral is surrounded with cooling water. In a coil condenser, the cooling water is inside the spiral and the spiral is surrounded with the reaction vapors.

Given the temperature of the cooling water and height of the condenser, a coil condenser may not provide enough cooling to condense all of the vapors. The Graham condenser has the risk of cooling the vapors faster than the condensate can return to the reactor. In this scenario, the vapors elevating from the reaction push the condensate out the top of the reactor flooding.

In this work, condensers arrangements were modified as needed. Reaction masses were often checked before and after reaction to monitor for vapor loss. For the 2-methylfuran reactions, a 6 inch coil condenser was attached to the reaction flask followed by 36 inches of Graham condenser. Having the coil condenser first reduced the risk of flooding. These condensers were cooled with 4^{o}C water from a circulating chiller.

2.2.2 Pressurized batch reactor

2.2.2.1 Introduction to three phase mixing

Batch reactors are frequently used today in both academia and industry. As reactors are varied through dimensions or condition changes, their heat and mass transfer performance must be validated. When using three phases, concentration gradients are generally a larger concern than temperature gradients [73]. Mass transfer hindrances in batch reactors have been blamed for discrepancies in experimental reaction rate calculations [74], and mixing methods have been frequently studied to reduce such mass transfer limitations inside batch reactors [75]–[77]. State of the art stirring devices are

now commercially available that generate a variety of flow patterns and have stir rates over 5000 RPM.

Stirrers are distinguished according to the flow they generate in the reactor and the choice of a stirring method depends on the needs of the desired reaction. To study a multi-phase reaction, such as the hydrogenation of a liquid using a heterogeneous catalyst, researchers must consider proper incorporation of all phases. To avoid mass transfer limitations, overhead impellers have been utilized in many recent multi-phase batch hydrogenation reactions[78]–[81]. Provided the ratio of liquid height to reactor diameter is less than 1.3, a single impeller is generally satisfactory for off bottom suspension of a solid into a liquid [77]. Incorporation of gas into the liquid is often attempted by use of baffles or gas entrainment impellors. Though baffles are known to increase the top-to-bottom flow, they also decrease the amount of total motion [76]. Also, the flow pattern in an unbaffled tank reactor stirred with a magnetic stir bar has been previously shown via modeling to have vertical flow with or without the formation of a vortex [82]. This begs the question, is the vertical flow from an unbaffled stirred tank sufficient for lab scale catalytic and kinetic studies? More specifically, would the simplistic method of using a magnetic stir bar in an unbaffled reactor be comparable to the commonly used complex stirring designs? Initially, the pressurized reaction in this work were performed in an impellor stirred, pressurized, batch reactor. As work progressed, a magnetically stirred, pressurized, batch reactor was designed, validated, and used.

2.2.2.2 Impellor stirred, pressurized, batch reactor

Pressurized catalyst screening reactions for the tetramerization of 2MF and for simultaneous tetramerization/Hydrogenation/hydrodeoxygenation reactions were done using an Autoclave Engineers bolted closure high pressure batch reactor made out of 316SS and corrosion resistant alloys. For the tetramerization studies, the 100mL reaction vessel was loaded with 1g of catalyst and 50mL of 2MF. The reactor was then bolted closed, purged with helium, and pressurize up to 500PSI with helium. The heating collar was placed around the vessel and heated to reaction temperature. For the hydrodeoxygenation (HDO) studies, the catalyst was loaded into the reactor without reactant. It was heated to 400^{o}C under H_2 flow to reduce the catalyst. After catalyst pretreatment, the reactor was cooled then the HPLC pumped 50mL of 2MF into the reaction vessel. The reactor was then heated to reaction temperature and pressurized to 500PSI with H_2. All reactions were stirred during the reaction at speeds up to 2000rpm

2.2.2.3 Magnetically stirred, pressurized, batch reactor

For use in hydrodeoxygenation studies, a pressurized batch reactor was designed that utilizes a magnetic stir bar without the need for baffles. However, before results could be trusted, it was imperative that we determine if the simplistic magnetic stir bar setup would be comparable to more complex methods of stirring. Using the hydrogenation of 2-Methyl-3-butyn-2-ol (MBY) with the Lindlar catalyst, experimentally obtained kinetic data is compared with published data obtained from a baffled batch reactor using a gas entrainment impellor [83]. It is demonstrated that on the lab scale, the magnetic stir bar design for stirring can be as effective as more complex gas entrainment systems. This simple approach to stirring demonstrated by the reactor

presented here allows for laboratory reactors to be more financially obtainable to academic research groups by proving that impellors are not always necessary for multi-phase pressurized reactions.

2.2.2.3.1 Design of magnetically stirred, pressurized, batch reactor

A 150mL reactor was machined on site from 316 SS. The reactor base has a 2" diameter cavity drilled out of a 3" diameter rod leaving a 0.5" wall and bottom. Six holes were tapped in the top of the vessel for a bolted closure, and a groove was made for proper placement of an O-ring. See Fig.2.2.

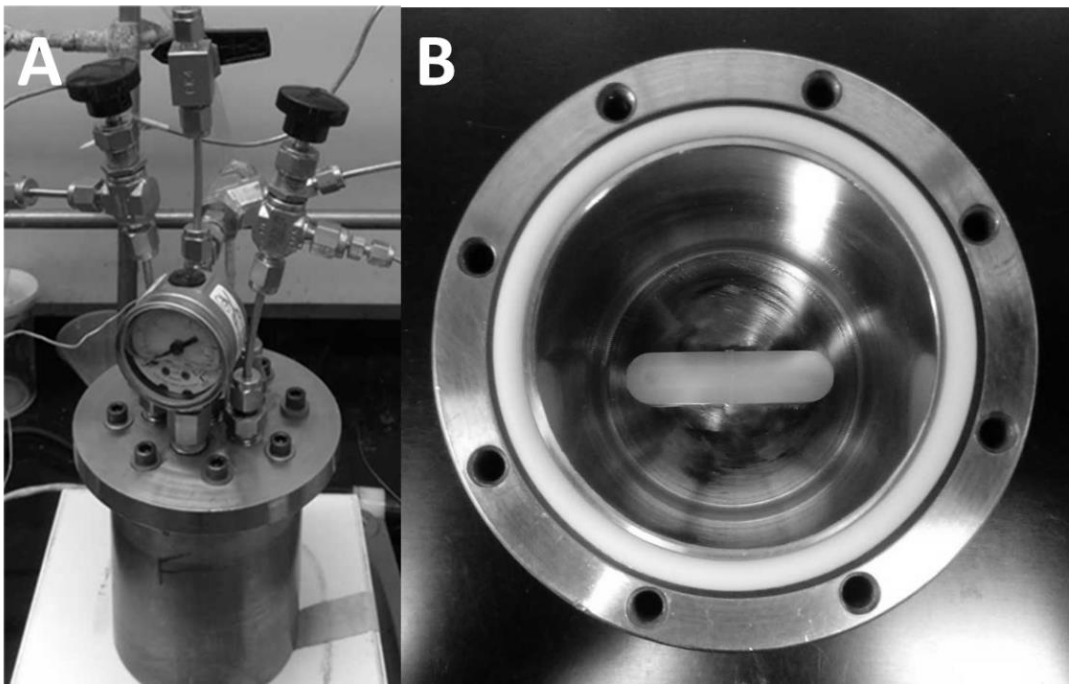

Figure 2.2 A) Picture of assembled reactor. The oil bath is not pictured. B) Reactor base showing 1.5mL cavity with 0.5" wall thickness, 1.5" stir bar, O-ring and holes for bolted closure

The lid assembly was designed to permit sampling of both liquid and gas phases during a reaction without the need to cool the reactor or depressurize it. The assembly was machined from a 0.5" thick 316 SS disk with 4" diameter. The disk was tapped for 0.25" NPT fittings. The pressure gauge was connected to one of the NPT taps using an

appropriate adapter. With the exception of the pressure gauge, connections were made using bore through adapters with 0.25” male NPT and 0.125” male tube fittings. Connections included a gas sampling/venting tube, liquid sampling tube, gas inlet tube, and thermocouple well. An additional connection was capped for the future use of liquid inlet. The lid assembly is sealed to the reactor base using a PTFE O-ring and 8 bolts.

For safety considerations, the reactor has been pressure tested to 100 bar and all connecting pieces are rated to higher pressures and temperatures over 423K. The gas sampling tube is equipped with a check valve to prevent air from entering the reactor after it has been purged. Attached to the gas inlet tube is a spring actuated pressure release valve. Heating is supplied with an oil bath. The temperature of the oil (TC) is controlled with a PID temperature controller. The internal reaction temperature (TI) is monitored with a k-type thermocouple that is inserted in the thermocouple well. A schematic is shown in Fig. 2.3.

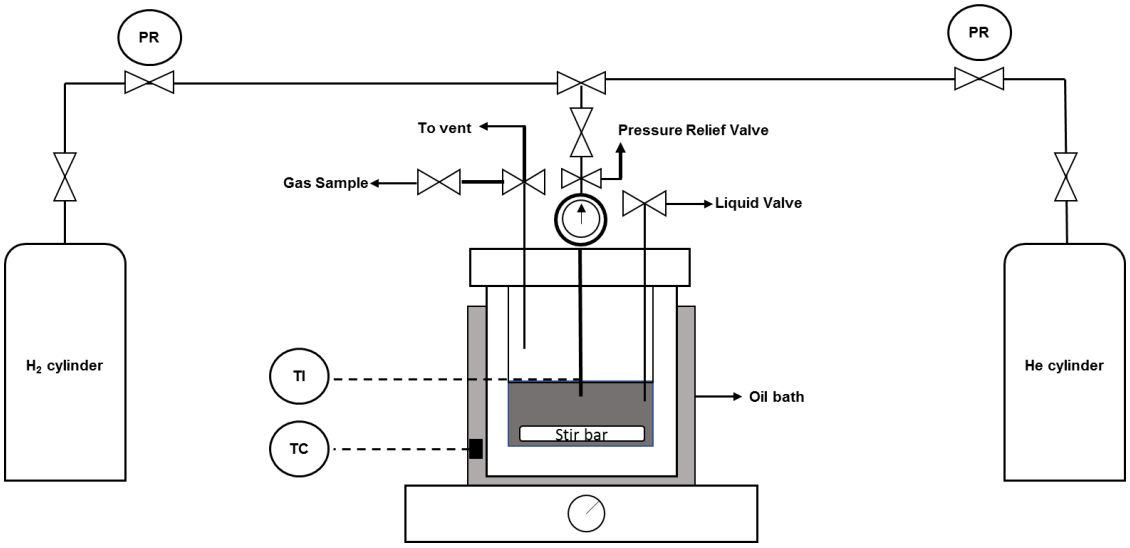

Figure 2.3 Schematic of magnetically stirred, pressurized, batch reactor setup

2.2.2.3.2. Materials and Procedure for validation of home-built batch reactor

2-Methyl-3-butyn-2-ol (MBY) (98%), 2-methyl-2-butanol (MBA) (99%), 2-methyl-2-buten-2-ol (MBE) (98%) and Lindlar Catalyst (5 wt % Pd/$CaCO_3$ modified with Pd) were purchased from Sigma-Aldrich and used as received. Methanol was purchased from Fisher Scientific. Ultra-high purity hydrogen (99.999%) and Helium (99.999%) were purchased from Praxair. A 1.5 inch Fisherbrand™ Octagon Spinbar™ was purchased from Fisher Scientific.

The reactor and oil bath were placed on a magnetic stir plate with digitally controlled variable stirring. The reactor base was loaded with a 1.5" magnetic stir bar, 50 mL of MBY and 0.076g of Lindlar catalyst. After sealing the reactor, helium was used to check for a leak tight seal and to purge the reactor of air. After venting the helium, stirring was initiated and the reactor was heated to 333K. After preheating the reactor, it was pressurized to 9 bar_g with hydrogen. Reaction time begins when the reactor is charged with hydrogen. To maintain reactor pressure, hydrogen was supplied through the entirety of the reaction.

At chosen sampling times, liquid samples are drawn. Approximately the first 0.25mL of sample is discarded and the following 0.5 mL of sample is saved for analysis. A Shimadzu GC-2010 Plus, discussed later in section 2.4.1, was used to analyze liquid samples using a Restek Rtx-1701 column and a flame ionization detector. The GC was calibrated for MBY, MBE and MBA using 7 point calibration curves. Liquid samples were allowed to cool to room temperature, filtered using 0.22um pore size PVDV filters, and diluted using methanol to $1/50^{th}$ the concentration. An AOC-5000 auto-injector was utilized to inject 1.0 uL of the diluted sample into the split injection port where it was

vaporized at 523K. Helium was used as a carrier gas with a total flow of 30.5 mL/min of which 2.5 mL/min was flown through the column. The GC oven was initially held at 313K for 3.0 minutes. It was then ramped to 328K at 10K/min and then to 343K at 1K/min.

2.2.2.3.3. Results and discussion of batch reactor validation

Validation of proper mixing was done by comparing measured kinetics of the hydrogenation of MBY with those known from literature. This reaction was chosen because it requires transfer through three phases and because it is what we considered a mid-speed reaction. It is fast enough that mass transfer limitations would be obvious while not too rapid that the kinetic values are still publically debated. Validation of the reactor with this reaction provides confidence in future reactor use with reactions of slower kinetics.

Reactions were run at 333K and 9.0 bar gauge. Maintaining the constant ratio of catalyst to liquid reactant of 0.175 wt%, stirring rates were adjusted to find the optimal stir speed for this reactor design. With a liquid sampling valve, the reactor discussed here allows for samples to be drawn without stopping the reaction. This allowed us to make reaction profiles of from a single reaction. The reaction profile resulting from a stir speed of 550 RPM is shown in fig.2.4A. MBY is almost completely consumed within 150 minutes. The MBY is hydrogenated to 2-methyl-3-buten-2-ol (MBE) which is hydrogenated to 2-methyl-2-butanol (MBA). This reaction profile is comparable to the profile in literature as shown in Fig. 2.4B [83].

To determine the optimal stir rate for this reaction in this reactor, the consumption of MBY was observed after 120 minutes of reaction for stir rates from 250 to 800 RPM.

At stir speeds below 550 RPM, the rate of reaction increased as reaction rates increased. With stir rates of 550 RPM and higher, the average reaction rate was constant for successful reactions. However, for stir rates of 700 and above, only about 30% of the reactions were successful. The other 70% of the reactions had extremely low conversions which is likely due to the stir bar spinning out of control. At 550-650 RPM, it is very rare that a reaction will not proceed, so this is the optimal stir rate range.

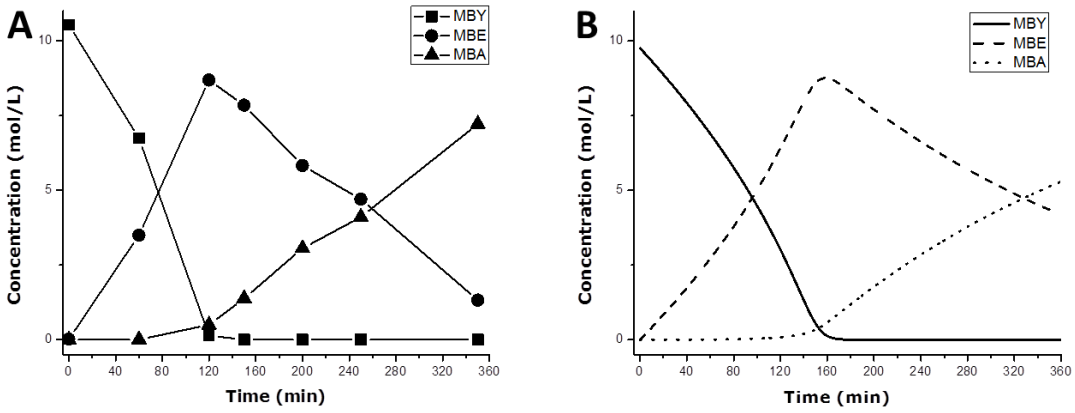

Figure 2.4 A: MBY hydrogenation reaction profile with stir rate of 550 RPM. B: Model results from literature[24] using P=9 bar gauge, T=333K, and catalyst to reactant ratio=0.175 wt%.

The 120 minute average reaction rates that were measured using the successful reactions with stir rates of 550-800 RPM had an average of $8.3*10^{-2}$ mol/L/min with a standard deviation of 0.003. This is faster than the previously published 120 minute reaction rate of $5.6*10^{-2}$ mol/L/min achieved with a baffled reactor using a gas entrainment propeller. This discrepancy can be explained with the two experimental differences. The concentration calculations presently reported are based on room temperature densities, whereas the previously published values were calculated based on the density at 333K. Adjusting our reaction rate using the ratio of 821/868, the current

reaction rate is lowered to $7.9*10^{-2}$ mol/L/min. The other difference is in stirring procedure. For the reactions reported above, the reaction slurry was stirred during heating. In literature, the stirring did not begin until the hydrogen was added. Our procedure allowed for the reaction to begin faster. To confirm this, two reactions were performed at a stir rate of 550 RPM in which the stir bar was not started until the reaction was fully preheated. For these, the density adjusted 120 min reaction rate was $5.8*10^{-2}$ ±0.002 mol/min. This value matches the previously published reaction rate, but this difference in rates based on stirring start times emphasizes the importance of beginning batch reactions with well mixed solutions. Stirring before adding the hydrogen does not begin the reaction, but waiting to stir could allow the catalyst to cake on the bottom of the reactor.

2.2.2.3.4. Conclusion of validation test

The design and validation of a 150mL pressurized batch reactor that uses a magnetic stir bar for agitation was discussed. It was demonstrated that the reactor could match the published reaction rate by not stirring until the hydrogen was added. A reaction rate that is 40% faster than reported in literature was reported by making the procedural change of stirring during preheating. By comparing reaction rates to those published, it was concretely shown that our homebuilt reactor was not limiting the hydrogenation of MBY. This study provides freedom to researchers to perform batch reactions without the need to utilize gas entrainment impellors. This greatly reduces expense and allows researchers to easily customize their attachments.

Due to the success of this validation study, this homebuilt reactor was used for the simultaneous hydrodeoxygenation studies of 1,4-anhydroerythritol and xylitol.

2.2.3 Fixed bed reactor

The flow reactions discussed in this theses were conducted in a fixed bed reactor. It is called such because the catalyst bed remains stationary in the reactor while the liquid and gas feeds flow through the bed.

2.2.3.1 Design of Fixed Bed Reactor

A schematic of the fixed bed reactor is shown in figure 2.5. The furnace used is an MTI-corporation GSL-1100x tube furnace with an 18 inch stainless steel reactor tube. The reactor has two feeds, one liquid and one gas, that join together just before entering the reactor tube. The gas feed uses mostly 0.25 inch stainless steel tube but decreases to 0.125 inch tube just before combining with the liquid feed. Flow rate is controlled by a Dakota mass flow controller capable of operating up to 1000PSI and controlling 0-500mL/min. There is a choice of two gasses tubed to the mass flow controller: helium for leak checking and post reaction flow and hydrogen for the pretreatment and reactions. The hydrogen line has a flashback arrestor between the regulator and the mass flow controller. After the mass flow controller, the gas line has a pressure gauge and a pressure release valve. The liquid feed begins with a 100mL glass graduated cylinder that holds the liquid reactant. It is pumped using an Alltech 426 HPLC pump, with a maximum working pressure of 6000PSI, through 3 feet of 0.0625inch tubing which is then enlarged to 0.125 inch tubing and passed through a quarter turn ball valve before connecting to the gas feed. As the combined feed enters the reactor tube, it passes through a fitting that connects the 0.125inch tube to the 0.5 inch tube. After the reactor, the product is immediately reduced back to 0.125 inch tubing that passes around a chilled heat exchanger. After the heat exchanger, two different configurations were used.

Initially, for the work with 2-methyl furan and butanal, the products entered a 500mL condenser. The gas stream from the condenser went to the back pressure regulator. This

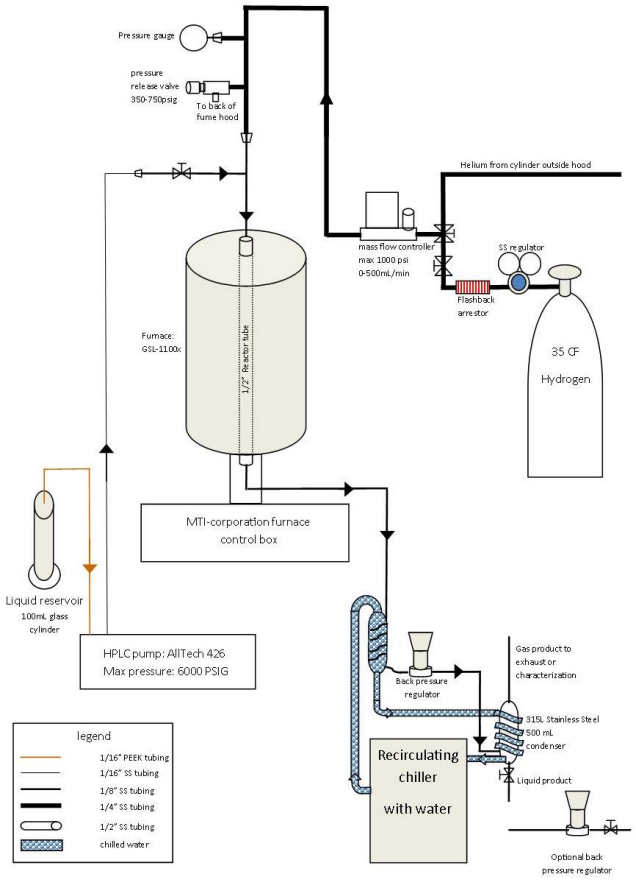

Figure 2.5 schematic of fixed bed reactor

had the benefit that all separation was done on the pressurized side of the system, so high vapor pressure chemicals such as 2-methyl furan could condense. Concern was raised that the 500mL condenser was unsafe because it contained most of the pressurized hydrogen in the system. It was mandated that the condenser be moved to the low pressure side of the back pressure regulator. This lowered the total pressurized volume to below 200mL. This change was made after the work with 2-methylfuran and butanal but before the work using 2-methylfuran as the sole reactant. Beyond decreasing the safety hazard of pressurized hydrogen, this also provided the functionality of drawing

condensed samples during the reaction. Unfortunately, the 2-methylfuran would not condense in this set up and flowed out with the hydrogen. Also, though the back pressure regulator was designed to regulate with liquid or gas, it did not maintain pressure well with liquid flowing through it. It often needed manual adjustment throughout the 20 hr reactions.

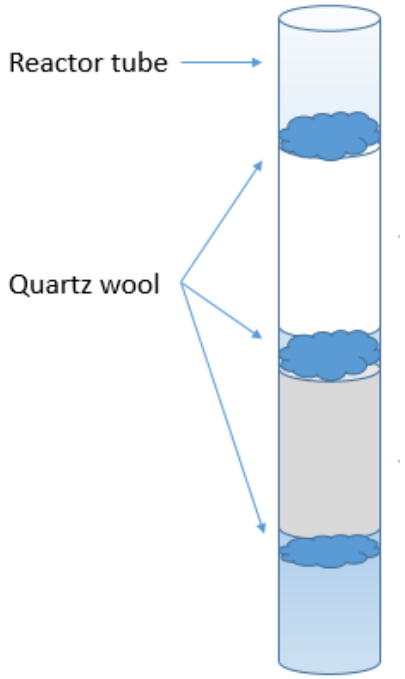

Figure 2.6 illustration of dual layer catalyst bed

The fixed bed reactor uses a 0.5" OD reactor tube. Quartz wool was used to keep the loaded catalyst in the tube. In the 2MF+BUT study, 5g of catalyst was loaded in the tube. Due to the low density of the catalyst, the tube was almost full when used. For work after the 2MF+BUT, a dual layer bed was desired. This allowed for two distinct catalysts to be utilized allowing one reactor to be used for two reaction steps. The first layer did not have a noble metal and was used for the alkylation step. The second step

had the bifunctional catalyst that could continue alkylation and also perform hydrodeoxygenation. This is illustrated in Fig. 2.6.

2.2.3.2 Operating procedure for fixed bed reactor

The glass cylinder was filled with 2-methylfuran (2MF) and the pump priming was checked by disconnecting the 0.0625 inch tube from the reactor and pumping 2MF through it. After checking the priming, the pump was turned off and the tube was connected to the other reactor tubing. The quarter-turn valve was closed to keep the liquid and gas separated until the reaction was set to begin. A total of 5g of catalyst powder, not pelletized, was loaded into the reactor tube supported by quartz wool. Once the tube was loaded, it was inserted into the tube reactor and the fittings tightened according to Swagelok instructions.

Leak tests were performed on the system before each use by flowing helium at 60mL/min up to 500psi. The electronic leak detector was used on each fitting, and fittings were tightened as necessary. To obtain the desired pressure, the back pressure regulator was adjusted until the system pressure reached 500PSI. After leak testing the system with He, hydrogen flow was begun and the tube furnace was set to 400^{o}C for 1 hour to reduce the catalysts. During this time, the system was checked again for leaks that may have developed during the heating process. After reducing the catalysts, the reactor was cooled to the reaction temperature, the HPLC pump was turned on to pump 0.02 mL/min and the valve between the liquid and gas tubing was opened.

Reactions length was 20 hours. When the reaction was complete, the furnace was turned off and He was allowed to flow through the system to purge the system of any remaining product.

2.3 Product analysis

2.3.1 Gas Chromatography, GC

The liquid reaction products are tested with gas chromatography (GC) using a Flame Ionization Detector (FID) to determine the chemical makeup of the product. The sample is prepared for the GC by diluting the product with a solvent and mixing it with sonication. A small amount of this is transferred to a vile compatible with the GC auto sampler. The GC auto sampler injects 1μL of the dissolved sample into the injection port of the GC where it is heated to 200^{o}C under helium flow. The helium, 100kPa at 1.33mL/min, then carries the volatiles to the column. The column is in an oven that is heated following a method chosen for product separation. The molecules of the sample are separated and elute from the column at various times based on vapor pressure and affinities for the stationary layer inside the column. As each chemical elutes, it is detected using an FID which combusts the carbons using a hydrogen flame. The computer then produces a spectrum of FID intensity vs. elution time. Integration of the non-solvent peeks is used to determine the percent of the carbons that are in each product. This does not report what the products are, just what elution time they had. Once all of the products of a reaction have been analyzed by other methods, then it can be assumed that for the same reaction the products at a given elution time will be the same products. For reactions with known products, the GC can be calibrated to give results in concentration instead of area percent.

A Shimadzu GC-2010 Plus with flame ionization detector was used to analyze liquid samples in this thesis. The 2-methyl furan project used dilution of 0.1mL of product in 25mL of acetone with a 30m, 0.25mm ID, Restek ZB-5MS column. The oven

held at 40°C for 3 minutes and then used a 10°C/min ramp to 280°C. For the other projects, a Restek Rtx-1701 column was used with products diluted to 300 times their volume with methanol. The GC was calibrated using 7 point calibration curves.

2.3.2 Gas Chromatograph – Mass spectroscopy, GC-MS

To determine what the batch reaction products are, we use a GC coupled with mass spectrometry. Here, the products are separated in the GC as described above and then products flow into the quadrupole mass spectrometer (MS) one at a time. The MS quadrupole uses an oscillating electric field to selectively choose which mass:charge ratios pass to the detector. This produces a spectrum showing fragment ratios of each molecule being analyzed. Based on the relative intensities of the fragments, information is gleaned about the structure of the molecule. Mass fragment spectra can also be compared to model libraries for quick identification of common products.

2.3.3 Nuclear Magnetic Resonance, NMR

As not all molecules are easily identified with a GC-MS, it is good to confirm new GC-MS results with H-NMR and sometimes C-NMR. If a product can be separated into individual molecules, NMR can be used to determine its structure. If a slurry is tested, NMR can be used to determine if it contains any molecules with certain functional groups such as furan rings. Samples were taken to the NMR center and analyzed by Dr. Pellechia using H-NMR and C-NMR. This was utilized for the identification of the 2-methylfuran tetramer. The H-NMR samples were dissolved in deuterated chloroform and run on a Bruker Avance III HD 300. The C-NMR samples were run on a Bruker Avance III D 500.

CHAPTER 3

SYNTHESIS OF CATALYSTS

A heterogeneous catalyst is one that is in a different phase then the reactants. All studies in the work have used liquid or gas reactants, and all catalysts used were solid. Though many solid catalysts were purchased ready for use, several were synthesized on site. On-site synthesis, can give control over chemical content and freshness of the catalysts used. The two main synthesis techniques used were precipitation and hydrothermal synthesis. Often the solids acids were then impregnated with an active metal through wet impregnation. This chapter provides details of the synthesis techniques that would be necessary to reproduce the work that is presented in later chapters.

3.1 Precipitation method

With precipitation, a solid is formed from a homogeneous solution [84]. This is a frequently applied method of preparation for several catalytically relevant materials such as oxides with high purity [84]. In this work specifically, the precipitation method involves dissolving two precursors in separate solutions of water in stoichiometrically correct amounts then combining them. Upon mixing, a chemical reaction occurs switching the cations and anions and a solid is formed.

3.1.1 Amorphous Zirconium phosphate, ZrP_2

Zirconium phosphate was synthesized following a procedure found in literature [85] that was reported to produce an amorphous, high surface area solid acid. 45.08 g of $ZrCl_2O_8 \cdot H_2O$ was dissolved in 140 mL of DI water. 32.02g of $NH_4H_2PO_4$ was dissolved in 280 ML of DI water. The precipitate was filtered and washed with DI water. It was then dried at 100°C overnight and calcined at 400°C for 4 hours. The first attempt at this synthesis was unsuccessful, creating crystalline ZrP_2O_7, see Fig 3.1. Later syntheses produced the amorphous zirconium phosphate. No difference was found in the synthesis technique, but an additional literature search revealed that calcining at 610°C and above would produce crystalline ZrP_2O_7 [86]. It is possible that a setting was incorrect in the oven for the first synthesis. This demonstrates the importance of characterizing every batch of catalyst with XRD.

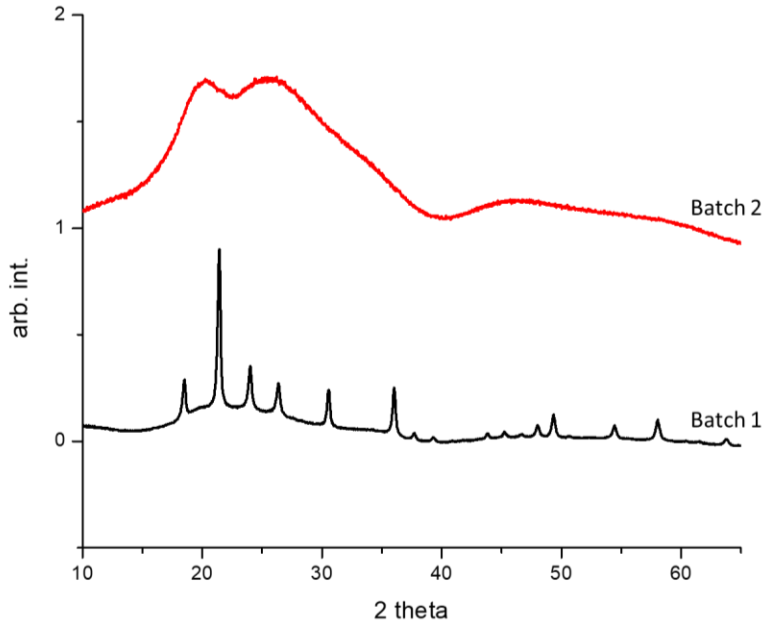

Figure 3.1 XRD of ZrP_2O_7. Batch 1 shows a crystalline structure. Batch 2 shows an amorphous structure

3.1.2 Mixed oxide of Mg/Al, MgAlO

MgAlO was synthesized with an Mg/Al ratio of 3/1 using a coprecipitation method similar to that found in literature [87], [88]. For solution 1, 34.89g of $Al(NO_3)_3 \cdot 9H_2O$ and 71.54g of $Mg(NO_3)_2 \cdot 6H_2O$ were dissolved in 187mL of DI water. For solution 2, 17.5g of NaOH and 11.9g of $NaCO_3$ were dissolved in 187mL of DI water. For solution 3, a pH buffer, 12g of NaOH was dissolved in 100mL of DI water. Solution 1 and solution 2 were poured simultaneously into solution 3. Samples were stirred for an hour and aged overnight. They were then washed, filtered, and dried at 120°C for 12 hrs. Finally, they were calcined at 600°C for 4 hrs.

These samples were initially characterized with XRD, but it was found that after a month's time the mixed oxide degraded to individual oxides. Recalcination returned the catalyst to its mixed oxide state, see Fig 3.2. Researchers must be aware that catalysts do not have infinite shelf life.

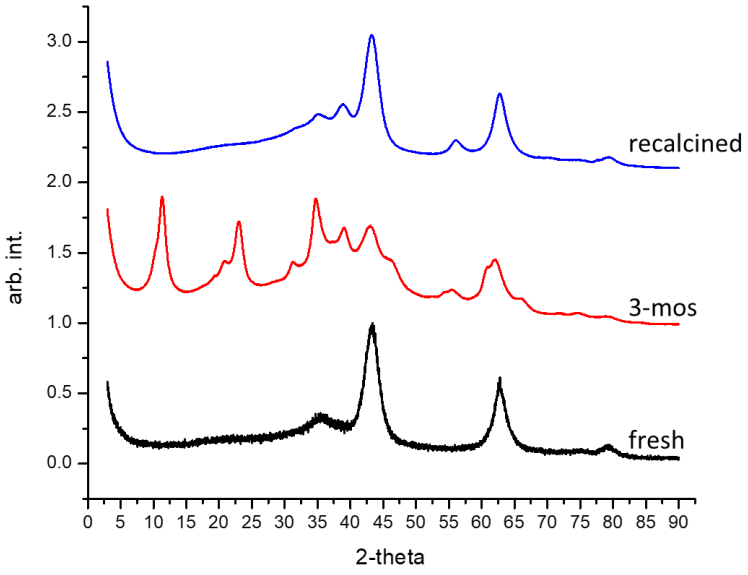

Figure 3.2 XRD of fresh MgAlO, the same catalyst 3 months later, and then after the catalyst was recalcined

3.1.3 Cerium Oxide, CeO_2

Cerium oxide was also synthesized using a precipitation method found in literature [89]. 2.88g of $(NH_4)_3CO_3$ was dissolved in 30mL of water. 6.51g of $Ce(NO_3)_3 \cdot 6H_2O$ was added to the ammonium carbonate solution. The solution was then sonicated for 2 hours before being filtered and washed with DI water for 3 times. It was dried overnight at 105°C and then calcined at 500°C for 6 hours. This synthesis technique produced a ceria that was very similar to the ceria we received from Daiichi in that the surface area of the synthesized CeO_2 was 88.74±0.25m^2/g and that of the commercial CeO_2 was 92.44±0.34 m^2/g. Though this synthesis was successful and could be used in the future, the Daiichi CeO_2 is used in this work. The purpose of using the commercial CeO_2 is two-fold. First, in is convenience to have CeO_2 always ready. Secondly, some reaction results are compared to those found in literature[44], [90]. Using the same source as in those literature studies helps to remove a variable in the catalyst synthesis. Commercially available CeO_2 varies widely in crystallinity and surface area available, and researchers must be careful of having too many variables.

In chapter 5, a calcination study is performed on ReO_x/CeO_2 using the CeO_2 purchased from Daiichi. It is found that higher calcination temperatures cause the CeO_2 to be more crystalline as evidenced by sharper XRD peaks. It is likely that the same would be true with the CeO_2 synthesized here.

3.2 Hydrothermal synthesis

This section speaks of the steps involved in synthesizing the mesoporous aluminosilicate that is used in chapter 4. The overarching technique is called hydrothermal synthesis even though that is just one of many steps. This technique has

many variables that can be tweaked during synthesis, and this section discusses the effects observed as just a few of those variables were adjusted.

3.2.1 Synthesis details and initial characterization

Initially, the goal was to produce Al-MCM-41, a mesoporous aluminosilicate with a well-ordered straw-like structure. The procedure presented by Kosslick [65] was followed using the same Si:Al ratio as the purchased Al-MCM-41, Si:Al=40. This procedure was chosen in part because it adds the aluminum to the synthesis before hydrothermal treatment. Reportedly [65], this allows the aluminum to be incorporated into the tetrahedrally coordinated framework.

The first step of synthesis required making a synthesis gel of molar composition $13.32Na_2O*xAl_2O_3*96SiO_2*30TEAOH*13.75HDTMACl$. This required weighing an Al pellet and calculating the correct amount of NaOH to have the Al:Na ratio correct for the size of the pellet. Generally, the Al pellets were 15-20 times the mass desired. The pellet and NaOH were heated to 80^{o}C in a beaker with 50mL of Di water. After the pellet was dissolved, the volume was returned to 50mL with the addition of more DI water. Then a portion of this solution was filtered by centrifugation and the appropriate volume needed for the chosen quantity of Al was measured. For instance, if the pellet was 18 times the mass of Al required, then the 50mL was divided by 18 and 2.78 mL was used. A 20% TEAOH solution was prepared by mixing the 35% solution with water. Then the aluminate solution was added to the TEAOH dropwise. This solution was added dropwise to the Ludox in a polystyrene container. When about half of the aluminate/TEAOH had been added to the Ludox, it would become too stiff to stir. A rigorous shake of the polystyrene container made the solution viscous enough for stirring

to continue. Lastly the HDTMACl was added and the solution was stirred for 30min. Though the volume of aluminate changed slightly based on the volume of the initial pellet, the TEAOH, Ludox, and HDTMACl volumes remained constant. 14.02mL of 35% TEAOH was mixed with 10.8mL of H_2O. 10.6mL of Ludox was used, and the HDTMACl solution was made by stirring 5g of HDTMACl into 15mL of DI water. After mixing, this produced roughly 50mL of synthesis gel

The synthesis gel was transferred to an 80mL Teflon lined, stainless steel autoclave which was heated to 115^{o}C for 3 days. The autoclave allowed the mixture to safely build pressure without all of the water evaporating. After 3 days of hydrothermal treatment, the autoclave was allowed to cool to room temperature. The product was washed with DI water and recovered with centrifugation until the pH was less than 8. This often required 10 washing cycles. This synthesized material was dried overnight and then heated to 600^{o}C with a 5^o/min ramp. It was calcined at 600^{o}C for 12hrs to remove the template.

After template removal, the Na+ ions were transformed to NH4+ form by heating it to 80^{o}C with an excess of 0.5M aqueous NH_4NO_3. This ion exchange was allowed to proceed overnight. It was then washed 3 times in a vacuum filter with DI water. After air drying the NH_4-Al-MCM-41 was calcined at 450^{o}C for 4 hrs to obtain H-Al-MCM-41.

To confirm the success of synthesis, the catalyst was characterized with XRD and Nitrogen adsorption and compared to the purchased Al-MCM-41. Before template removal, the synthesized catalyst has 4 XRD peaks, Fig. 3.3, corresponding to the hexagonal mesopore of MCM-41. The (100) peak of the synthesized catalyst is shifted

slightly to the left of the (100) peak of the purchased. This shows that, as synthesized, the mesopore is slightly smaller than the purchased one. However, upon calcination the structured mesopore becomes almost amorphous and the (100) peak shifts to the right. It no longer maintains the 4 peaks representative of Al-MCM-41. This is consistant with the characterization of the recipe reference [65]. This is customary of a disoriented unidirectional structure [91], [92]. In other words, it was thought to maintain the straw like structure with the straws no longer tightly packed. The nitrogen adsorption confirmed a high surface area of 1042±19 m^2/g compared to the surface area of the purchased Al-MCM-41 of 912±4 m^2/g. The BJH pore volume of the synthesized catalyst as calculated with desorption was only 0.58cm^3/g as compared to the 1.11cm^3/g of the purchased catalyst. This could be indicative of shorter tubes as is reasonable with the less ordered structure.

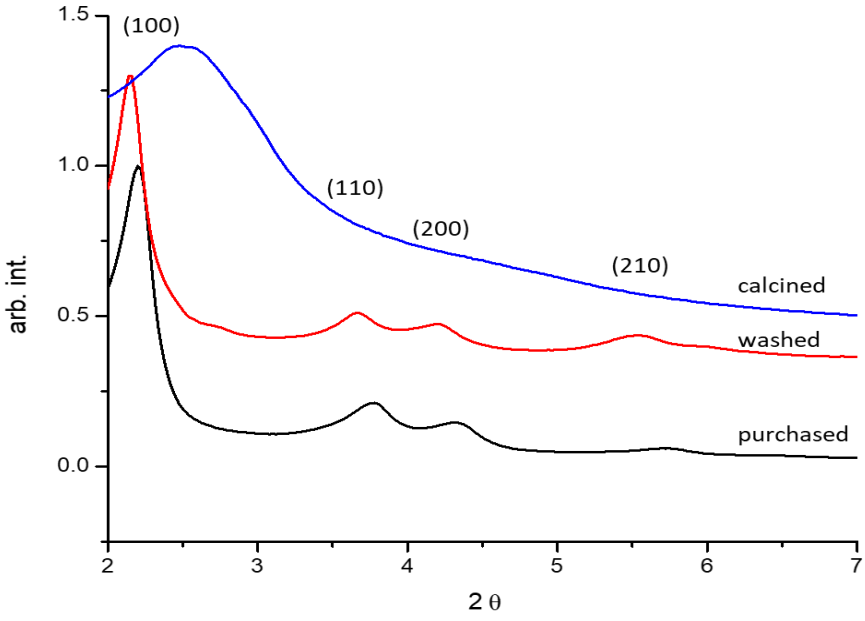

Figure 3.3 XRD of synthesized aluminosilicate vs purchased Al-MCM-41. The washed trace shows the XRD before calcination. The calcined trace shows that the aluminosilicate does not remain ordered after calcination

3.2.2 Adjusting Si /Al ratio of synthesized aluminosilicate

The first variable adjusted in the synthesis was the Si/Al ratio. Decreasing the Si:Al ratio not only adds acid sites, but it can also weaken the sites due to Next Nearest Neighbor interactions [93]. In the study by Kosslick [65], it was shown that acid density is maximized with Si:Al ratio of approximately 7. It is believed that increasing the aluminum content weakens the framework which in turn increases the number of Lewis acid sites. Weakening the framework also decreases the pore volume though the pore diameter will remain unaffected [94]. For this phase of synthesis, all conditions remained the same as stated above except for the amount of aluminum added to the synthesis gel. Though this slightly changed the water content, the overall volume remained similar so the hydrothermal treatment was as consistent as possible. Nitrogen desorption was used to analyze the samples with Si/Al=40, 20, and 12, and it was shown that most of the pore volume is contained in pores that are approximately 2.5 nm in diameter. This is consistent with expectation because of the templating agent used, HDTMACl.

TEM was performed on these same samples, Fig. 3.4. The consistency in the TEM and pore volume distribution with these varied Si/Al ratios shows that the structure is not degrading substantially with the added aluminum. However, it was discovered through TEM that the pores are not unidirectional as previously expected. These curved pores appear much more consistent with KIT-1. Without proving that these pores are branched like KIT-1, and knowing that they are not straight, the samples cannot be classified as Al-MCM-41 or KIT-1. Hence, they are referred to in this work as mesoporous alumino silicate.

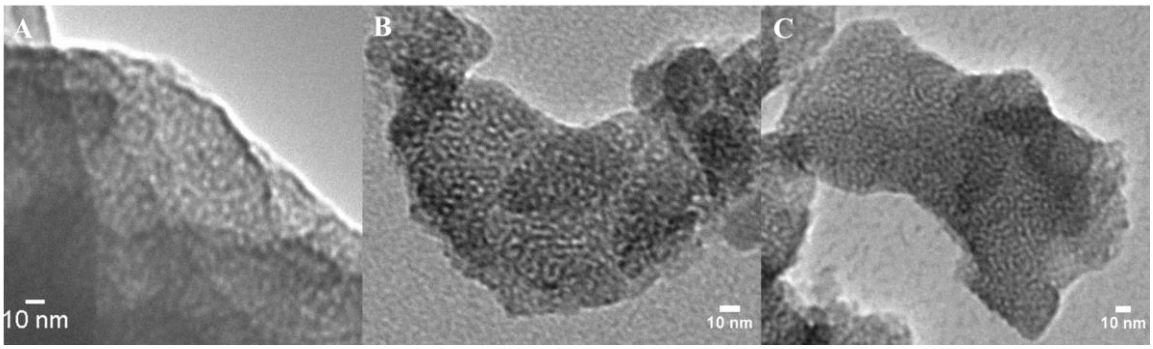

Figure 3.4 TEM images of aluminosilicate with various Si/Al ratios. A: Si/Al=40, B: Si/Al=20, C:Si/Al=12

Solid state NMR was used to analyze the purchased sample as well as samples of Si/Al= 40, 12, and 7. In the NMR results, 2 or 3 peaks are visible, see Fig. 3.5. The dominant peak in all of the spectra is the peak at 50-55 ppm. This is representative of tetrahedrally coordinated Al sites. This confirms that, though decreasing with increased aluminum, much of the Al sites remain incorporated in the framework. The peaks at 25-28 ppm represent 5-fold coordinated Al, and the peaks -0.2-1.2 ppm represent octahedrally coordinated aluminum.

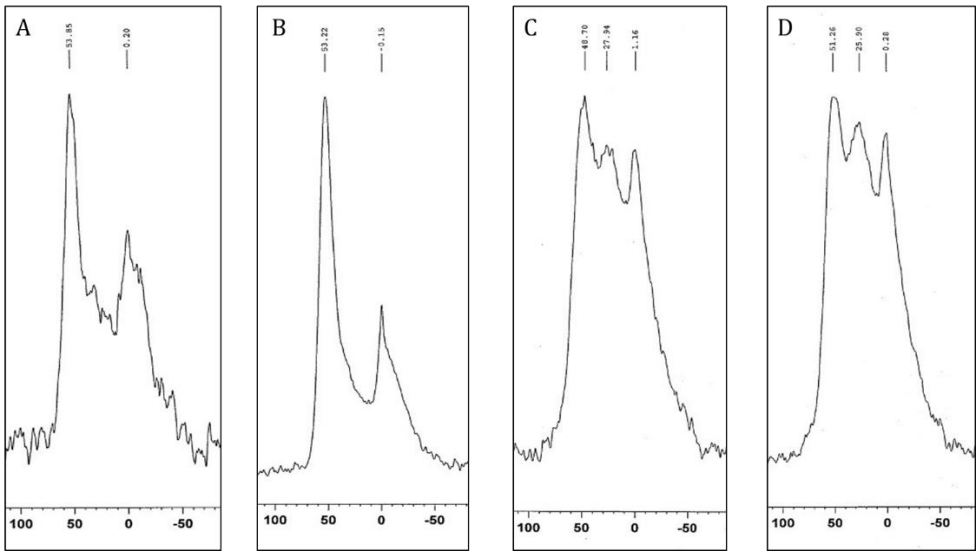

Figure 3.5 Solid state 27Al NMR of a) purchased Al-MCM-41, b-d) synthesized aluminosilicate with Si/Al=40, 12, 7.

3.2.3 Adjusting pore size of synthesized aluminosilicate

There was also interest in monitoring the effects of catalyst pore size on conversion and selectivity. Pore sizes can be modified slightly by changing the organic templating molecules. For the above syntheses, hexadecyltrimethylammonium chloride (hexadecyl-TMACl) was used as the surfactant. According to literature, this should have set the pore size to 3.4nm[95], but Nitrogen desorption showed the average pore size to actually be 3.07nm. Theoretically, surfactants with less carbons [95], such as dodecyltrimethylammonium chloride (dodecyl-TMACl), a 10 carbon surfactant, and octatrimethylammonium chloride (octa-TMACl), an 8 carbon surfactant, would lower the pore size as low as 2.5nm. By keeping all other conditions the same, the intent was to change pore size without greatly affecting other catalyst characteristics. This surfactant comparative study was performed with Si/Al=20.

Upon altering the surfactant, nitrogen desorption and XRD were used to calculate the pore diameter and unit cell diameter respectively. The difference of these gave the wall thickness. The values for surface area, pore diameter, unit cell diameter, and wall thickness are given in Table 3.1.

Table 3.1 analysis of aluminosilicate synthesized with various surfactants

surfactant	Surface area (m^2/g)	BET pore width (nm)	Unit cell diameter (nm)	Wall thickness (nm)
Hexadecyl(C16)TMACL	1000	3.07	4.47	1.40
Dodecyl(C12)TMACl	899	2.85	3.54	.69
Octa(C8)TMACl	431	5.02	X	X

Upon changing the surfactant, other adverse changes resulted to the structure of the aluminosilicate. Dodecyl-TMACl did lower the average pore width to 2.85nm;

however, the unit cell diameter also decreased more than the pore width so the calculated wall thickness was greatly decreased from 1.4nm for Hexadecyl-TMACl to only 0.69nm for Dodecyl-TMACl. The use of Octa-TMACl made the aluminosilicate structure collapse slightly as seen by the decreased surface area of only 431 m^2/g. Also, the C8 surfactant did not have the desired effect of decreased pore size as is seen by the facts that the calculated pore size increased. The XRD peak was used to calculate the unit cell width, but when using octa-TMACl the peak shifted below our detection limit of 2 2theta see Fig. 3.6, which is indicative of an increased unit cell size.

Figure 3.6 XRD of calcined aluminosilicate synthesized with various surfactants

One possibility for the failed synthesis using the Octa-TMACl was that the pH of the silica gel varied too greatly. pH is important for the proper formation of the mycelles. The amount of time that the synthesis gel is stirred can also effect the formation of the mycelles. To explore this, the pH and stir time were controlled before and after the addition of surfactant. A solution of NaOH was used to raise the pH while a HCl was used to lower it. In an effort to save time and gather as much information as possible without a huge delay, a ¼-factorial design was followed during synthesis using number of carbons in the surfactant, pH before addition of surfactant, stir time before addition of surfactant, pH after addition of surfactant, and stir time after the addition of the surfactant. The surface area was then measured after each synthesis. These conditions and resulting surface area are shown in Table 3.2.

As marked in red in Table 3.2, only two of these syntheses resulted in the desired high surface area. This is an example where the factorial design did not answer the question of the cause of the failed synthesis with the C8 surfactant. The only two synthesis that worked were the ones with the high pH before and after the addition of the surfactant; however, they were also ones that had the C16 surfactant. Given that a synthesis failed with the C16 surfactant that had the low pH, this does provide support to the hypothesis that low pH will cause a synthesis to fail. Because this design did not have a run with the C8 surfactant and high pH, it cannot be said for certain that pH was the only cause of the failure. At the time that this ¼-factorial was completed, these catalysts were no longer of interest. Therefore, further time was not devoted to making the synthesis work with the C8 surfactant.

Table 3.2 Single run, 1/4-factorial design, Si/Al=20

Surfactant	pH before	Stir before (mins)	pH after	Stir after (mins)	Surface area (m^2/g)
16	8	60	8	60	169
8	14	10	8	60	198
16	14	60	14	60	**1064**
8	8	10	14	60	2
8	8	60	14	0	200
16	14	10	14	0	**1020**
8	14	60	8	0	175
16	8	10	8	0	179
12	11	35	11	30	173

3.3 Wet impregnation:

3.3.1 specifics of Pt/MCM-41

The 0.1 wt.% Pt/MCM-41 catalyst used in this work was prepared by wet impregnation of Al-MCM-41 with a methanol solution of ammonium tetrachloroplatinate [96]. The Al-MCM-41 was mixed with the platinum solution under constant magnetic stirring at room temperature and the methanol was naturally evaporated overnight. The mixture was then dried in an oven at 100^{o}C for 10 h, and calcined at 550^{o}C for 3h with temperature ramping from room temperature to 550^{o}C at the rate of 5^{o}C min^{-1}. To insure that adding the active metal did not damage the pore system of Al-MCM-41, TEM and XRD were used to analyze the catalyst, Fig 3.7. The TEM image shows that the straight pores of Al-MCM-41 are maintained after the addition of the Pt, and the XRD shows that bulk order is also maintained.

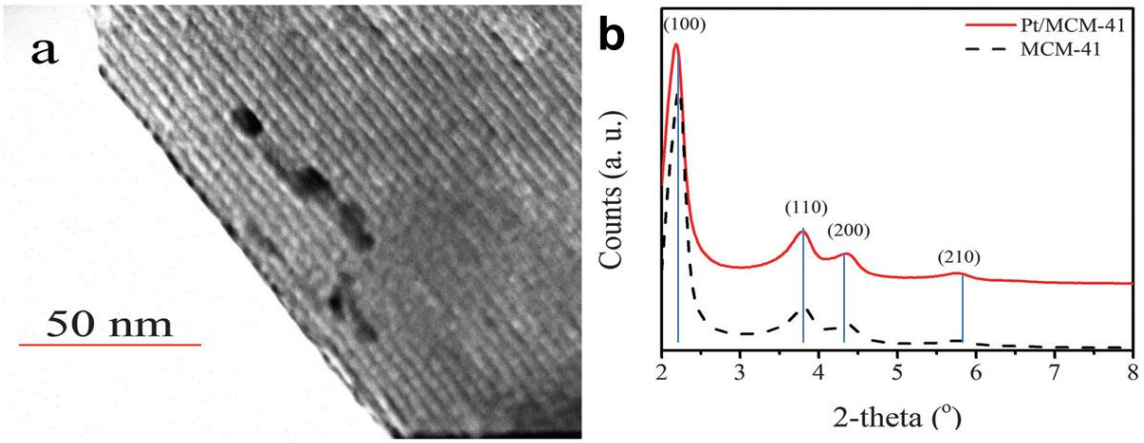

Figure 3.7 a:TEM, b: XRD of fresh Al-MCM-41 and the 0.1wt% Pt doped Al-MCM-41. Images adapted from [43]

In the TEM image of Fig. 3.7a, the Pt nanoparticles appear darker due to the higher electron density of Pt than that of silica and alumina in the wall of Al-MCM-41, which

are the gray stripes. Though depth cannot be seen in TEM, the Pt nanoparticles appear to be grown within the boundary of the Al-MCM-41 pores. This is seen because the growth direction of Pt nanoparticles aligns with the pore channels of Al-MCM-41. Thus, based on the TEM images, the Pt nanoparticles are believed to be located inside the pores of the Al-MCM-41 instead of on the outer surface of the Al-MCM-41.

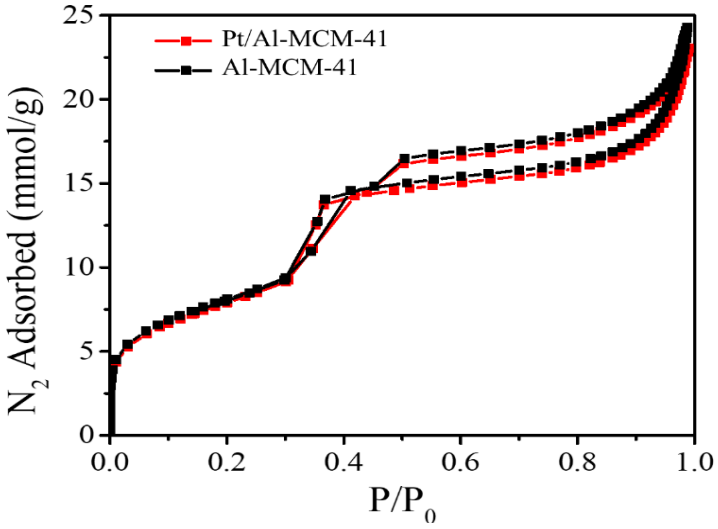

Figure 3.8 Nitrogen adsorption and desorption isotherms of fresh Al-MCM-41 (black) and Pt/Al-MCM-41 (red) Image adapted from [43]

Nitrogen adsorption and desorption experiments, in Fig 3.8, indicate that the pores remain largely open and accessible. The Pt/Al-MCM-41 shows nearly identical isotherm curve to that of pure Al-MCM-41. Both the isotherm curves of Pt/Al-MCM-41 and Al-MCM-41 are typical type IV curves, which indicate that the two samples have a similar mesopore structure. Furthermore, the average pore size of the Pt/Al-MCM-41 was calculated to be 3.1 ± 0.3 nm, which is consistent with the TEM images and, within the experimental error, is the same than that of fresh Al-MCM-41 (2.6 ± 0.3 nm). After the deposition of Pt, the surface area of the catalyst was determined to be 612 ± 10 m^2 g^{-1},

which is slightly lower than the value of 650 ± 5 $m^2 g^{-1}$ measured for pure MCM-41. The pore volume decreases from 0.795 to 0.767 $cm^3 g^{-1}$. In both cases, less than a 6% reduction is observed after the deposition of Pt.

3.3.2 Specifics of ReO_x/CeO_2 and ReO_x-Pd/CeO_2

The CeO_2 supported catalysts used in this work were made using CeO_2 that was donated by Daiichi Kigenso Kagaku Kogyo Co., Ltd. Impregnation procedure was similar to that found in literature [44], [90]. For ReO_x/CeO_2, the desired amount of ammonium perrhenate (NH_4ReO_4) was dissolved in DI water and then CeO_2 was added. The quantity of water was not measured with precision, but it was always initially enough to allow the mixture to stir freely. The solution was heated to 80°C while stirring overnight to allow the water to evaporate. It was then heated at 110°C for 3 hours to ensure complete dryness. Finally, it was calcined at 500°C for 3hrs. For ReO_x-Pd/CeO_2, a second impregnation step was utilized. After drying the ReO_x/CeO_2 but before calcining it, the ReO_x/CeO_2 was added to an aqueous solution of $Pd(NO_3)_2$. This was then dried again as above and then calcined at 500°C for 3hrs. Characterizations of these catalysts are specific to loading and are provided in chapter 5 where they are discussed.

CHAPTER 4

LONG CHAIN CARBOHYDRATES AND HYDROCARBONS FROM PLATFORM CHEMICALS

Here-in is first discussed our initial work[43] of producing long chain hydrocarbons from waste derived chemicals, summarized below in section 4.2. It is shown that 2-methylfuran (2MF) and butanal can be utilized to produce C8+, 72% nonane, in a single, solvent free, fixed bed reactor. Producing C8+ in a single continuous step showed that chain growth and HDO can be performed in a scalable fashion. Being a continuous, solvent free reaction, this is a successful proof of concept of a single step alkylation/HDO.

The C8+ alkanes, discussed in section 4.2, are not as long as desired because they are not long enough to be considered a crude substitute[30]. They are of suitable length to be added to the light crude oil processing at a refinery. Section 4.3 address the concern of the carbon length of the final HDO by focusing on the production of suitable carbohydrates. This section discusses a screening to choose a potential bifunctional catalyst and reactants.

Section IV focuses on a catalytic study for the oligomerization of 2MF. Included are a catalyst screening followed by optimization of an aluminosilicate for the production of the 2MF trimer and tetramer. Initial results from a high pressure batch reaction show the feasibility of using 2MF for single step production of a crude replacement.

Though section 4.2 utilizes a fixed bed reactor for the simultaneous alkylation and HDO of reactants, sections 4.3 and 4.4 rely on batch reactors for the screening of chemicals and catalysts that could be used in the fixed bed reactor in the future. Sections 4.3 and 4.4 are focused purely on the formation of carbohydrates that have been shown in literature to produce crude substitutes upon HDO[33], [34], [97], [98].

4.1 C8+ production from 2 methyl-furan and butanal in a single step reactor

In this section, the concept of producing long-chain hydrocarbons in a single step reactive process by utilizing a bi-functional catalyst with both acid and metallic sites is demonstrated. This is done through the production of a C8+ hydrocarbon mix using 2MF and butanal as reactants. Our approach utilizes a solid acid for the alkylation function and a transition metal as hydrodeoxygenation catalyst. A series of solid acids was screened, among which Al-MCM-41 demonstrated the best combination of activity and stability. Platinum nanoparticles were then incorporated into the Al-MCM-41. The Pt/MCM-41 catalyst showed 96% yield for C8+ hydrocarbons and the catalytic performance was stable over four reaction cycles of 20 hours each. This section is an overview of the work spearheaded by Cun Wen published here [43]. This section is necessary to understand the relevance of the work that follows in sections 4.3 and 4.4.

4.1.1 Alkylation activity tests

For the first set of catalyst screening, a refluxed batch reactor with magnetic stirring was used to screen for materials that would make effective alkylation catalysts. The first set of reactions involved a broad sampling of potential solid-acid catalysts including: ZSM-5, meso-ZSM-5, Al-MCM-41, sulfated zirconia, and amberlyst-15. In the first screen, a 15 mL mixture liquid of 2MF and butanal (mole ratio of 2MF: butanal

is 2:1) was added to 0.22 g of catalyst. The reactions were performed at 80°C for 20hrs to set a baseline for alkylation activity. After the reaction, the liquid product was filtered using a syringe filter and analyzed with a gas chromatography-mass spectrometry (GC-MS). The conversion of 2MF is shown in Fig. 4.1. As expected from literature, these reactions had high selectivity toward 1,1-bisylvylbutane [37].

ZSM-5 zeolite was included in the screening based on its well-known acid catalysis properties [99], [100] including alkylation [101]. However, ZSM-5 shows poor activity for the alkylation between 2MF and butanal, with only 1±1% of 2MF converted after 20 hrs of reaction. The molecular size of 2MF is estimated to be between 4.8-7.3 Å, based on literature reports [102], [103]. It is possible that the low activity of ZMS-5 may be attributed to the small pores, in the range of 5.4-5.6 Å [104], not allowing product formation. An attempt was made to increase the accessible surface area by synthesizing mesoporous ZSM-5 following literature reports [105]. This resulted in only a slight increase in the catalytic activity for 2MF and butanal alkylation from 1% to 4% [43].

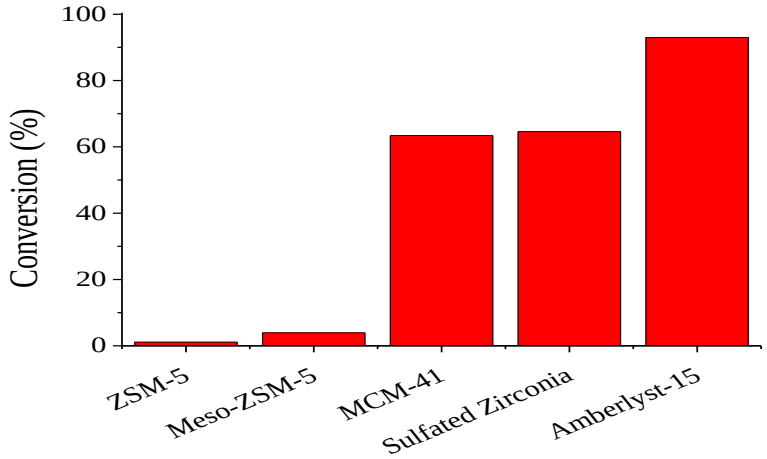

Figure 4.1 Conversion of 2-Methyfuran on different solid acids catalyst in the alkylation reactions between 2-Methyfuran and butanal. Figure from [43]

Exploring the need for more accessible pore sites, 3 more catalysts were chosen for screening. Al-MCM-41 was chosen for its pore diameter of 2.6 ± 0.3 nm. Sulfated zirconia was used as a catalyst sample that did not have a structured pore system, so all acid sites are on the surface. Finally, Amberlist-15 was used in the screening process to have a baseline for comparison because it performed well for this alkylation reaction in literature [97]. These 3 catalysts all showed substantially higher activity than ZSM-5, see Fig. 4.1. Amberlyst-15 demonstrated the highest conversion of the catalysts screened with over 90% 2MF conversion. It was not chosen for the next step because it is a styrene-based resin that is not stable at temperatures above 140^{o}C [106], which is too low for the temperature range typically required for HDO (170-400^{o}C) [107], [108]. Sulfated zirconia and Al-MCM-41 had comparable reaction results of just over 60% 2MF conversion. Though sulfated zirconia performed well in the screening, it was not chosen for the use in the HDO reactor because of the possibility that its sulfate group may deactivate HDO-active metals, such as Pt [109], and may lead to sulfur contamination of the final biodiesel product. Al-MCM-41, having excellent thermal stability [110], [111] and nothing known to poison active metals, was considered the best choice when compared to sulfated zirconia and Amberlyst-15. Al-MCM-41 has much larger pores than ZSM-5 (2.6 ±0.3 nm vs 5.5Å) and high surface area (650 ± 5 m^2 g^{-1}). Therefore, from the initial catalyst screening, Al-MCM-41 was chosen as the acid catalyst and the support of the HDO functionality for the bi-functional catalysts.

4.1.2 bifunctional catalyst

After choosing Al-MCM-41 as a suitable acid for the alkylation of 2MF and butanal, an active metal needed to be added to it for HDO. Pt was chosen as it has been

used for many HDO processes [48], [112]. As described in section 3.3.1, Pt was loaded on Al-MCM-41 via wet impregnation of ammonium tetrachloroplatinate.

To be an active catalyst for HDO, the Pt should be in the metallic form [96], [99]. The oxidation state of the Pt after reduction under H_2 at 400°C was characterized with X-ray photoelectron spectroscopy (XPS). As seen from the Pt 4*f* XPS profile, Fig 4.2, the binding energy of Pt 4f 5/2 (70.6) is consistent with that of metallic Pt [113]. Thus, reduction at 400°C is satisfactory to in ensure that the metallic phase is present for the HDO reaction.

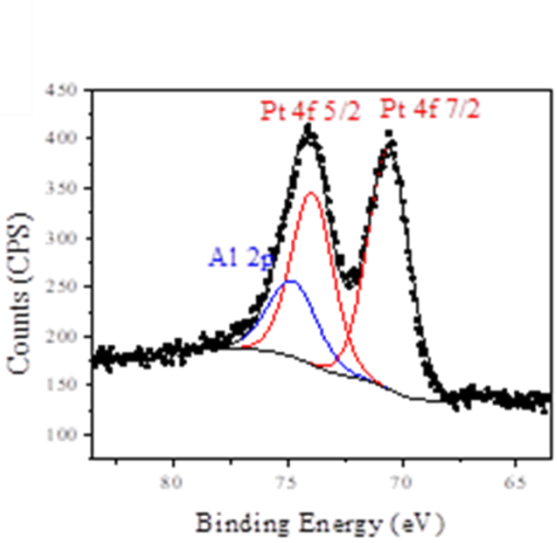

Figure 4.2 XPS of Pt/Al-MCM-41 image from [43]

4.1.3 Plug flow reactor results

After the formulation of the bi-functional Pt/Al-MCM-41 catalyst, the catalytic performance for biodiesel production was tested in a fixed-bed, plug flow reactor described in detail in 2.3.3. The initial intent was that the bifunctional catalyst would make the 14 carbon carbohydrate as produced in section 4.2.2 and then hydrodeoxygenate it to a 14 carbon hydrocarbon. However, it was found instead that the

predominant product was straight chain nonane. A significant amount of C8 hydrocarbons were also produced, so the selectivity results of a temperature sweep are reported for hydrocarbons with a carbon backbone of 8 or more carbons, see Table 4.1. At 503 K, the yield to C_{8+} is 96%, slightly higher than the yield obtained with the two-step process reported in the literature [37]. As the highest C8+ yield was obtained at 230°C, the product distribution is shown for that temperature, Fig 4.3A. With the high selectivity to C9, it is hypothesized that the hydrodeoxygenation is occurring too quickly for the complete formation of the C14 carbohydrate and the C9 is being produced from the hydrodeoxygenation of the alkylation product of 1 molecule of 2MF with 1 molecule of butanal as depicted in Fig. 4.3B. The biodiesel production on the bi-functional catalyst is proposed to follow the following reaction pathway: 2MF and butanal first go through an alkylation reaction to form 1-sylvyl-butanol, followed by hydrodeoxygenation reaction to form the final C_9H_{20}, as illustrated in Fig 4.3B. Further discussion of the reaction pathway may be found here[43].

Table 4.1. Temperature sweep with bi-functional catalyst for C8+ hydrocarbons.

Catalysts	**Temperature**	**Conversion[a]**	**C_{8+}Selectivity[b]**	**C_{8+} Yield**
0.1wt% Pt/MCM-41	350°C	100%	69%	69%
	280°C	100%	76%	76%
	230°C	98%	98%	96%

[a] The conversion is calculated by dividing the mole of converted 2MF to the original mole of 2MF measured by GC-MS. [b] The selectivity to C_{8+} are calculated by how many portion of carbon from the 2MF and butanal are converted to C_{8+} hydrocarbons, and are measured by GC-MS. The error for the calculated selectivity is ±7%.

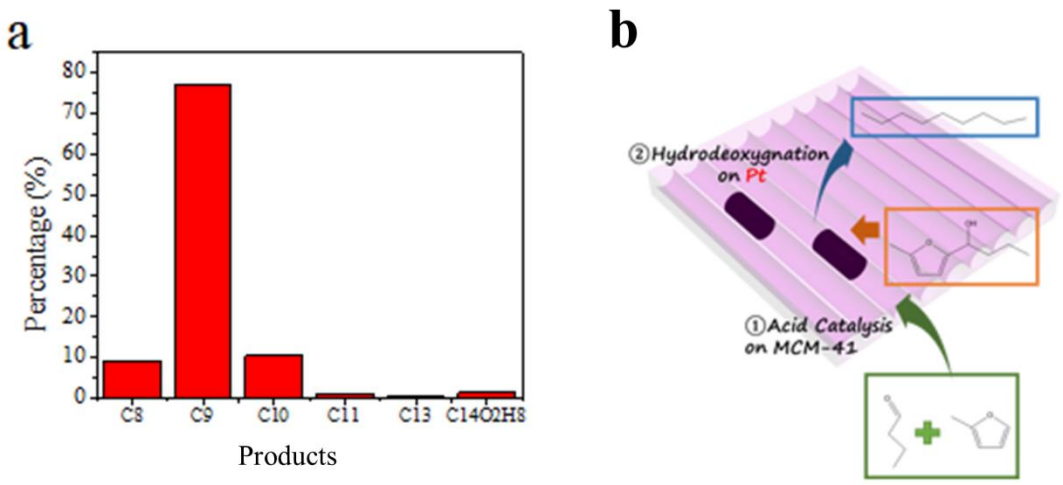

Figure 4.3. a) product distribution at 230°C over Pt/Al-MCM-41 (the percentage is calculated based on the percentage of total carbon in each production) and b) illustration of proposed reaction pathway resulting in nonane. Images from [43]

4.1.4 Catalyst stability

To make the bi-functional catalyst viable for large scale industrial use, the catalyst should not only have high yield, but also be stable under severe reaction conditions. Because high reaction temperatures may destroy the pore system of Al-MCM-41 by either dealumination or coking [114]–[116], the stability of the Pt/Al-MCM-41 catalyst is tested at 350°C, the highest temperature in this study, by reusing the same catalyst four times without regeneration. The conversion of 2MF and the selectivity to C_{8+} are retained at 100% and 69 ± 6%, respectively, which indicates excellent thermal stability of Pt/Al-MCM-41. Nitrogen adsorption and desorption was used on the spent catalyst, and it was observed that the type IV isotherm remained but the surface area of the spent catalyst is reduced to 43 % of the original surface area. Thus, the stability tests and nitrogen isotherm curves indicate that Pt/Al-MCM-41 has a good stability for this single step reaction.

4.1.5 Conclusion of C8+ production in a single step reaction

A bi-functional Pt/Al-MCM-41 catalyst has been developed to produce a light crude oil replacement from waste-biomass derived 2MF and butanal with yield of 96%. In the Pt/Al-MCM-41, the Al-MCM-41 works as both support for Pt and acid site for alkylation between 2-methylfuran and butanal to first form C9 carbohydrates, which is then hydrodeoxygenated to C8+ hydrocarbons on the Pt. The production of biodiesel on the Pt/Al-MCM-41 is sensitive to the reaction temperature, which influences the selectivity to hydrocarbon fuels and chain length of side-products.

4.2 Consideration of platform chemical processing steps

To further improve on the above process, consideration was given to the source of both reactants. Assuming reaction conditions and yield would remain similar, the overall efficiency of fuel production would be more efficient if less processing was required to obtain the platform chemicals used for the fuel production. 2 methylfuran is obtained from the reduction of furfural. This processing step could be eliminated if furfural were used in the single step production of alkanes instead of 2MF. Butanal was the co-reactant used above. Though butanal is plentiful and inexpensive, it requires several processing steps to obtain it from biomass. Levulinic acid is currently produced from hydrolysis of 5-hydroxymethylfurfural which is obtained via the dehydration of fructose or glucose. Though these sugars could be used in other well accepted routes to produce fuel, levulinic acid was considered here as a viable platform chemical because it can be formed in a single step from the sugar.

To understand the current knowledge of the conversion of furfural and 2-methylfuran into diesel, a brief review of literature was performed to see the various

reaction pathways that have been studied to obtain alkanes. The initial intent was to find a multi-step processes that could be adapted to the single step reactor. This would require that the carbon chain growth be performed on a heterogenous catalyst that was stable in the high temperature required for hydrodeoxygenation.

Furfural has been reacted with acetone using both Aldol condensation and Michael condensation [21], [35]. These predominantly produce carbohydrates that have either 13 or 8 carbons respectively; however, conditions can be adapted to produce C7-C31 [21]. This reaction is commonly performed in batch reactions containing two liquid phases with NaOH as the catalyst and THF as the organic phase solvent. No reports were found of these condensation reactions using solid base catalysts. This is due to the fact that these C13+ products have only minor branching and are therefore solid at room temperature [40], making it difficult to retrieve a heterogeneous catalyst.

Continuing the theme of addition of furfural and a ketone, furfural has been reported to react with both 3-pentanone and 5-nonanone over solid bases [40]. In these reactions, each ketone reacts with just one furfural molecule producing C10 or C14 carbohydrates with enough branching that the products remain liquid at room temperature. Furfural and methyl isobutyl ketone can be reacted stoichiometrically over CaO in a batch reactor at 130^{o}C for 8hrs for a 95% yield of a C13 carbohydrate.

2-methylfuran has also been reported with many co-reactants [97]. Condensation has been demonstrated with 2-methylfuran and a number of aldehydes and ketones over either homogeneous or heterogeneous acids. Additionally, 2-methylfuran has been reported to trimerize in acidic reactions in the presence of water or tetramerize without the presence of water [98]. These reactions would form a C15 or C20 carbon backbone.

This trimerization and tetramerization has been considered positive for process efficiency as only a single reactant is needed to create the carbohydrate. Though the presence of water can greatly control the selectivity of the 2MF polymerization, the conversion is low over solid acids and the best reported conversion from a heterogeneous catalyst is over Amberlist 15 [98]. Being a resin, Amberlist 15 would not be suitable for the single step reactor.

Interested in continuing to improve the single step process of section 4.2 for the generation of alkanes by consideration of sustainability and processing requirements, several screening reactions were performed to determine a suitable catalyst for the alkylation of furfural with butanal and levulinic acid with furfural.

4.2.1 Experimental:

Furfural (98%), Levulinic acid (98%), butanal (98%), 2-methylfuran (2MF) (98%), MCM-41 mesostructured aluminosilicate, methanol (99.8%), and Amberlyst-15 (hydrogen form) were purchased from Sigma-Aldrich and used as-received. ZSM-5 (Si/Al ratio of 80) was purchased from Alfa Aesar and was also used as received. Zeolite Y hydrogen 80:1 and 60:1, and SiAlO were purchased from Fluka, ZrP_2 was synthesized as described in section 3.1.1.

4.2.2 Furfural + butanal

A 15mL mixture of furfural and butanal (mole ratio of furfural: butanal was 2:1) was added to 0.22g of catalyst. Then the mixture was heated to 60-180^{o}C and magnetically stirred for 20hrs. After the reaction, the liquid product was filtered out and analyzed with gas chromatography or gas chromatography-mass spectrometry (GC-MS).

Upon the initial screening at 60°C of furfural +butanal with catalysts Al-MCM-41, Zeolite Y hydrogen (80:1 and 60:1), SiAlO, and ZrP_2, all conversions were observed at 1.2-1.4%. Elevating the temperature to 180°C, the reaction was screened with SiAlO and Al-MCM-41. These reactions had conversions of 5% and 10% respectively. Though previous studies utilized furfural with ketones, this shows that it also reacts with an aldehyde. The single step reactor requires high conversion of the condensation reaction step. It is possible that increasing the temperature more would increase conversion to usable amounts, but these results were not promising for the goal at hand.

4.2.3 Levulinic acid + furfural

A 15 mL mixture liquid of furfural and levulinic acid (mole ratio of furfural: levulinic acid was 1:2) was added to 0.22 g of catalyst. Then the mixture was heated to 60-180°C and magnetically stirred for 20hrs. After the reaction, the liquid product was filtered out and analyzed with gas chromatography or gas chromatography-mass spectrometry (GC-MS).

Initial screenings of a variety of acids led to either less than 1% conversion or uncontrollable polymerization forming a solid product. Understanding that furfural has been known to polymerize in acids, further screenings were performed with basic catalysts. For a baseline, NaOH was used. Previous reports found NaOH in water to be favorable for condensation of furfural and levulinic acid.[117] As confirmation of the reaction, 2.4g of NaOH was dissolved in 3mL of deionized water. It was then added to the 15mL reaction mixture of Levulinic acid and furfural. This resulted in complete consumption of the furfural. Though NaOH was verified to have favorable results, solid

bases did not perform as well. The use of CaO produced solids, and $MgAl_2O_4$ initially produced 8% conversion.

To focus more on $MgAl_2O_4$ as a potential catalyst for a single step production of diesel length alkanes involing levulinic acid and furfural, an attempt was made to reproduce the 8% conversion; however, the reaction polymerized completely. Upon completing synthesis of $MgAl_2O_4$, XRD had been used to confirm its structure. After the complete polymerization of this reaction, XRD was utilized again. The structure had clearly changed to a mix of MgO and Al_2O_3, see section 3.1.2. Upon re-calcining the catalyst, it reformed $MgAl_2O_4$, and the conversion of levulinic acid and furfural dropped to 2%. Concluding that the conversion of levulinic acid and furfural increases as the MgO and Al_2O_3 separated, it was decided that this would not be a good catalyst choice for the desired one step process. Uncontrolled polymerization of the reactants would certainly clog the flow reactor.

Seeing that increasing the conversion of the mixture of levulinic acid and furfural also increased the likelihood of uncontrolled polymerization, it was decided that the use of furfural should no longer be pursued for the single step process. Two years after this work was ceased because it would not serve the goal at hand, a different group published their successful results with these chemicals.[118] An important note is that they began by nutralizing the levulinic acid. Given that acids promote the polymerization of furfural, this step removed the acid while allowing the ketone to remain. They also found that MgO-Al_2O_3 could produce 100% conversion of furfural with only 7.1% from the aldol condensation of furfural and levulinc acid.

4.2.4 Conclusion of consideration of platform chemical processing steps

This screening method did not produced results adequate for the single step reactor. All too often, increasing temperature with any reaction that had furfural led to solid formation. The formation of solids in a flow reactor would not only clog the reactor but would render it unsafe to the user.

4.3 2-methylfuran as single reactant for production of crude substitute.

Beyond the concern about the source of the reactants for the single step conversion of waste derived chemicals to alkanes is the importance of the specific product obtained. The use of 2MF and butanal produced predominantly C9. This is at the low end of length that could be considered for diesel. The branching of the product is also important. Branching is needed in long molecules to reduce the boiling point and improve viscosity. To address both length and branching, research was given to the possibility of using 2-methylfuran as the sole liquid reactant for single step alkylation and hydrodeoxygenation.

Previous research has shown multi-step processes of converting 2-methylfuran to a C15 hydrocarbon through the 2-methylfuran trimer. The mechanism published for the first step states that water is required to open a 2-methylfuran ring which then combines with 2 rings that have not opened [97]. This was originally reported using sulfuric acid but was later shown to proceed with Amberlist 15 provided water was added [98]. One common concern is that this condensation can react past the trimer to larger oligomers and solidify. The next main steps in this process are the hydrogenation and hydrodeoxygenation of the trimer into the C15 hydrocarbon. These have been reported

simultaneously at 350°C and 725PSI[97] or individually at slightly lower temperatures.[42]

A water free option for fuel from 2MF utilizes the production of a 2MF tetramer to obtain a C20 hydrocarbon. As with the C15, this has been reported as a multistep process beginning with a batch reaction using Amberlist 15 followed by hydrogenation and hydrodeoxygenation over palladium and ruthenium catalysts [98]. To make either the C15 or the C20 hydrocarbon production processes more scalable, by using a single flow reactor like what was previously shown with the 4.2, would require a solid catalyst that could survive the temperatures required for hydrodeoxygenation, but Amberlist 15 is a resin which cannot handle those temperatures.

In the study of 2MF for hydrocarbon production, similar goals were maintained as were used in the single step process for 2MF and butanal. The first goal was the continuation a solvent free process which includes using no water. Organic solvents would require costly separation steps, and water as a solvent could require a costly water treatment after the reaction. Second, because hydrodeoxygenation is often performed at temperatures up to 350°C, a solid catalyst that is stable up to that temperature was needed. An additional consideration was present for this project that the process must minimize the formation of molecules larger than C20, referred to here-in as heavies. Diesel is a mix of hydrocarbons commonly C9-C23, if the oligomeration is permitted to proceed past the C20 tetramer, the chain length would be too long.

4.3.1 Experimental

2-methylfuran (2MF) (98%), Al-MCM-41 mesostructured aluminosilicate, and methanol (99.8%) were purchased from Sigma-Aldrich, and used as received, Pt/Al-

MCM-41 was synthesized as in 3.3.1, ZrP_2 was synthesized as described in 3.1.1, mesoporous alumino-silicate was synthesized by hydrothermal synthesis as described in section 3.2.

4.3.2 Atmospheric batch screening

Initial screenings were performed in 50mL refluxed flasks heated by oil bath. 10mL of 2MF and 0.22g of the chosen catalyst were magnetically stirred at 66°C for 20hrs. Each flask had over 2 feet of graham condenser that was chilled to 4°C using water pumped from an electric chiller. Anytime that these reactions were attempted without proper condensing, the 2MF evaporated giving the illusion of increased conversion. To insure this was not an issue, the mass of each loaded vessel was measured before and after each reaction. Only results without significant mass loss are shown in Table 4.2. Al-MCM-41 had 7% conversion and 97% selectivity to the tetramer. ZrP_2 had 3% conversion and 49% selectivity. Amberlyst 15 had 20% conversion and 54% selectivity.

Table 4.2 Initial screen of catalysts for 2MF tetramerization

Catalyst	Conversion	Tetramer Selectivity	Yield
Al-MCM-41	7%	97%	6.8%
ZrP_2	3%	49%	1.5%
Amberlyst 15	20%	54%	10.8%

Based on these initial screenings, Al-MCM-41 aluminosilicate was chosen for further study because it most closely met the goals. It is stable up to 800°C and provides high selectivity to the C20 precursor. It was observed that use of MCM-41 hinders the selectivity to heavies and it is speculated that this is due to the fact that most acid sites are

inside the channels of this molecular sieve where there is not ample room for the formation of larger products.

In an effort to increase conversion, mesoporous aluminosilicates similar to Al-MCM-41 were synthesized so that the Si/AL ratio could be adjusted. These catalysts had similar pore diameter to the Al-MCM-41. Characterizations are provided in section 3.2. The Si/Al ratio screen was performed with 4 hr reactions at 66°C. The results are shown in Table 4.3.

Table 4.3 Si/Al ratio screen performed at 66°C for 4 hours

MCM-41 Si/Al	Conversion	Selectivity to tetramer	Selectivity to heavies
∞	3.4%	100%	0%
100	5%	100%	0%
40	11%	96%	3%
20	33%	94%	5%

4.3.3 High pressure batch reaction

For its high conversion, the silicon/aluminum ratio of 20 was chosen for a high pressure batch reaction. It was hypothesized that the increased pressure and temperature would increase conversion of 2-methylfuran and maintain the high selectivity to the C20 precursor. Using the 150mL Autoclave Engineers batch reactor, 90mL of 2MF and 1.32g of Si/Al=20 aluminosilicate were reacted at 230°C and the total pressure was brought to 500PSI with He. These conditions were chosen because they match the best temperature and pressure used in the flow reactor in section 4.2. Five samples were drawn from the reactor over the 170min reaction. The conversion of 2MF reached 43% by end of the

reaction, but the selectivity to the C20 precursor dropped. Conversion and selectivity are shown in Fig. 4.4. Conversion and yield are shown in Fig. 4.5.

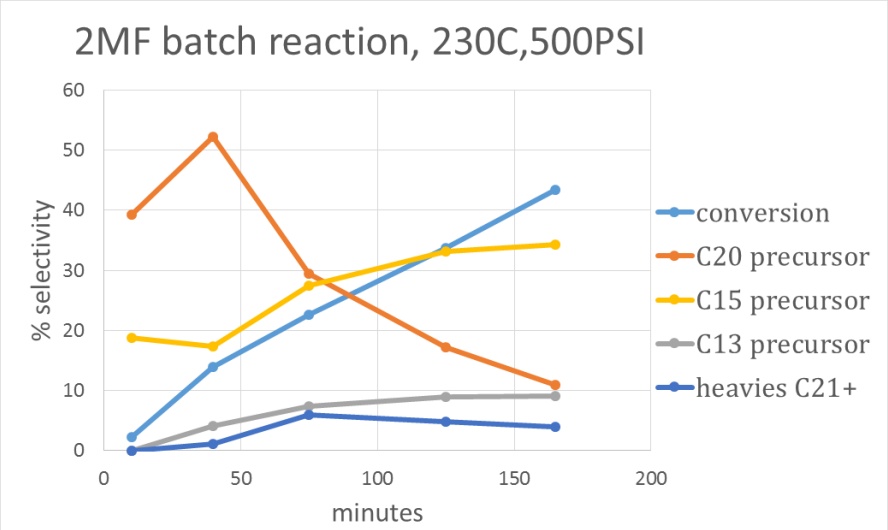

Figure 4.4 Selectivity of products for 500PSI batch reaction at 230°C. Pressure was built with He.

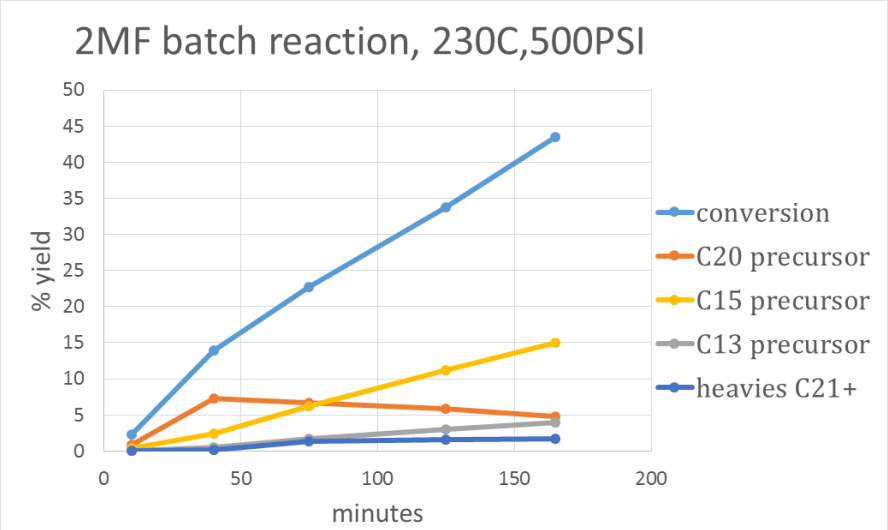

Figure 4.5 Yield of products for 500PSI batch reaction at 230°C. Pressure was built with He.

Though the selectivity to C20 dropped with time, the C15 precursor became the most selective product. This was not bad for the long term goal of producing diesel

length hydrocarbons because C15 is well within the desired range. It should be noted that the C15 precursor is reported in literature to require the presence of water[42], [97], but here it was made with 34% selectivity. Other products include a C13 precursor which appears to be part of a crack of the C20 precursor. As the selectivity to the C20 precursor decreases, the selectivity to the C13 precursor increases as well as an increase in selectivity to the C15 precursor. The graph of yield, Fig. 4.5, gives further support to the cracking of the C20 precursor because the yield decreases with time. The products not reported in the figures are too low in concentration to be identified.

Having shown the ability to produce a precursor mix between C13 and C20 that is predominantly C15, the above results were considered promising enough to continue to the next steps of attempting this reaction in the fixed bed reactor with flowing H_2 and Pt promoted catalyst. Unfortunately, with every attempt, the 2MF solidified on the sides of the reactor tube before reaching the catalyst. Several adjustments were made to attempt to avoid this, but nothing worked. The bed location was adjusted. The insulation at the entrance to the reactor was adjusted. All adjustments only accomplished moving the location of the solidified 2MF.

4.3.4 Conclusion:

Much of the preliminary work has been done to use 2MF as a sole reactant on a bifunctional mesoporous aluminosilicate promoted with Pt. Though it is contrary to one of the main goals of this project, it is likely that this reaction would be successful with a solvent. The single step reaction between 2MF and butanal was successful in the fixed bed reactor. Though the butanal was a reactant, it may have acted as a solvent for the

2MF before reaching the catalyst bed. One positive result of this work is that a method was shown that produced the C15 precursor from 2MF without the addition of water.

CHAPTER 5:

STRUCTURAL DETERMINATION OF RHENIUM OXIDE ON CERIUM OXIDE

Rhenia (ReO_x) on Ceria (CeO_2) functionalized with Palladium has been reported to be more active for simultaneous hydrodeoxygenation (HDO) of hydrocarbons than ReO_x on other supports [44], [51]. Though this benefit could simply be from the oxygen storage properties of the support or from the PdO crystallite size, it is natural to presume that this could be the result of a structural difference of the ReO_x when supported on the cubic fluorite CeO_2. [53] While the structure of ReO_x on other supports has been widely studied as discussed in section 1.3, research into the structure of ReO_x on cerium oxide is lacking.

5.1 Experimental:

Various loadings of ReO_x/CeO_2 and ReO_x-Pd/CeO_2 were prepared by wet impregnation following the method presented in section 3.3.2. CeO_2 used here was donated by Daiichi Kigenso Kagaku Kogyo Co., Ltd. Ammonium perrhenate (≥99%) and palladium (II) nitrate were purchased from Aldrich. After completing the synthesis with a 500^{o}C calcination, samples have their Re weight loading confirmed by ICP. The Re ICP samples are made by heating a theoretically 50 PPM mixture of catalyst in HCl to 110^{o}C for 12 hrs. Digesting in Aqua regia was also attempted, but it did not dissolve the Re completely as was evident by ICP results far below those from samples digested in HCl.

XRD was performed to check for inconsistencies in synthesis such as agglomeration of Re or Pd or a change in crystallinity of the CeO_2. For XRD, samples were deposited on zero-background plates using ethanol. Scans were run at 1^o/minute or slower. TPR was used to monitor the changes in reduction temperature that were caused by loading. XPS was used for oxidation state of the Re and the surface of the cerium oxide support. In XPS, various pretreatments were performed including oxidation and reduction. Those specifics will be included with the data presented. FTIR and Raman also had various pretreatments as discussed later.

5.2 XRD and ICP of ReO_x/CeO_2

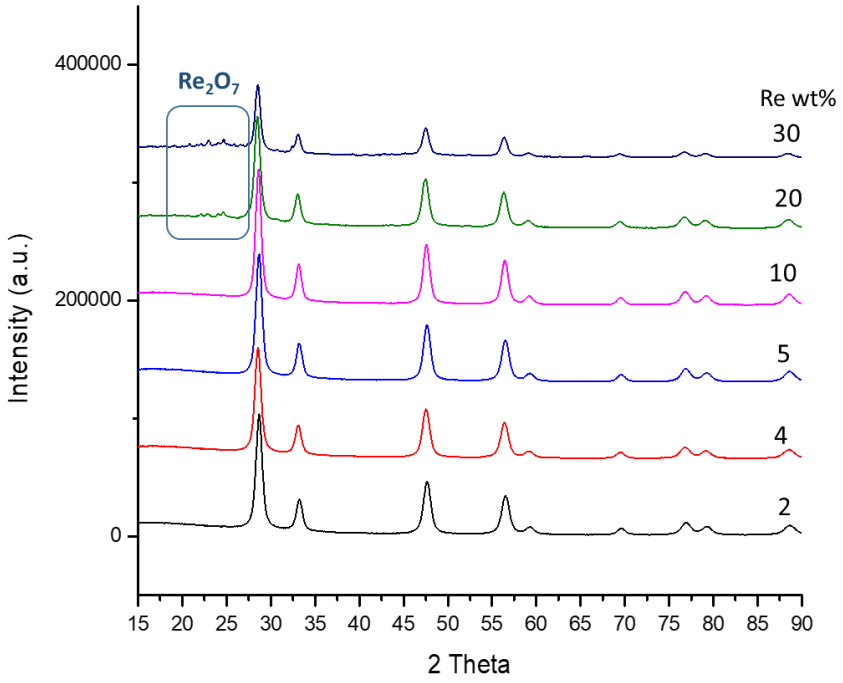

Figure 5.1 XRD of fresh CeO_2 and various loadings of Re. Nominal loadings of Re wt% are shown.

XRD patterns were obtained for multiple Re loadings of ReO_x/CeO_2 as well as the clean support. As seen in Fig. 5.1, the addition of ReO_x does very little to the XRD

patterns. Except for the highest loadings, ≥20 wt% Re, all of the diffraction peaks belong to CeO_2. At the highest loading of ReO_x, small peaks appear in the region of 22-25 2θ that are consistent with Re_2O_7. These include 21.98 2θ for (1 2 1), 22.85 2θ for (0 0 4), and 24.13 2θ for (1 2 1).[119] Based on these diffraction peaks, the Rhenia in these high loading samples cannot be considered to be isolated as they contain solid Re_2O_7 crystallites. Because the CeO_2 peaks are consistent in breadth across all weight loadings, it is clear that the CeO_2 crystallinity is not being effected by the addition of ReO_x. Based on Scherrer's equation [120], the grain size of this Ceria support is 15nm. Using nitrogen adsorption, this Ceria support has a surface area of 92.44±0.34 m^2/g.

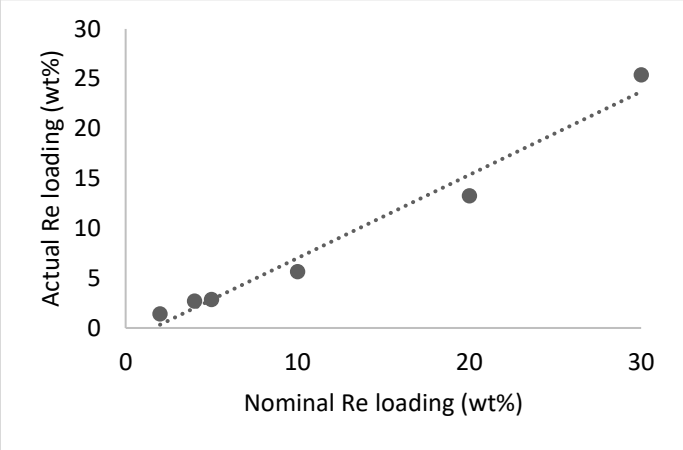

Figure 5.2 Actual Re wt% as determined by ICP

ICP was performed to compare the actual loading of Re with the nominal loading and the results are displayed in Fig 5.2. As seen by the linear trend line, it does not appear that the highest possible loading has been achieved. Rhenia on other oxide supports asymptotically approaches a maximum loading. For example, the maximum loading on ReO_x/Al_2O_3 has been reported as 13 wt%.[58] This maximum loading is attributed to the high volatility of Re_2O_7. It is hypothesized that at low loadings the ReO_x

is isolated but as surface density becomes too large, the isolated ReO_x combine to form Re_2O_7 and subsequently vaporize.[58], [60] The linear trend in Fig. 5.2 implies that the Re_2O_7 is not vaporizing from the CeO_2 surface. However, with the high Re loading achieved, as high as 25wt% by ICP, it is impossible that the ReO_x is remaining isolated. The Re_2O_7 diffraction peaks along with the ICP indicate that solid Re_2O_7 is forming and remaining on the surface after 500°C calcination

Due to the high volatility of Re_2O_7, which sublimes at 300°C, it is seldom reported to have solid Re_2O_7 present after a 500°C calcination [121] and unprecedented to have XRD evidence of its existance. To understand this phenomenon, a calcination study was performed with 30wt% ReO_x/CeO_2. This sample was synthesized using the normal procedure, except the final calcination was not performed immediately. The uncalcined sample was divided into several parts to be calcined at various temperatures. These samples were then analyzed with XRD and ICP, Fig. 5.3 and Table 5.1 respectively.

The XRD patterns, Fig 5.3, reveal that the uncalcined 30wt%ReO_x/CeO_2 contains ammonium perrhenate, the rhenium precursor used for these catalysts. Though NH_4ReO_4 is readily soluble in water, it recrystallizes when dried in the presence of ammonia. As the synthesis technique had no method of removing the ammonia from the solution before drying, excess rhenium recrystallized as NH_4ReO_4. Upon calcination, the ammonium perrhenate crystals thermally decomposed forming the Re_2O_7 crystals as seen with 500°C calcination. However, no Re_2O_7 is seen through XRD with calcination temperatures of 700°C and higher. Additionally, the increased calcination temperature decreased the FWHM of the CeO_2 peaks.

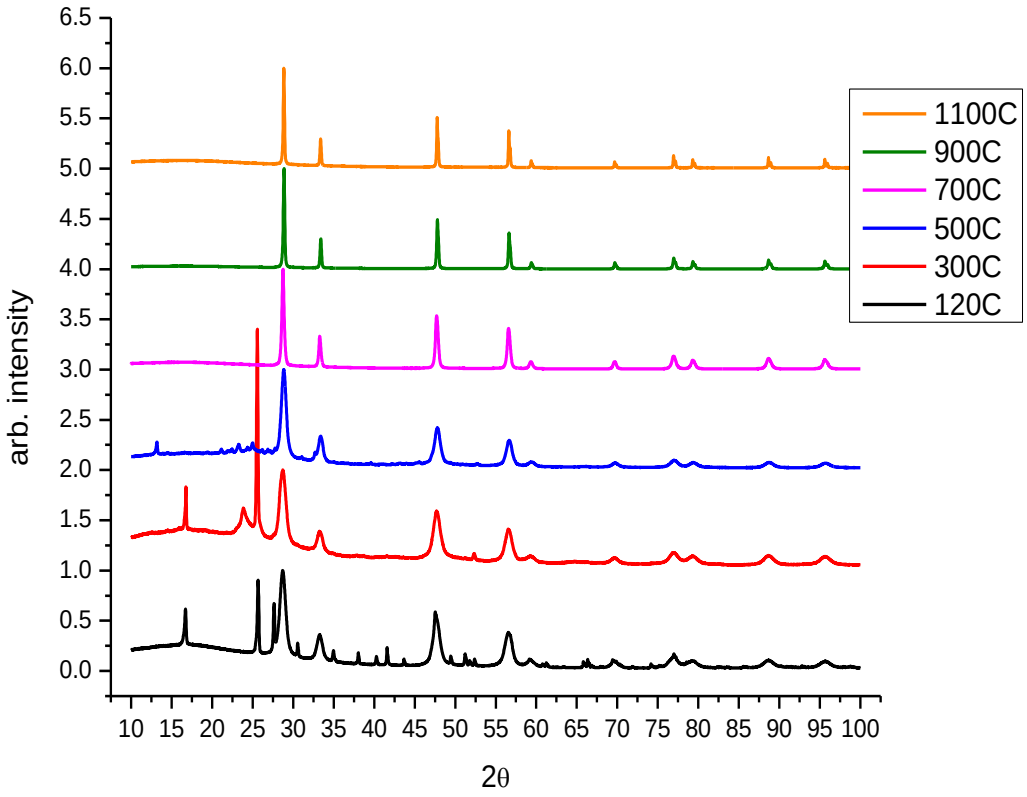

Figure 5.3 XRD patterns of 30wt% ReO_x/CeO_2 calcined at multiple temperatures. The pattern for 120°C represents the sample that was dried but not calcined.

Table 5.1 Re loadings of 30wt% calcination study

Calcination temperature (°C)	Loading measured by ICP (wt%)
120	18.5
300	24.2
500	24.7
700	0.002
900	0
1100	0

ICP was used for the samples of nominally 30wt% that had been calcined at various temperatures, see Table 5.1. The result for the uncalcined sample was lower than expected, only 18.5wt%, but this could be due to the ammonium perrhenate not dissolving well in HCl. The 300°C and 500°C samples had loadings as expected. Consistent with the XRD findings, there was a sharp decrease in the Re loading with calcination temperatures of 700°C and higher. From the results of XRD and ICP, it is seen that the Re_2O_7 is not forming until calcination and that it vaporizes at a temperature between 500°C and 700°C.

5.3 Temperature Programmed Reduction of multiple Re loadings of ReO_x/CeO_2

Previous studies with ReO_x on oxide supports have reported that increasing the loading of Re decreases the reduction temperature. [58] This is because increasing loading requires the ReO_x to attach at weaker bonding sites as the stronger sites are consumed. Also, supported rhenium oxide is known to auto-induce reduction[122]. This auto-catalytic process, indicative of sharp TPR peaks, is two-fold in meaning. First, when reduction begins, all of the rhenia reduces completely to metal. Also, as the rhenium from the weaker sites is reduced, it stimulates the more strongly attached species to reduce as well resulting in a single reduction peak[58]. This has been observed for Al_2O_3, ZrO_2, TiO_2, SiO_2, and carbon supports [58], [122].

In this study using CeO_2 support, the TPR results are not consistent with rhenia on other oxides, see Fig. 5.4. For the low weight percents (below 5wt%), there are multiple reduction events observed showing that the rhenia does not reduce completely to metal at the start of reduction. Also, the reduction temperature jumps from 175°C for the 3 and 4 wt% ReO_x to over 300°C for the 5wt% matching the reported Re_2O_7 reduction

temperature[122]. The surface species that were present at the lower loadings are no longer present in the 5wt% and higher. Though crystalline Re_2O_7 was not evident with XRD until 20wt%, the TPR implies that the Re_2O_7 could be formed at loadings as low as 5wt%

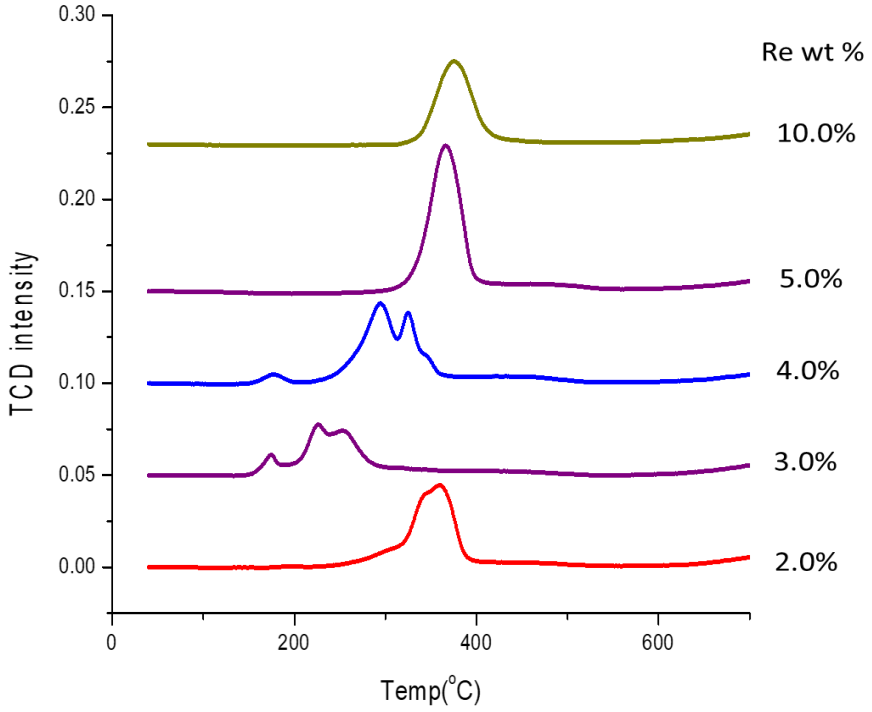

Figure 5.4 Temperature Programmed Reduction of multiple Re loadings on ReO_x/CeO_2

5.4 X-ray photoelectron spectroscopy of ReO_x/CeO_2

To further explore the loading effects of Rhenia, XPS was performed as shown in Fig 5.5. After calibrating the C 1s peak binding energy to 284.5 eV, the Re peaks were fit. Peaks were fit with a binding energy delta of 2.43eV, area ratio $4f_{\frac{5}{2}}/4f_{\frac{7}{2}} = 0.75$, FWHM $4f_{\frac{5}{2}}$ =FWHM $4f_{\frac{7}{2}}$. All loadings of Re on untreated ReO_x/CeO_2 contain Re^{VII}. At 5wt% Re, there is evidence of charging as is shown in red in Fig 5.5. When charging

is present, false peaks or shouldering occurs at slightly higher binding energies than the main peaks.[123] With charging present, error in peak fitting is increased, but information is still gained from the presence or absence of peaks. Charging was evident on loadings of 5% and higher and also on any sample containing Pd.

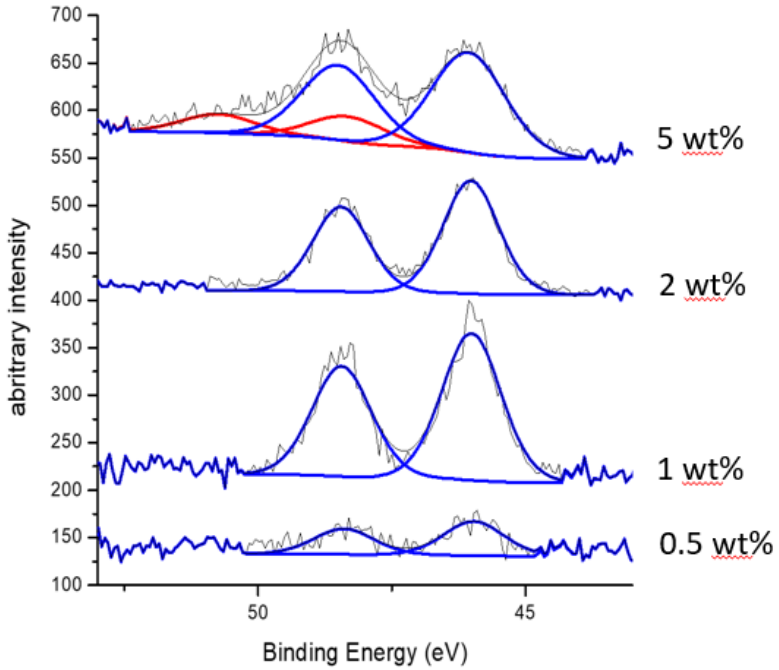

Figure 5.5 X-ray photoelectron spectroscopy with no pretreatment. The blue peaks represent Re^{VII}. The red peaks mark an example of charging.

To insure that no permanent change occurs with reduction and re-oxidation cycles, 2wt% ReO_x-0.3wt%Pd/CeO_2 was treated in situ, see Fig 5.6. After reducing at 200°C for 1 hour, the Re was not fully reduced nor was the cerium oxide surface reduced, see Fig. 5.6. At 200°C, Re was present as Re^{VII}, Re^{VI}, and Re^{0}. These multiple states further support what was observed in TPR that ReO_x/CeO_2 does not auto catalytically reduce. After further reduction at 500°C, the Re reached its metallic state and the CeO_2 surface was partially reduced to Ce_2O_3. As 500°C is not hot enough to reduce the bulk CeO_2, this reduction is localized to the surface. The reduced sample was then oxidized

and the rhenium oxide returned to Re^{VII}. After reduction and re-oxidation, there was no carbon peak to use for the calibration. Therefore, calibration was done by setting the highest binding energy CeO_2 peak to 917eV. This is not a common practice, but this peak does not overlap with any other CeO_2 or Ce_2O_3 peak.

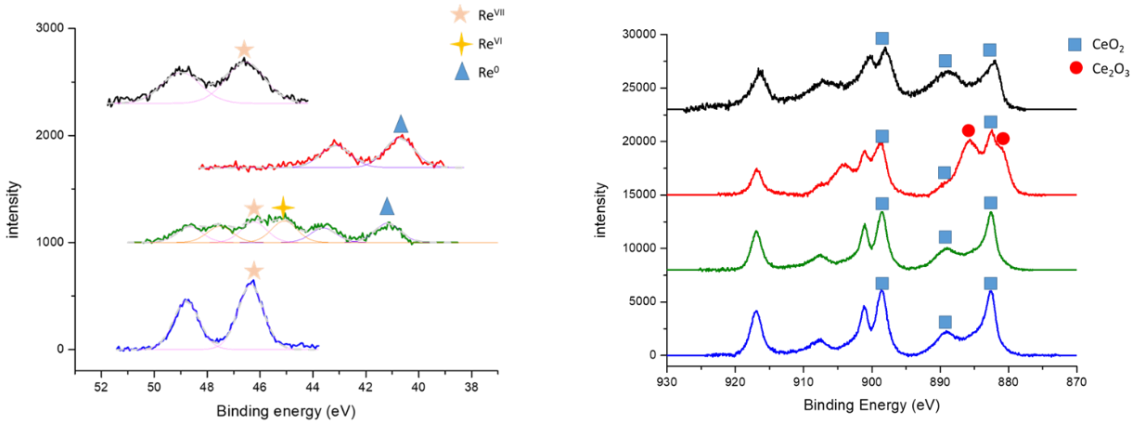

Figure 5.6 XPS of 2wt%Re-0.3wt%Pd/CeO_2. From bottom: blue trace is fresh catalyst, green trace is reduced at 200°C, red trace is reduced at 500°C, and black trace (top) is reoxidized at 200°C.

5.5 Raman and IR

As presented in section 1.4.2, reported Raman of supported rhenia in ambient conditions is very consistent without dependence on loading or support. Raman of supported ReO_x in ambient conditions has previously only been reported to have 2 peaks in the 800-1050cm^{-1} region which are unambiguously assigned to the symmetric and anti-symmetric stretches of terminal Re=O and are found at 967-982cm^{-1} and 916-930cm^{-1}, respectively, for supports of ZrO_2, TiO_2, Al_2O_3, and SiO_2. [57], [58], [124]–[126] These previously reported Raman bands are independent of loading [57], [58] with the exception that the anti-symmetric stretch is sometimes not visible. [125] The previous band assignments for ambient conditions align with the band positions of aqueous ReO_4^-.

Because ReO_x is highly soluble in water, it is believed that ambient conditions provide enough surface water for the surface adsorption bonds to hydrolyze rendering the ReO_x to be unattached to the surface[58], [124], [126]. Upon dehydration of ReO_x on other supports, the terminal Re=O symmetric vibrational bands shift to higher wave numbers, 995-1018cm^{-1}, due to shorter bond length. The antisymmetric band is then reported at either 970-980cm^{-1}, or 880-890cm^{-1}[58]. The 880-890cm^{-1} peak location is said to be from a distortion in the tetrahedron caused by bonding to the support.

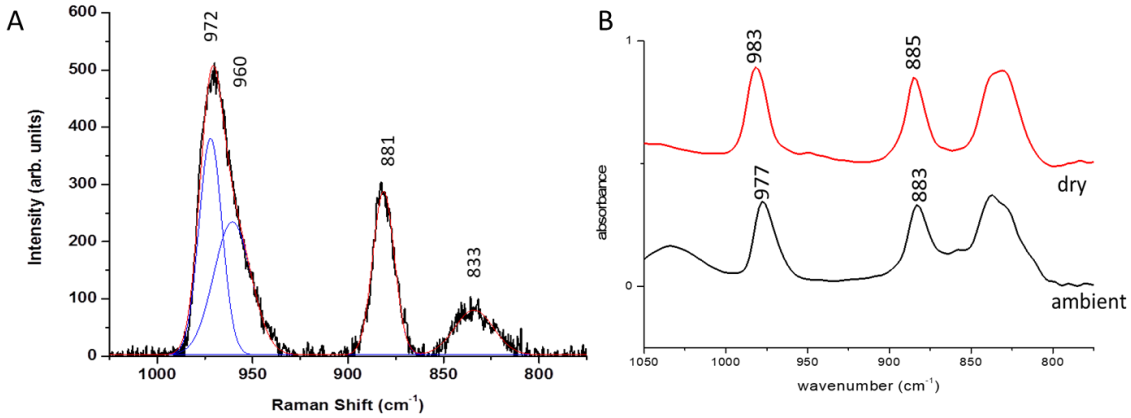

Figure 5.7 A: Ambient Raman of 1wt% ReO_x/CeO_2. B: Ambient and dried FTIR of 1wt% ReO_x/CeO_2.

1wt% ReO_x/CeO_2 was observed in ambient conditions in Raman. For ambient conditions, Raman is preferred over FTIR because the Re=O symmetric stretch of hydrolyzed ReO_4^- is not visible in FTIR[58]. The Raman spectrum is presented above in Fig 5.7A. The 1wt%ReO_x/CeO_2 has a double peak at 972 cm^{-1} and 960 cm^{-1} as well as a peak at 881 cm^{-1} and a very broad peak at 833 cm^{-1}. These peaks cannot be explained by the literature reports above, and the 881 cm^{-1} peak implies that the ReO_x is bonded to the surface in ambient conditions instead of being hydrolyzed. To aid in discovering the peak assignments, FTIR was performed on the same sample in both ambient and dried

condition, see Fig 5.7B. For the dried spectrum, the sample was dried in the DRIFTS reaction cell by flowing H_2 and heating the sample to 150°C. The spectrum was then taken in a He atmosphere at 100°C. The FTIR spectrum for ambient conditions is consistent with that of Raman except that the 960cm^{-1} peak is not active in FTIR.

The Raman peak at 975cm^{-1} is assigned to the symmetric stretch of Re=O. The fact that this peak is visible in FTIR further supports that the ReO_x is attached to the surface. Were the ReO_x not attached to the surface, the Re=O symmetric stretch would not be visible in FTIR because it would not produce a change in dipole moment[58]. The Raman peak at 962cm^{-1} is at lower wavenumber than what is normally observed in ambient conditions for the symmetric stretch of Re=O (967-982cm^{-1}), but it is high for the anti-symmetric stretch (916-930cm^{-1}). The reference spectra of $NaReO_4$ has a Raman stretch of 958cm^{-1} for the symmetric stretch of Re=O. Given that this peak is not visible in FTIR, it is not an anti-symmetric stretch. By elimination, 962cm^{-1} must belong to a symmetric Re=O stretch, but this necessitates that a second species is present as each species may only have one symmetric Re=O stretch. This second species is not adsorbed to the surface rendering its Re=O symmetric stretch inactive in FTIR. This is the only supported ReO_x with these peaks under ambient conditions and also the first supported ReO_x in which some of the ReO_x is actually chemisorbed to the support in the presence of water.

5.5.1 Pretreatment/temperature effect on FTIR spectra

Using the Harrick Scientific Praying Mantis DRIFT reaction cell of the FTIR a series of pretreatments was performed on 0.25wt%ReO_x/CeO_2 and the CeO_2 support to see the effect of drying and calcination. A background spectrum was measured using a

mirror in place of the reaction cell. A powder sample was then loaded into the cell. The CeO_2 support was dried at 100°C under 40sccm helium flow for 1 hour and a spectrum was measured, Fig 5.8a . In the 800-1100cm^{-1} wavenumber range, two peaks were seen which are attributed to carbonates. The presence of these carbonates is likely from exposure to air. They are not contamination from synthesis because the sample was calcined as the final synthesis step. For 0.25wt%ReO_x/CeO_2, an initial spectrum, Fig 5.8b, was measured at 100°C within 5 minutes of beginning the heating and flow of helium, 40sccm. The sample was heated to 100°C and remained under the flow of He for 2 hrs. This resulted in a peak shift from 975 to 979 cm^{-1}, Fig 5.8c, because the removal of water allowed the Re=O bond to shorten.

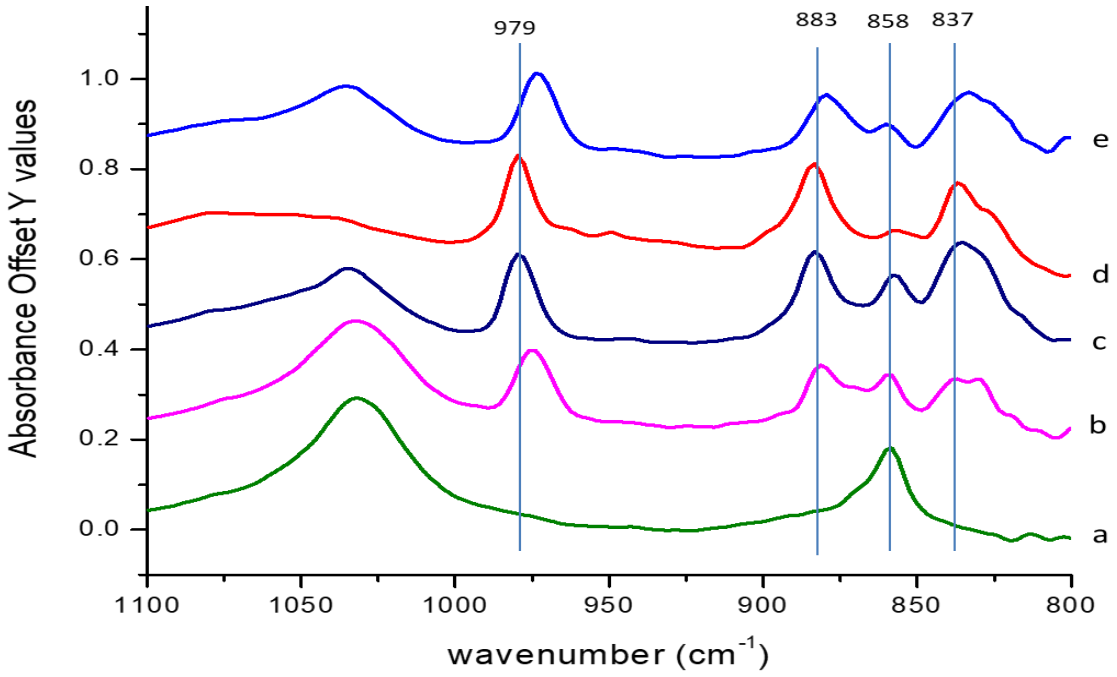

Figure 5.8: ReO_x region FTIR: Drying and calcination:a: CeO2, b-e: 0.25wt%ReO_x/CeO_2. a:dried in He at 100°C for 1 hour, Spectrum taken at 100°C. b:initial scan- spectrum taken as soon a temp reached 100°C in He flow. c: dried. Spectrum taken after 100°C was maintained for two hours in He flow. d: calcined. Temperature was raised to 400°C under the flow of zero-air. Spectrum was taken after temperature was decreased to 100°C. e: after exposure to ambient conditions, spectrum was taken at 25°C under He flow.

The sample was then calcined by heating to 400°C for an hour under the flow of zero air, 40sccm. Upon cooling to 100°C another spectrum was measured, Fig 5.8d. Here it is seen that the carbonate peaks from the bulk CeO_2 are greatly reduced. The gas flow was stopped and the sample was left open to ambient conditions. Twelve hours later, under the flow of helium, a spectrum, Fig 5.8e, revealed that the carbonates returned and the 979 cm^{-1} peak shifted back to 975 cm^{-1}. This confirmed that the carbonates are present due to exposure to ambient air. For cleaner FTIR spectra, without carbonate peaks, the pretreatment procedure was altered to calcine at 550°C.

5.5.2 Loading effects on FTIR spectra

Knowing that solid Re_2O_7 was evident at elevated Re loadings in XRD (section 5.2) and TPR (section 5.3), multiple ReO_x loadings were studied in the FTIR, Figs 5.9 and 5.10. These were dried at 550°C in air for 1hr and then cooled to 100°C for the spectra to be recorded. The spectra were recorded under the flow of He. The spectra for 4 and 5 wt% ReO_x/CeO_2 contain peaks for solid Re_2O_7 [55], [57], [58]. Crystalline Re_2O_7 is composed of both octahedral ReO_6 and tetrahedral ReO_4[57], [58]. The units are linked by oxygen bridges in a double layer structure. The weak van der Waals forces between the layers produce the complicated spectral pattern [57].

This FTIR evidence of solid Re_2O_7 in the 5wt% sample is consistent with the TPR for 5wt% ReO_x/CeO_2. The TPR for 4wt%ReO_x/CeO_2 had the same initial reduction peak as 3wt%, but the 2nd and 3rd reduction peaks were at higher tempertures than with the 3wt%. It is likely that the 4wt% ReO_x/CeO_2 is in the transition to solid Re_2O_7. Part of the ReO_x is in solid form, so the FTIR peaks for solid Re_2O_7 are present. Part of the ReO_x is not in solid form, so the lower TPR peaks are present.

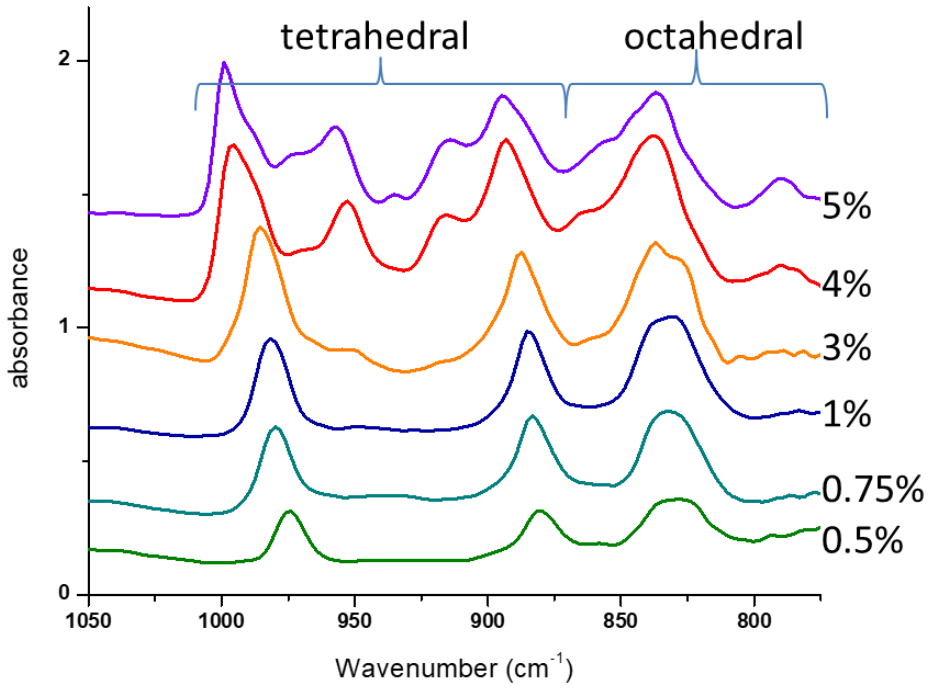

Figure 5.9 FTIR spectra of various Re loadings of ReO_x/CeO_2. Samples were calcined in situ and spectra were recorded at 100°C

The broad 833-837cm^{-1} peak is present at all loading. From the peak assignments of Re_2O_7 in literature[55], [57], [58], the peaks below 870cm^{-1} belong to the octahedrally coordinated portion of Re_2O_7. This shows that both tetrahedrally coordinated ReO_x and octahedrally coordinated ReO_x are present on CeO_2 at all loadings.

Loading effects were also observed in the hydroxyl region, Fig 5.10. The peak at 3585cm^{-1} increases in intensity with increased loading. This observation is exactly opposite of what is known to occur with ReO_x/Al_2O_3 where the hydroxyl sites are consumed with increased ReO_x coverage. This FTIR peak at 3585cm^{-1} was investigated more by monitoring its change with elevated temperatures, Fig 5.11. The 1wt%ReO_x/CeO_2 sample was calcined in dry air at 500°C to remove water and then cooled to 22°C. As the temperature decreased, the temperature was maintained at various

temperatures for 10 minutes to stabilize and have spectra recorded. After cooling, the temperature was increased, and for each temperature, no difference was seen in the spectra from the spectra recorded during the temperature decreasing. The spectra shown in Fig 5.11 were recorded as the temperature was decreasing. With increased temperature, the peak at 3585cm^{-1} decreases in intensity showing that the presence of OH group is temperature dependent. As the sample was calcined *in situ* before this temperature ramp, the presence of the OH group is not caused by surface water.

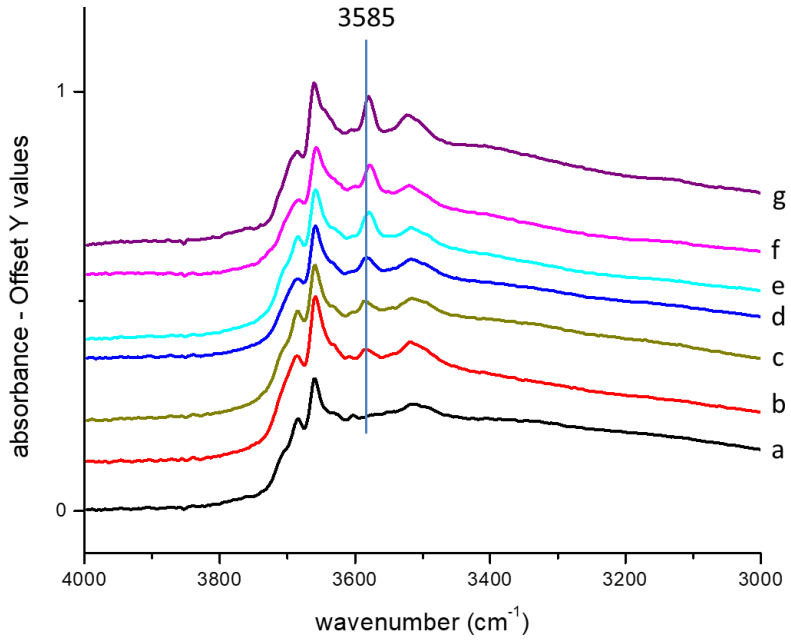

Figure 5.10 Hydroxyl Region FTIR: loading effect; a:CeO_2, b-g: ReO_x/CeO_2 dried at 150°C Spectra recorded at 100°C. b:0.25wt%Re, c:0.5wt%Re, d:0.75 wt%Re, e:1wt% Re, f: 1.5 wt% Re, g:3wt% Re

It is possible that this OH group is serving as a cross-linkage between two ReO_x, forming a dimer. This was mentioned as a possibility by Lacheen et. al.[127] who grafted Re_2O_7 onto ZSM-5. Though the catalysts in the present study were formed with wet impregnation, the calcination study showed that ammonium perrhenate is present

until calcination when it decomposes to Re_2O_7. If the OH is the crosslinkage of a dimer at low temperatures, it is likely forming an O crosslinkage at higher temperatures.

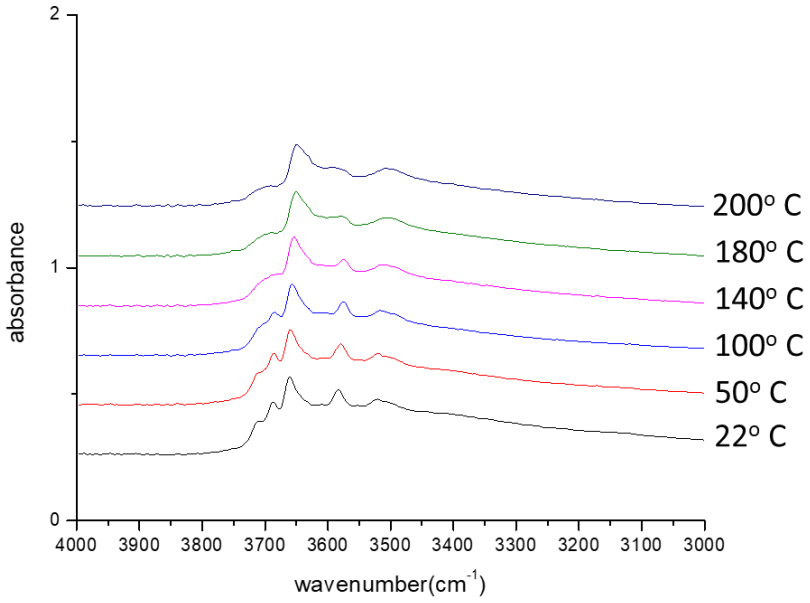

Figure 5.11 Hydroxyl region FTIR: effect of temperature. 1wt%ReO_x/CeO_2 at various temperatures under flowing air. Sample was calcined at 500°C in air before spectra were taken.

The fact that low loadings of ReO_x have an OH group at temperatures below 100°C is supported by a recent DFT study of isolated ReO_x. [54] In the DFT study, several possible structures of isolated ReO_x/CeO_2 were studied and it was determined that below 100°C, the most stable structure had one terminal double bonded oxygen and one OH group. Though the DFT study cannot be directly compared to this work because it was done on a fully hydroxylated CeO_2 surface, it does show the possibility of having an OH group on the ReO_x species. The DFT study shows the Re bonded to 3 support oxygen making the Re five coordinated. The spectroscopy in this current work shows that the Re must be tetrahedrally coordinated. Given the current spectroscopy and the previous DFT, the low loading, low temperature ReO_x/CeO_2 can have 3 of its four points

of coordination assigned. It has at least 1 terminal oxygen Re=O, at least one Re-OH bond, and at least one Re-O-Ce bond. The fourth Re coordination could be a second of any of those or a bond to the octahedrally coordinated portion of the sample.

5.5.3 $^{18}O_2$ substitution

To determine the number of Re=O bonds per ReO_x, an $^{18}O_2$ substitution study was performed in FTIR, Fig 5.12. Similar studies[59], [60] were discussed in section 1.4.3. 0.25wt%ReO_x/CeO_2 was calcined at 500°C. It was then reduced and reoxidized with $^{18}O_2$. Two reduction/reoxidation cycles were performed. As oxygen substitution continues, only one new Re=O peak is formed showing that the tetrahedrally coordinated portion of this sample has only 1 Re=O bond. Though this does not fully determine the structure, it does decrease the possible structures.

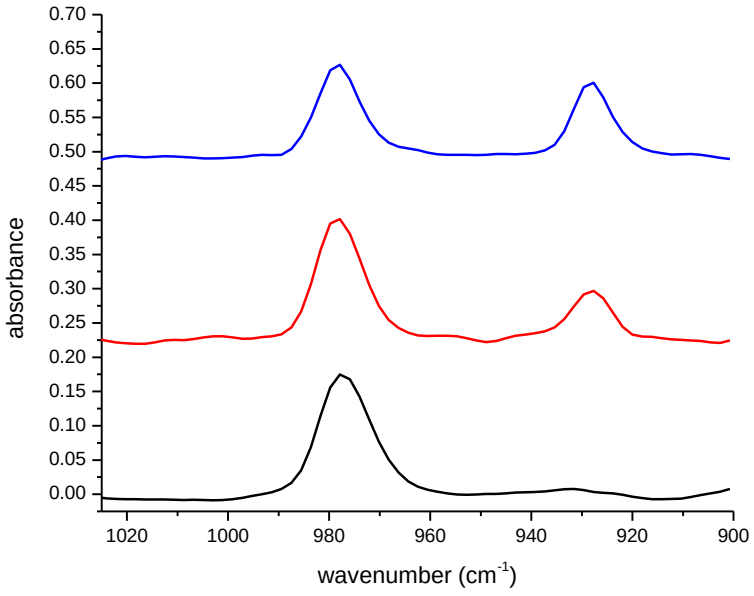

Figure 5.12 oxygen substitution on 0.5wt% ReO_x/CeO_2. Black trace (bottom) sample was reduced and reoxidized with air. Red trace (middle), sample was reduced and reoxidized with $^{18}O_2$. Blue trace (top), sample was again reduced and reoxidized with $^{18}O_2$.

5.5.4 Reduction of 2wt% ReO_x-Pd/CeO_2 in FTIR

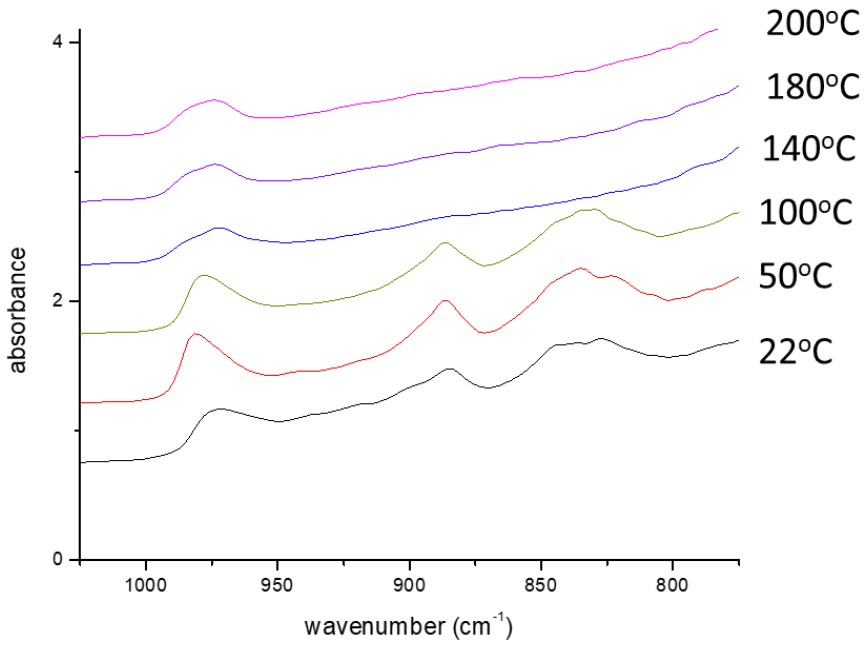

Figure 5.13 FTIR spectra of 2wt%ReO_x-0.3wt%Pd/CeO_2 reduced in H_2

The 2wt% ReO_x-Pd/CeO_2 sample was loaded into the DRIFT reaction cell. Without calcining, the cell was flushed with He and then 40sccm H_2 flow was started. As the temperature was elevated, a sudden change was noticed between 100°C and 140°C, Fig 5.13. At 140°C and above, the 880cm^{-1} peak and the 833cm^{-1}peak have completely diminished. This information can be used in conjunction with XPS, Fig 5.6a. From XPS results, as the ReO_x begins to reduce, it goes from Re^{VII} to Re^{VI} before going to Re^0. Re^0 would not be visible in FTIR. From the spectra in figure 13, it is seen that the octahedrally coordinated portion of the sample is first to reduce, but its reduction is simultaneous with the loss of the 880cm^{-1} peak. The remaining IR peak around 970cm^{-1} must be Re^{VI}, but this peak was present before reduction and must have been Re^{VII}.

Thus, the loss of the 880cm^{-1} peak is co-occuring with the reduction of the tetrahedrally coordinated species from Re^{VII} to Re^{VI}. Hence, the 880cm^{-1} peak must be assigned to the cross linkage between the tetrahedrally coordinated ReO_x and the octahedrally coordinated ReO_x. As the octahedrally coordinated ReO_x reduces, the cross-linkage is lost. This leaves isolated, tetrahedrally coordinated ReO_x with a single terminal oxygen which is consistant with the DFT study found here[54].

5.6 Conclusion

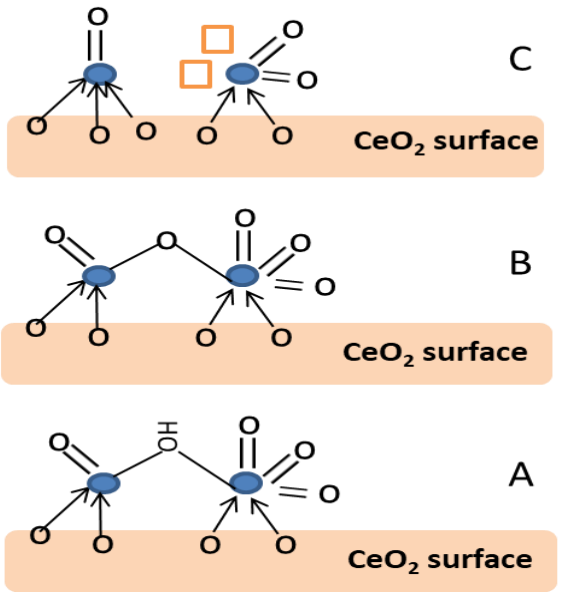

Figure 5.14 Possible structures of low loadings of ReO_x/CeO_2. A is at temperatures below 100^{o}C. B is at elevated temperatures in air. C is during H_2 reduction at 140^{o}C.

The structure of ReO_x/CeO_2 has been investigated and discussed. Using multiple characterization techniques, it was shown that ReO_x/CeO_2 with 5wt%Re and higher contains solid Re_2O_7. Low loadings in ambient conditions have cross-linked Re_2O_7 species adsorbed to the CeO_2 surface, see Fig 5.14A. This dimer consists of a

tetrahedrally coordinated half and an octahedrally coordinated half, similar to the building blocks of crystalline Re_2O_7. The isotope study revealed that the tetrahedrally coordinated half of the dimer has a single Re=O. With elevated temperature, the OH peak, discussed with Figs 5.10 and 5.11, dries to form the structure shown in Fig. 5.14B. Upon reduction in H_2, the octahedrally coordinated half of the dimer reduces first leaving isolated, tetrahedrally coordinated ReO_x with a +VI oxidation state similar to what is drawn in Fig. 5.14C.

CHAPTER 6

ADAPTATION OF GAP DECOMPOSITION FOR SUB-MONOLAYER DOSING OF P_2

Surface reconstructions are a classic area of study in the field of surface science, but the desire to have a phosphorous adsorbate can lead to many challenges, especially when safety is considered. The traditional use of PH_3 as a phosphorous source [128], [129], being a gas, had ease of use and the coverage could be easily controlled. However, PH_3 is highly toxic and can condense on the chamber walls as P_4, white phosphorous. White phosphorous ignites in air at room temperature. This results in sudden burning when the vacuum chamber is eventually opened. Red phosphorous, amorphous P_n, is safe to handle in air. It can be used as a phosphorous source because it will sublime predominantely as P_4 [130] which can be cracked at 1000^{o}C to P_2 [131]–[133]. Provided the P_2 is rapidly cooled it will condense as red phosphorous. Though this is safer than the traditional use of PH_3, there are still safety risks involved. The P_4 does not always fully crack to P_2, and red phosphorous crackers also suffer from burning when opened to the atmosphere.

In 1985, Mondry et al. reported a method of using GaP to produce P_2 by using a tantalum scavenger[134]. As GaP is heated, P_2 has a higher vapor pressure than Ga_2. GaP condenses on the tantalum scavenger, but the excess P_2 is released for dosing which produces a clean P_2 stream. GaP effusion cells are now well accepted and available for

purchase, however they are used for MBE with large coverages[135]–[139], micrometers thick.

Here-in is reported the adaptation of Mondry's method for submonolayer P_2 dosing. Consideration is given not only to the purity of the P_2, but also the ability to remove surface contaminations from both the single crystal being dosed and the P_2 source. To demonstrate the ability to reproduce the overlayers previously reported from dosing PH_3, the adapted P_2 doser is used to reproduce the LEED patterns previously reported on Ni(111). [128], [129] This opens the door for further surface science studies with phosphorous adsorbate using GaP as the source.

6.1 Down sizing the tantalum scavenger

The first step in adapting the GaP decomposition source for the purpose of sub-monolayer doses was to down size it. The original doser reported by Mondry was designed for an MBE furnace. Like the one reported here [136], it likely had a crucible on the order of 80mL. Our chosen heating method for this purpose was a 1mL alumina crucible heated by a tungsten wire, see Fig. 6.1a. The majority of the inner diameter of the crucible was 8mm, but it was beveled so the inner diameter at the top was 10mm. Due to this, it was decided that the tantalum scavenger should have a cone shaped bottom allowing it to rest inside the crucible. Three pieces of tantalum were spot welded together to form the scavenger in such a manner that vapors could not escape the crucible without touching at least one surface of the scavenger, see Fig 6.1c. The bottom piece was a cone with bottom diameter of 8mm, top diameter of 10mm and side length of 4mm allowing it to fit inside the alumina crucible. The center piece was a 10mm diameter disk with 2mm wedges removed from the outer circumference which was spot welded to the

top of the first piece. The top piece was another cone with lower diameter of 12mm, top diameter of 3mm and side length of 6mm which sat atop the other pieces and extended beyond the edge of the crucible. A picture of the scavenger resting in the crucible is shown in Fig. 6.1b. This scavenger was fabricated at Hokkaido University by the I-Cat fabrication center.

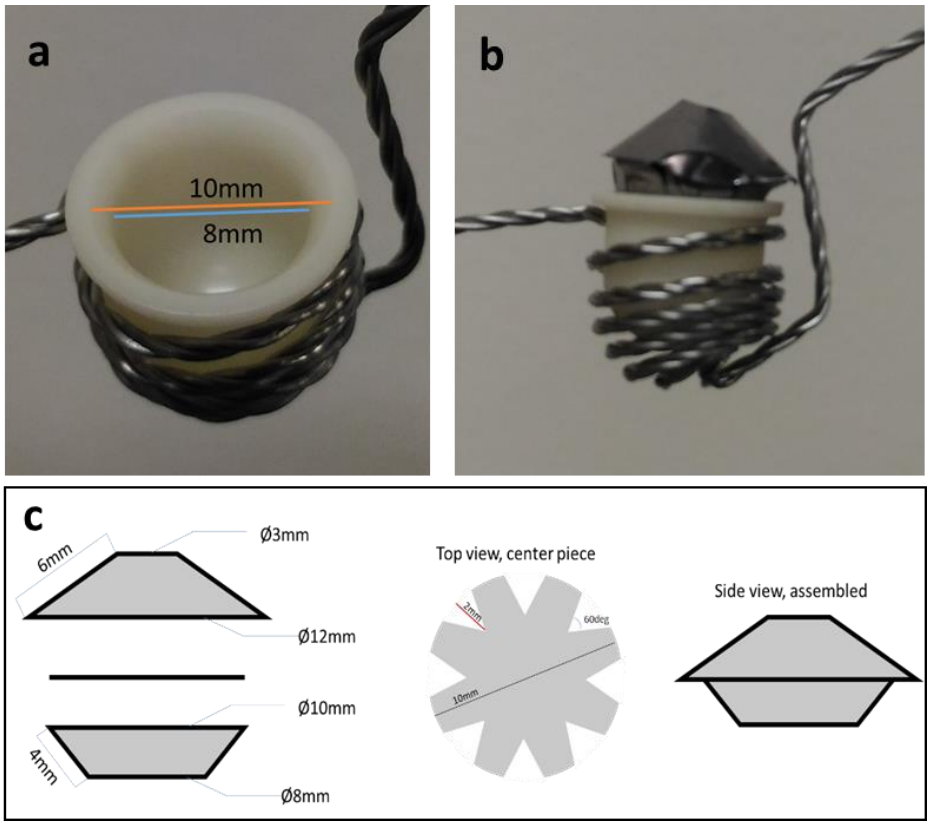

Figure 6.1: image of alumina crucible for holding the GaP and a tungsten wire for heating the crucible. b: image of the scavenger made from tantalum. c: schematic of the scavenger

6.2 Initial dosing tests:

After loading the crucible with 0.3g of GaP chips, the scavenger was installed in a system with a quadupole mass spectrometer and an XPS. It was placed in a chamber with a window so that its temperature could be monitored with an optical pyrometer. The crucible was heated to 800^{o}C for 24 hours to allow impurities to outgas. This

temperature was below the temperature that P_2 vaporized. After outgassing, the temperature was increased to 1100°C, and the mass spectrometer was used to scan for the possibility of unknown vapors and to check the P_2/P_4 ratio. The results are shown in Fig 6.2. In literature, Mondry et al [134] report P_2/P_4=120 from their decomposition source. From this test, we measured P_2/P_4=14.5. Though this is not nearly as good as reported by Mondry et al, it is far better than that achieved by red phosphorous crackers from which P_2/P_4=4.

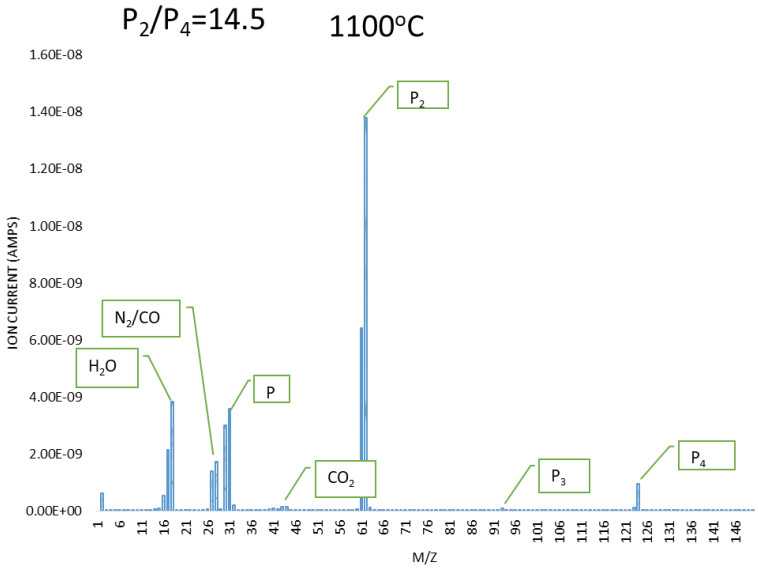

Figure 6.2 mass spec of vapors produced while using GaP decomposition source at 1100°C.

After confirming that P_2 was dosing and that no Ga was evident in the vapors, an attempt was made to dose onto a molybdenum plate. A molybdenum plate was positioned 4 inches above the P_2 doser and the filament was heated to 1100°C for 10 minutes. After dosing, the plate was transferred to the XPS without removing from vacuum. The XPS showed that phosphorous was on the plate. Comparing the intensity ratio of the P 2p peak at 130eV [140] and the Mo 3d5/2 peak at 228eV, the ratio was a

low 0.06. Curious if running the mass spectrometer during dosing would cause a problem, the experiment was repeated while the mass spec was running. This time, the P 2p peak had an obvious shoulder at 133eV which is indicative of palladium oxide. Also, the P/Mo ratio dropped to 0.03. Due to this information, the mass spectrometer was never run when dosing on a substrate. Also, as a precaution, ion gauges were turned off during dosing. There was concern that the P/Mo ratios were low as they are proportional to coverage. Another dosing attempt was made for 1 hour and the P/Mo ratio measured by XPS was only 0.1. One hypothesis for low coverage was that P might have a low sticking ratio on Mo. Another hypothesis was that the GaP needed more surface area to release the P_2. When the doser was moved to the system with the Ni single crystal, the GaP was ground to increase its surface area and 0.5g was used instead of the previous 0.3g. Also, dosing temperature was increased to 1200^{o}C. At no time was Ga or GaP (BE=134.8 [141]) observed with the XPS.

6.3 Dedicated vacuum chamber for GaP decomposition

To mitigate any potential phosphorous contamination that could be caused by dosing P_2 in a shared system, the GaP decomposition source was moved to a single chamber system with standard facilities for sample preparation and analysis: an ion gauge, a sputtering gun for cleaning by Ar ion bombardment and an OCI LEED-AUGER Spectrometer. In this chamber, the Ni(111) single crystal was mounted to a molybdenum plate attached to a liquid N_2 cooled xyzθ manipulator. The sample was heated by a filament located behind the molybdenum plate. Sample temperature was monitored using a thermocouple spot welded to the side of the single crystal. The crystal was cleaned by repeated cycles of Ar ion sputtering at 2kV for 10-20 minutes, followed by annealing at

600°C for 10 minutes. The crystal was allowed to cool below 100°C between cleaning cycles. Cleaning cycles were repeated until the Ni crystal was clean as confirmed by both a sharp (111) LEED pattern and the P_{LVV} and C_{KLL} Auger peaks being undetectable by AES. Annealing temperatures above 600°C were not used to avoid phosphorous contamination that most likely came from the sample holder/manipulator.

A difficulty arose by having both the Ni(111) crystal and the GaP decomposition source in the same chamber. It was found that as the GaP source was heated, it always had a small amount of off-gassing. This is evident by the mass spec traces shown in Fig. 6.3 that were recorded as the GaP was heated. This off-gassing polluted the clean surface of the Ni crystal. Turning off the decomposition source to clean the Ni again meant that the decomposition source would again produce the off-gas. This cycle necessitated use of a second chamber for preheating the GaP decomposition source that was separated from the main chamber by a gate valve.

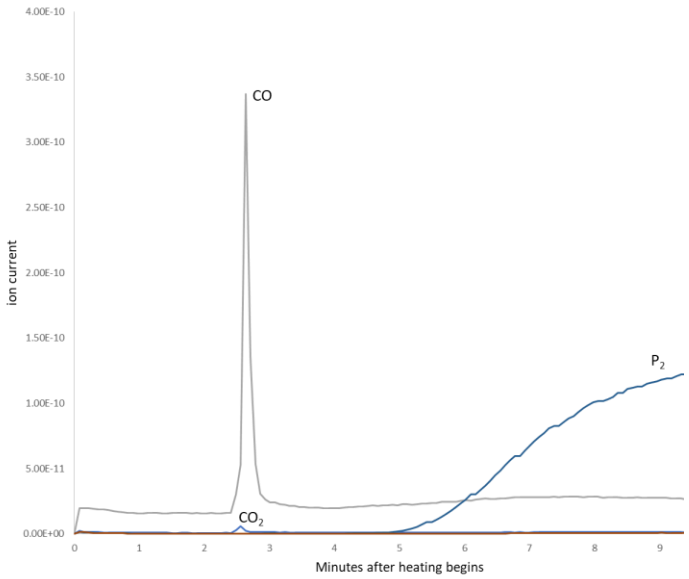

Figure 6.3 Mass spec trace while heating GaP decomposition source. Off gas of CO is observed while source is heating.

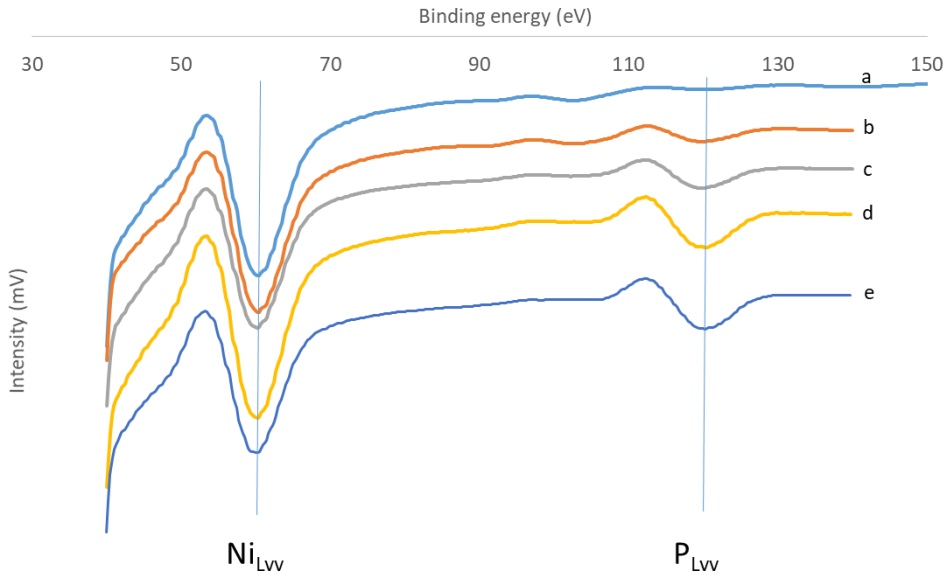

Figure 6.4 AES showing various dosing times and P_2 coverages. a: clean surface, b: short dose. Gate valve was closed as soon as it was opened. 20% coverage. c: gate valve remained open 45 seconds. 37% coverage. d: gate valve remained open 90 seconds. 44% coverage. e: gate valve remained open 3 minutes. 51% coverage

The second chamber had its own turbo pump, cold cathode gauge, quadrupole mass spectrometer and the GaP filled P_2 doser. To dose the P_2, the source was outgassed for an additional hour at 1000°C before increasing the temperature to 1200°C. This was done with the gate valve closed to maintain cleanliness of the Ni sample. During the hour of GaP outgassing, the clean Ni sample was preheated to 200°C to ensure that it had no condensed water on its surface. When the pressure of the GaP chamber increased to $1.0*10^{-5}$ Pa, the gate valve was slowly opened (30 seconds opening time) and the P_2 entered the main chamber. The gate valve would then be slowly closed immediately after it was fully open or up to 4 minutes later, according to the desired dose. The amount of P on the Ni was determined by AES using P_{Lvv} and Ni_{Lvv} peak ratios and a correlation between AES ratios and monolayer coverage found by H_2 Temperature Programmed

Desorption reported in literature[142]. As seen by the AES spectra in Fig. 6.4, the timing of the gate valve proved to be an adequate method for controlling the P_2 coverage on the nickel.

6.4 LEED image reproduction

After dosing, the Ni(111) crystal was annealed and then cooled by the addition of liquid N_2 to the manipulator. After cooling the crystal, LEED images were observed. Following literature reports to achieve the $\sqrt{7}^{x}\sqrt{7}R19$ diffraction [128], the sample was given a 30sec dose of P_2 then annealed to 500°C. As soon as the sample reached annealing temperature, the annealing was stopped. Following literature reports to achieve a "complicated pattern," [129] the sample was given a 30sec dose of P_2 then annealed to 600°C. The annealing temperature was held for 10 minutes. These images are shown in chapter 7, Fig 7.1.

6.5 Conclusion

This work demonstrated a method to adapt a GaP decomposition, originally used for MBE, for use in surface science studies by creating sub-monolayer coverages of P_2. The tantalum scavenger was sized to fit in a 1mL crucible. After observing formation of phosphate when the mass spec was on, care was taken to not use any ion-forming instrumentation during dosing. To prevent surface contamination from off-gassing, a second chamber was used to preheat the GaP before dosing. These steps in adapting the P_2 dosing method for sub-monolayer coverages lead to successful reproduction of LEED images previously observed from dosing PH_3. This opens the door for use of this method in future surface science studies.

CHAPTER 7

A NEW INTERPRETATION OF THE √7×√7 R19.1° STRUCTURE FOR P ADSORBED ON A NI(111) SURFACE[1]

7.1 Abstract

We have studied P adsorption on Ni(111), a system which shows complex adsorbate structures. We determined the phase diagram of the surface P adsorbed on Ni(111). At low coverage, amorphous P was observed. At temperatures between 373 K and 673 K and coverages above 0.1 monolayer, we found a √7×√7 R19.1° structure, but above 673 K, other complex structures were created. These structures seemed to correlate with each other and we reinterpret a √7×√7 R19.1°structure of P adsorbed on Ni(111) based on the similarities of these surface structures. The new rectangular structure for the √7×√7 R19.1° is discussed in relation to the Ni_2P local structure.

7.2 Introduction

Adsorption structures and surface reconstructions are classic topics studied in surface science [143]. The adsorption structures of S and Cl, for example, on Ni(111) have been well studied with various techniques. The adsorption of Cl on Ni(111) gives a √3×√3 R30° pattern where Cl is adsorbed at a hollow site with no Ni below in the second layer (which is called as "the fcc hollow site"), and the Ni-Cl distance is 0.233 nm [144]–[147]. When S is adsorbed on Ni(111) at room temperature or below, p(2x2) and √3×√3

[1] Elizabeth Barrow, Grant S. Seuser, Hiroko Ariga-Miwa, Donna A. Chen, Jochen Lauterbach, and Kiyotaka Asakura. Accepted by Science and Technology of Advanced Materials. Reprinted here with permission of publisher

R30° overlayer structures were observed [148]–[154]. Complex low energy electron diffraction (LEED) patterns, such as $5\sqrt{3} \times 2$, were produced when the S/Ni(111) surface was heated [149], [155]–[164].

In contrast to the adsorption of Cl and S on Ni(111), the adsorption structure of P on Ni(111) has rarely been reported, probably due to the observed amorphous or complex structures. When P is adsorbed on Ni(111) at room temperature, an increasing coverage causes the Ni (1x1) LEED pattern to gradually diminish without the formation of a distinct structured overlayer[129]. Two previous studies of P/Ni(111) reported clear LEED patterns after annealing the P/Ni(111). A Ni(111) $\sqrt{7}\times\sqrt{7}$ R19.1°-P (denoted as $\sqrt{7}\times\sqrt{7}$ R19.1° P/Ni(111)) LEED pattern was obtained when the 3/7 monolayer (ML) P-covered surface was annealed to 773 K with the heating stopped as soon as 773 K was reached [128]. A more complex LEED pattern was reported by annealing a 0.15 ML P/Ni(111) to 873 K and maintaining that temperature for 5 minutes [129]. These reconstructed structures were very complicated, and further studies of these structures have not been reported in the literature as far as the authors know.

Recently, Ni_2P, an intermetallic compound, has drawn wide interest due to its high catalytic activity. Its crystal structure belongs to the $P\bar{6}2m$ space group with a=b=5.859 Å and c=3.382 Å [165]. The Ni_2P is widely used for hydrodesulfurization[166] and hydrodenitrogenation [166]–[168] for fossil fuels, hydrodeoxygenation [169]–[172] for biomass conversion, and as a cathode catalyst in hydrogen evolution reactions [173], [174]. The Ni_2P can be regarded as a substitutional material for noble metals, such as Pt and Pd. Operando X-ray absorption fine structure (XAFS) studies have revealed the reaction mechanism of hydrodesulfurization, but the

structure-activity relationship is not yet clear [175]–[178]. Surface science studies on a well-defined surface may provide more details about the structures and their relationships with catalytic activity. Several studies have been reported for Ni_2P single crystal surfaces [156], [179]–[189]. X-ray photoelectron spectroscopy (XPS), scanning tunneling microscopy (STM), angle resolved photoelectron spectroscopy (ARUPS), LEED and thermal desorption spectroscopy (TDS) have all been applied to $Ni_2P(0001)$ and $Ni_2P(10\bar{1}0)$ surfaces. The surface structures of Ni_2P single crystals were complicated even for a (1 × 1) structure, and more complicated surfaces were observed after annealing treatments [187], [190]. We have reported that P enrichment occurred to remove the Ni dangling bonds [183], [191]. Control of the P concentration on the surface, however, is difficult because P atoms are always supplied from the bulk[192]. In order to better understand the Ni_2P catalysts, we carried out experiments on Ni(111)-P surfaces where the P was supplied by dosing from the gas-phase. Since the P supply was limited to surface deposition, P migration from the bulk could be neglected. In this work, we studied the structures of P adsorbed on Ni(111). Previously, the $\sqrt{7}\times\sqrt{7}$ R19.1° structure and the more complicated structure (called pattern C in this paper) were reported independently, though the two structures showed similarities. We synthesized the two structures and obtained a comprehensive phase diagram. We also reported a new, complicated LEED pattern (called pattern B), which was previously not reported. In order to interpret these three structures consistently, we propose the rectangular surface unit cell and a new model structure for $\sqrt{7}\times\sqrt{7}$ R19.1°.

7.3 Experimental Details

The experiment was carried out in two ultrahigh vacuum (UHV) chambers (about 5×10^{-8} Pa) composed of a main chamber and a P-evaporation chamber, which were separated by a gate valve. In the main chamber, the Ni(111) single crystal was attached to a molybdenum plate and mounted on an xyzθ manipulator. The manipulator was equipped with a resistive heater and cooled with liquid N_2. The temperature was monitored using a thermocouple spot-welded to the side of the Ni single crystal. The Ni(111) was cleaned in the main chamber by repeated cycles of Ar ion sputtering at 2kV for 10-20 minutes, followed by annealing at 873 K for 10 minutes. Cleanliness of the surface was confirmed by both a sharp (1×1) LEED pattern and by the absence of detectible P_{LVV} and C_{KLL} peaks by Auger electron spectroscopy (AES). The evaporation chamber was equipped with an evaporation source [134]–[136]. The evaporation chamber and the main chamber were separated by a gate valve during the GaP preheating to remove the surface impurity just before the evaporation. After preheating the GaP, the gate valve was opened to introduce P into the main chamber. The P adsorption was carried out in the main chamber. The Ni(111) sample was heated at 373 K during the P evaporation. The amount of P on the Ni was determined by AES using P_{LVV} and Ni_{LVV} peak ratios. Based on hydrogen thermal desorption studies of P/Ni(111) [142], a P_{LVV}/Ni_{LVV} ratio of 0.5 corresponds to a P coverage of 0.33 ML.

7.4 Results

The (1×1) LEED spots of the Ni(111) substrate gradually became faint with the deposition of P and completely disappeared at the P saturation coverage. Approximately 0.24 ML of P was deposited, and the surface was annealed to chosen temperatures (573 K

– 873 K); three types of LEED patterns designated as pattern A, pattern B, and pattern C were observed, as shown in Figure 7.1.

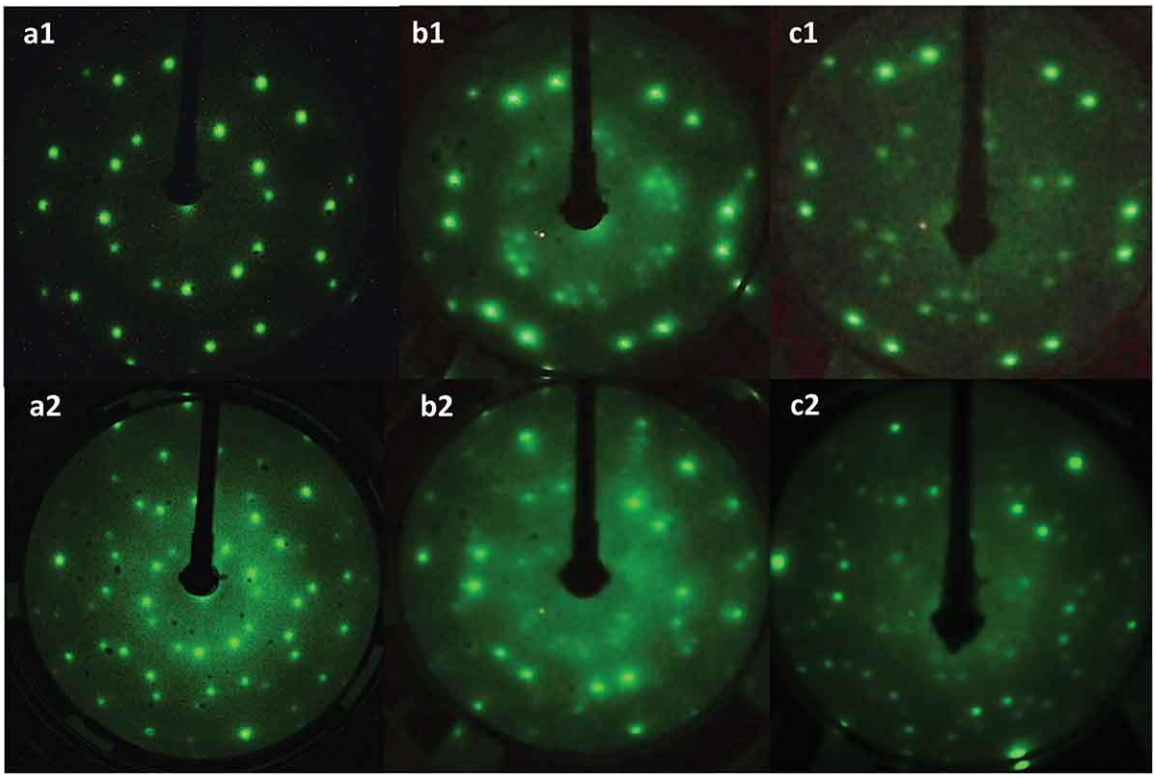

Figure 7.1 Photographs of LEED images of post annealed surfaces of P dosed onto the Ni(111) surface. a1, a2: pattern A which was formed after 0.26 ML P was deposited on Ni(111) heated at 373 K. b1, b2: images of a series of patterns referred to as pattern B(coverage was 0.15 ML and annealing temperature was 873 K for less than 30 s) c1, c2: pattern C (coverage was 0.12 ML and annealing temperature was 873 K for 10 minutes). Acceleration energies were 40 eV for a1 and b1, 32 eV for c1, respectively. Acceleration energies for a2, b2 and c2 were 80, 75 and 70 eV, respectively.

We deposited 0.26 ML P on Ni(111) at 373 K, we obtained Pattern A. Pattern A was consistent with a √7×√7 R19.1° diffraction pattern, which had previously been reported on Ni(111) [128]. Fig. 7.2 shows a √7×√7 R19.1° structure drawn in LEEDPat4.2 [193] with its commonly used reciprocal lattice unit vectors. $\overrightarrow{a_1}$ and $\overrightarrow{a_2}$ were the Ni(111) surface lattice unit vectors while $\overrightarrow{b_1}$ and $\overrightarrow{b_2}$ were the overlayer lattice

unit vectors. The structure was composed of two domains, which had a mirror symmetry relation with each other as shown in Figure 7.2. The 12 spots appeared around (0,0).

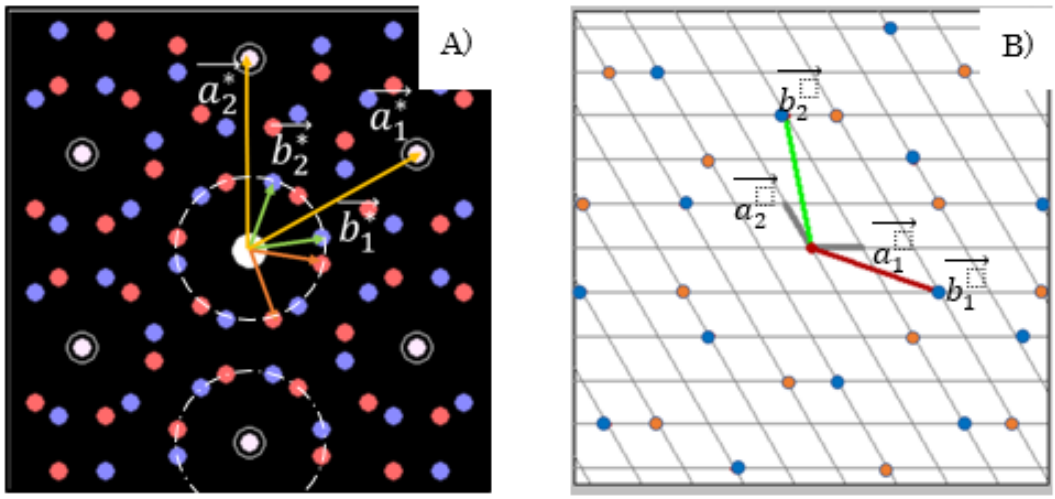

Figure 7.2 A) √7×√7 R19.1° LEED pattern with the reciprocal lattice unit vectors. Red and blue short vectors indicate different domains. Dashed and dot-dashed circles indicate the inner circle around (0,0) and the one around (0, -1), respectively. B) the real space substrate lattice and its lattice unit vectors $(\vec{a}_1, \vec{a}_2)$. *Blue and red points indicated the lattice associated with √7×√7 R19.1° for two different domains, respectively.* $\vec{b}_1$ *and* $\vec{b}_2$ *were overlayer lattice unit vectors.*

Figure 7.1(b) shows LEED pattern B after annealing at 873 K for 30 sec. Pattern B had LEED spots that corresponded well with those of √7×√7 R19.1° especially around (n,m) (n or m=1,-1). The spots around (0,0) (on the dashed line in Figure 7.2 (B)) were split into three spots compared to pattern A, indicating that pattern B had a unit cell incommensurate to the substrate unit cell. These groups of three spots around (0,0) were always weak and diffuse. Consequently, 12 sets of three split spots appeared around (0,0). We believe that pattern B corresponds to a newly reported structure.

At higher temperatures that ranged from 773 K and 873 K, pattern C appeared where 6 sets of 5 spots were found in the inner circle. The √7×√7 R19.1°-like spots were stronger around (n,m) (n or m=1,-1). This pattern C corresponds to the one observed

previously on P on Ni(111) prepared by PH_3 deposition [129]. Note that the coverage decreased with temperature. When the initial coverage of P was 0.24 ML, 873 K annealing produced pattern C and reduced the P coverage to 0.12 ML, probably due to the diffusion into bulk Ni or evaporation from the surface.

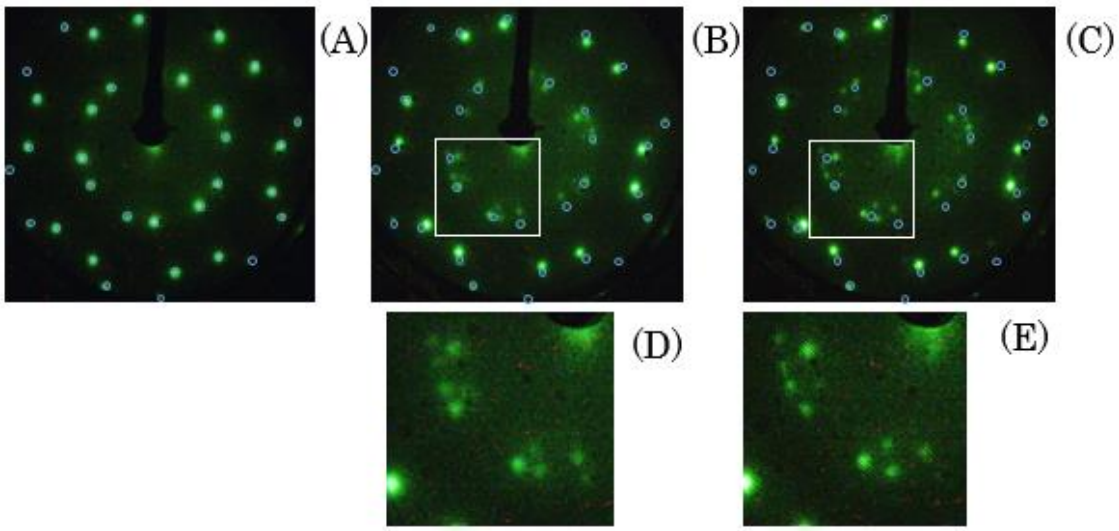

Figure 7.3 LEED patterns for P/Ni (111) (initial coverage was 0.24 ML) (A): Annealed at 573 K for 10 minutes, Pattern A appeared; (B) After sequential annealing at 773 K for 10 minutes, we obtained pattern B; (C) After further annealing at 773 K for 10 minutes, the LEED corresponding to pattern B appeared but spots changed compared to the previous one (Figure 3 (B)). (D) and (E) are expanded images of (B) and (C), respectively. The separation of the three split spots became larger in (C) and (E). The small blue circles in (A), (B), and (C) indicated the √7×√7 R19.1° spot positions.

In order to see the relation between these patterns, we carried out subsequent heating. Figure 7.3(A) shows the √7×√7 R19.1° after 573 K annealing. When the sample was heated to 773 K, pattern B was observed, as shown in Figure 7.3(B). Figure 7.3(B) has blue open circles which serve as a visual guide and correspond to the √7×√7 R19.1° spots seen in Figure 7.3(A). These spots were slightly shifted in the direction of the substrate reciprocal lattice unit vector, as shown in Figure 7.3(B). In addition, their positions were varied with the annealing temperature and duration time as shown in

Figure 7.3(C) where the sample was heated at 773 K for another 10 minutes. The difference between Figure 7.3 (B) and Figure 7.3(C) was that the location of the three split spots changed. The three split spots were expanded, and two sets of the neighboring three split spots moved closer to each other with increased annealing time. Pattern B appeared to be a transient structure. Further expansion of the three split spots transformed the two sets of three split spots into one set of 5 spots observed in pattern C. These similarities and continuous changes indicated that the unit cells of pattern A, pattern B and pattern C were closely related.

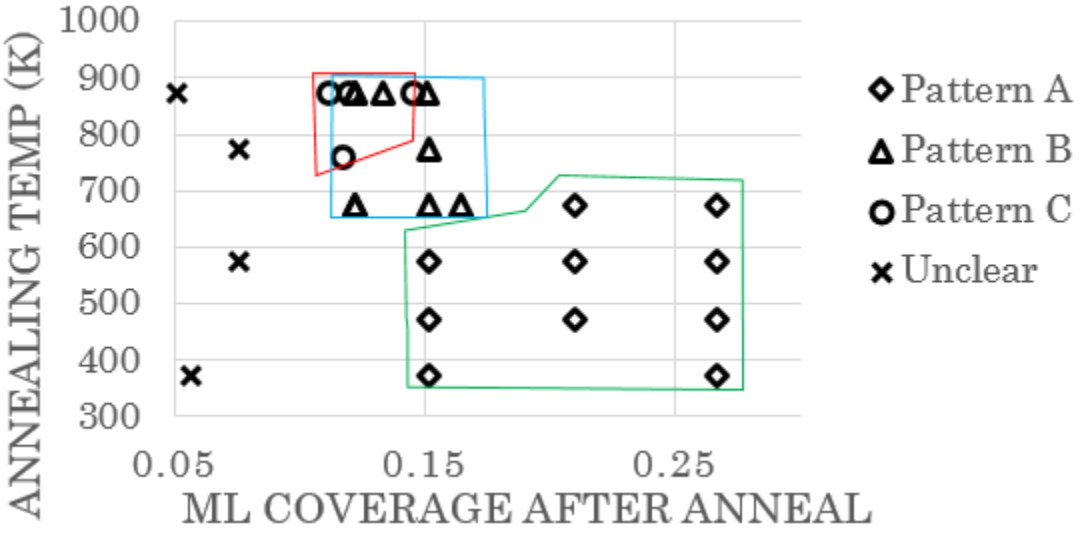

Figure 7.4 Phase diagram showing conditions for the 3 observed patterns. P coverages below 0.08 ML did not produce clear LEED patterns after annealing. Coverages were determined by AES after LEED imaging was complete.

Figure 7.4 shows the phase diagram of P on Ni(111). Here, each sample was annealed at the designated temperatures. The coverages reported were measured by AES after the annealing and LEED measurements. For coverages less than 0.08 ML, we could not detect a LEED pattern since the surface remained amorphous. For coverages greater than 0.11 ML, the $\sqrt{7}\times\sqrt{7}$ R19.1° structure started to appear above 373 K. If the sample

was heated above 673 K, we observed pattern B where the √7×√7 R19.1° spots were split into three. Pattern B is a transient structure, and the spot positions gradually changed with further annealing. Finally, when the sample was annealed above 773 K-873 K, pattern C was observed. Since pattern B was a transient state from pattern A to pattern C, we had overlapping areas of pattern B and pattern C where both pattern formations were highly dependent on the dosing amount, annealing temperature, and annealing time.

7.5 Discussion

The √7×√7 R19.1° overlayer lattice unit vector $\overrightarrow{b_1}$ and $\overrightarrow{b_2}$ were expressed by the substrate vectors, $\overrightarrow{a_1}$ and $\overrightarrow{a_2}$ as

$$\overrightarrow{b_1} = 2\,\vec{a}_1 - \vec{a}_2$$

$$\overrightarrow{b_2} = \vec{a}_1 + 3\vec{a}_2$$

Or

$$\begin{pmatrix}\vec{b}_1\\ \vec{b}_2\end{pmatrix} = \begin{pmatrix}2 & -1\\ 1 & 3\end{pmatrix}\begin{pmatrix}\vec{a}_1\\ \vec{a}_2\end{pmatrix}$$

This can be graphically shown as in Fig. 7.2. The reciprocal lattice vector was written as

$$\begin{pmatrix}\overrightarrow{b_1^*}\\ \overrightarrow{b_2^*}\end{pmatrix} = \frac{1}{7}\begin{pmatrix}3 & -1\\ 1 & 2\end{pmatrix}\begin{pmatrix}\overrightarrow{a_1^*}\\ \overrightarrow{a_2^*}\end{pmatrix}$$

Saidy et al. produced a hexagonal unit cell to explain the √7×√7 R19.1° structure [128]. In their model structure, 3 Ni atoms were replaced with 3 P atoms. The maximum coverage of P was thus 0.57 ML. However, this hexagonal unit cell could not explain the three split spots in pattern B. To observe the three split spots, the breakdown of 3 fold rotational symmetry is necessary. We could reproduce the three split spots in the inner circle around (0,0) if the angle between the overlayer lattice unit vectors $\overrightarrow{b_1}$ and $\overrightarrow{b_2}$ was set to 130° and the angle between the overlayer lattice unit vector and the substrate ($\overrightarrow{b_2}$ and $\overrightarrow{a_2}$) was set to -9.1° instead of -19.1°. As in pattern C, 6 sets of five spots could be

seen by the rotation of the overlayer by 9.1° where the angle between $\overrightarrow{b_2}$ and $\overrightarrow{a_2}$ became 0°. This lattice unit vector allowed us to create the incommensurate surface structure by breaking down the three-fold rotational symmetry. Unfortunately, this approach also had a fatal problem in that there was no agreement between the calculated and observed spots around (m, n) (m or n=-1,1). This lack of model agreement occurred because the spots on the inner circle around the (0,0) spot were used for the reciprocal lattice unit vectors. It is not necessary to select the spots around (0,0) as the reciprocal lattice unit vectors because electron diffraction suffers strongly from multiple scattering [194]. Since the spots around (m, n) (m or n = -1, 1) appeared stronger in pattern B and pattern C, these spots could be regarded as the reciprocal lattice unit vectors. The spots around (0,0) appeared as a result of multiple scattering. Based on this idea we reinterpreted the √7×√7 R19.1° pattern.

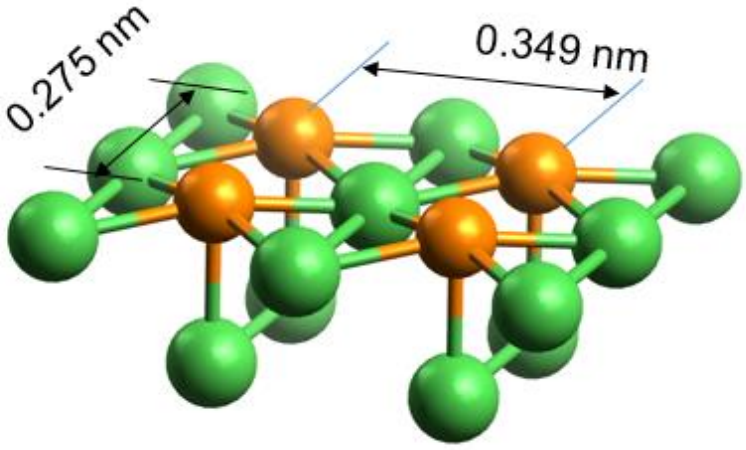

Figure 7.5 Model structure proposed for pattern C. [25]
Green spheres are Ni and the orange spheres are P.

We previously proposed the structure for pattern C as shown in Fig. 7.5 based on extended X-ray absorption fine structure (EXAFS) analysis [129], where the topmost two layers of Ni were reconstructed to a rectangular unit cell. The P was adsorbed above the

center of the rectangular unit. If we reproduced the √7×√7 R19.1° based on this rectangular model, we could connect pattern A (√7×√7 R19.1°) and pattern C. After trial and error, we found the rectangular unit cell could indeed be well fit to the hexagonal √7×√7 R19.1° First we selected the surface reciprocal lattice vectors from the spots on the circle around (m,n)(m or n=-1, 1) shown as $\vec{c}_1$ and $\vec{c}_2$ in Figure 7.6(A).

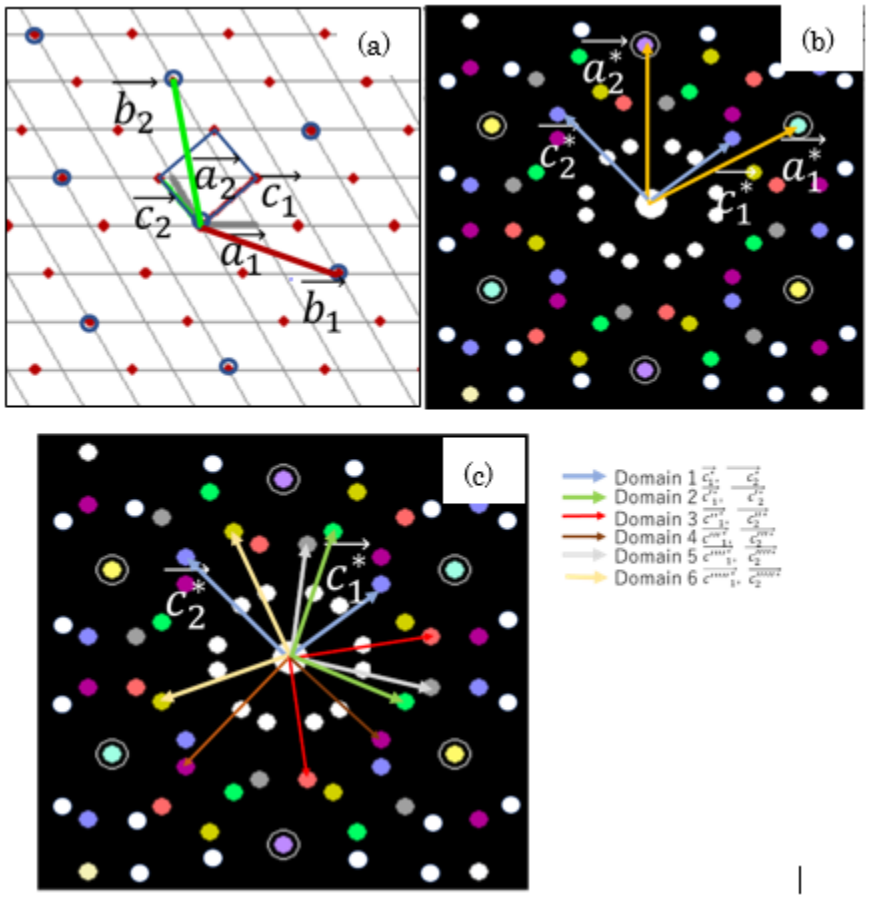

Figure 7.6 (a) The rectangular overlayer lattice points (red) with lattice vectors ($\overrightarrow{c_1}$, $\overrightarrow{c_2}$). The blue circles are the lattice points of the √7×√7 R19.1° structure with lattice vectors ($\overrightarrow{b_1}$, $\overrightarrow{b_2}$). (b) reciprocal space of (a). The white spots indicate multiple scattering. (c) Lattice unit vectors 6 domains.

The relationship between $(\vec{c}_1, \vec{c}_2)$ and ($\vec{a}_1$, $\vec{a}_2$) was

$$\begin{pmatrix} \vec{c}_1 \\ \vec{c}_2 \end{pmatrix} = \begin{pmatrix} 1.5 & 1 \\ -0.25 & 1 \end{pmatrix} \begin{pmatrix} \vec{a}_1 \\ \vec{a}_2 \end{pmatrix}$$

$$|\vec{c}_1| = \frac{\sqrt{7}}{2}|\vec{a}_1|\,, |\vec{c}_2| = \frac{\sqrt{21}}{4}\,|\vec{a}_1|$$

$$\vec{c}_1 \cdot \vec{c}_2 = 0$$

$$\begin{pmatrix} C_1^* \\ C_2^* \end{pmatrix} = \begin{pmatrix} 4/7 & 1/7 \\ -4/7 & 6/7 \end{pmatrix} \begin{pmatrix} a_1^* \\ a_2^* \end{pmatrix}$$

The $(\vec{b}_1, \vec{b}_2)$ required for the $\sqrt{7} \times \sqrt{7}\, R19.1°$ structure were the unit cell vectors for which both the $(\vec{c}_1, \vec{c}_2)$ and $(\vec{a}_1, \vec{a}_2)$ lattices were commensurate as shown in

$$\begin{pmatrix} \vec{b}_1 \\ \vec{b}_2 \end{pmatrix} = \begin{pmatrix} 1 & -2 \\ 1 & 2 \end{pmatrix} \begin{pmatrix} \vec{c}_1 \\ \vec{c}_2 \end{pmatrix} = \begin{pmatrix} 2 & -1 \\ 1 & 3 \end{pmatrix} \begin{pmatrix} \vec{a}_1 \\ \vec{a}_2 \end{pmatrix}$$

The spots around the (0, 0) appeared as the result of multiple scattering events in the overlayer and the substrate lattices that reproduced the LEED patterns as shown in Figure 7.6(b). For example, $\overrightarrow{b_1^*}$ is created by $-\overrightarrow{c_1^*} + \overrightarrow{a_1^*}$ in Figure 6(B). Note that the multiple scattering spots of the other domains appeared at the same position. For example, the multiple scattering spots of $(\overrightarrow{c_1^{*\prime}} - \overrightarrow{c_2^{*\prime}}) + \overrightarrow{a^*}_2$ in the second domain（Domain 2 of Figure 7.6(C)）and of $2(\vec{c}_2^{*\prime\prime} - \overrightarrow{c_1^{*\prime\prime}}) - (\overrightarrow{a_1^*} + \overrightarrow{a^*}_2)$ in the third domain (Domain 3 of Figure 7.6(C)) gave the same spot. In other words, the spots around the (0,0) were triply degenerated spots. This meant when the rectangular unit vectors were slightly deformed, these spots were split into 3 spots, corresponding to pattern B.

Thus, the rectangular unit cell and multiple scattering events can rationally explain the √7×√7 R19.1° structure and its continuous transition to patterns B and C. Moreover, the strong spots in pattern B and pattern C are understood by the reciprocal lattice unit vector, although further calculations are necessary to completely reproduce all of the spots in pattern B and pattern C.

In the literature, the √7×√7 R19.1°is usually interpreted in terms of a hexagonal overlayer. In the LEED analysis of √7×√7 R19.1° of P/Ni(111), 4 surface Ni atoms out of 7 were replaced with 4 P atoms to produce the mixed overlayer of Ni and P [128]. The √7×√7 R19.1° overlayer for S adsorbed on Cu(111) [195], [196], Rh(111) [197]–[199] and Pd(111) [200], [201] had similar structures, maintaining the hexagonal unit cell. The rectangular lattice structure we propose is unique and explains the relationship between the √7×√7 R19.1° structure and the two incommensurate structures of pattern B and pattern C. In the literature we found one other example of the formation of an overlayer with a different lattice system. This example was the $5\sqrt{3}\times 2$ pattern on Ni(111), where the surface overlayer had a square lattice [202]. S was adsorbed on the square-reconstructed Ni surface to increase the number of S-Ni bonds.

Hereinafter we continue to discuss the possible local structure around P based on the rectangular reconstruction. We have proposed a rectangular unit cell for pattern C, as shown in Figure 7.5, which has dimensions 0.275 nm ×0.349 nm. P adsorbs on the center of the reconstructed Ni rectangular unit. If a similar unit cell is formed in pattern A, or √7×√7 R19.1°, the rectangular structure has size 0.284 nm × 0.329 nm. In this model structure the maximum coverage of P should be 4/7 ML. This structure can be related to the local structure found in the $(11\bar{2}0)$ surface of the Ni_2P crystal which has a rectangular 0.261 nm × 0. 338 nm lattice. Each corner of this rectangular local structure has Ni atoms, as shown in Figure 7.7. P is situated at the Ni 4-fold hollow site. Therefore the rectangular unit of the √7×√7 R19.1° structure has a similar local structure to Ni_2P.

Further reconstructions to pattern B and C might occur to produce more stable structures. Pattern B might be the transient structure from the √7×√7 R19.1° structure to

the structure of pattern C. In order to measure the actual unit cell dimension and to confirm the definite conclusions, we need further calculations and experiments on the √7×√7 R19.1° structure of P/Ni(111) using atomic scale STM and EXAFS.

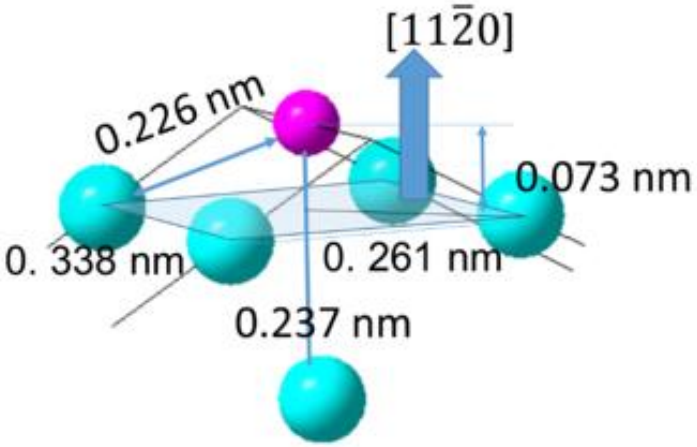

Figure 7.7 Part of the crystal structure unit of Ni_2P. The large blue and small purple sphere represent Ni and P atoms, respectively. The blue rhombus corresponds to the (11$\bar{2}$0) plane.

7.6 Conclusions

We have found that overlayer structures formed during the adsorption of P on Ni(111) depends on the coverage, the annealing temperature and time. When the sample is heated between 373 K and 673 K, the √7×√7 R19.1° reconstructed structure is created. Annealing at temperatures above 673 K leads to the formation of pattern B, where the spots in the √7×√7 R19.1° pattern are split into three spots. The degree of separation and position of the three spots continue to change with temperature and annealing time. At higher temperatures, pattern C is produced where every two of the twelve sets of the three split spots in pattern B merge to give a pattern with six sets of five spots each. We have proposed a new interpretation of the √7×√7 R19.1° structure based on a rectangular unit

cell, which can explain the successive changes to pattern B and pattern C. The rectangular unit is similar to the local structure of P on the $Ni_2P(11\bar{2}0)$ plane, and it can be regarded as the model structure for the Ni_2P surface.

7.7 Acknowledgements

The authors express their gratitude to the South Carolina Smart State Center of Economic Excellence for Strategic Approaches to the Generation of Electricity (SAGE), and the National Science Foundation grant DGE 1250052.

This collaboration was carried out under the friendship contract between ICAT Hokkaido University and the Department of Chemical Engineering, University of South Carolina. The work is supported by the CREST-JST project “Innovative Catalyst”. The GaP evaporator was constructed by ICAT technical division. We used an open software LEEDPat4.2 provided by the Fritz-Haber-Institute, Berlin (http://www.fhi-berlin.mpg.de/KHsoftware/LEEDpat/). The evaporation systems were constructed by the technical support team of Institute for Catalysis, Hokkaido University.

CHAPTER 8

CONCLUSIONS AND FUTURE WORK

This work contained multiple projects all in some way connected to the hydrodeoxygenation of biomass derived chemicals. Though conclusions have been drawn, each work has the potential to be continued

The work in chapter 4 focused on the utilization of the chemical 2-methyl furan for fuels. A bifunctional catalyst Pt/Al-MCM-41 was developed for the single step alkylation and hydrodeoxygenation of 2MF and butanal to diesel with 96% yield without the need for solvent. The catalyst was shown to be stable over 4 runs of 20 hrs each. This work was continued with a study of the oligomerization of 2MF over solid catalysts. An aluminosilicate catalyst with Si/Al=20 was developed that demonstrated 40% conversion of 2MF in a pressurized batch reactor. This produced a mix of carbohydrates with the major components being the 2MF trimer and tetramer. Both the tetramer and the trimer are known to perform well under hydrodeoxygenation to form C15 and C20 hydrocarbons. Until this work, it was believed that the formation of the 2MF trimer required water for ring opening, but it was formed here without water.

A next step for this project is to develop a bifunctional catalyst for both the oligomerization of 2MF and its hydrodeoxygenation. Much of the preliminary work has been done for this with the development of an aluminosilicate that can be used in a pressurized batch reactor to form predominantly the trimer without many large oligomers.

Though it is contrary to one of the original goals of this project, it is likely that a solvent would be beneficial as initial attempts to use 2MF in a fixed bed reactor resulted in clogs. Successfully oligomerizing and hydrodeoxygenating 2MF in a single step would form a diesel mix with longer chains than in the 2MF+butanal project.

In Chapter 5, the structure of ReO_x/CeO_2 was studied. Though the ReO_x surface structure has been well characterized on SiO_2, Al_2O_3, ZrO_2 and TiO_2 supports, the ReO_x surface structure on CeO_2 had not been rigorously studied. It has been discovered that the structure of ReO_x supported on CeO_2 is unlike any previously studied supported ReO_x. One of the main differences is that ReO_x is chemisorbed on the surface of CeO_2 in ambient conditions instead of being hydrolyzed by surface water. Additionally, instead of vaporizing as is commonly reported, it is shown that with high loadings of ReO_x, crystalline Re_2O_7 is formed and remains on the surface even after calcination at 500^{o}C. It is shown that with the lowest loadings studied, 0.5wt%Re, Re has a +VII oxidation state, and ReO_x is present with both tetrahedral and octahedral coordination. Using an $^{18}O_2$ isotope exchange, it is shown that the tetrahedrally coordinated portion of ReO_x/CeO_2 has a single terminal oxygen. Upon reduction with H_2, the octahedrally coordinated portion of ReO_x reduces at a lower temperature than the tetrahedrally coordinated portion.

Now that the FTIR and Raman peaks of ReO_x/CeO_2 have been assigned, these techniques can be used to determine the mechanism of simultaneous hydrodeoxygenation on ReO_x-Pd/CeO_2. Using a low concentration of reactant, so that water formation does not decrease signal, the reaction can be run in the reaction cells. While observing vibrational peaks in Raman and FTIR, reaction products can be observed *in operando* with a mass spec. It was previously reported [90] that conversion decreases if the catalyst

is pre-reduced. The FTIR and Raman can elucidate what causes the decrease in reactivity by comparing *in situ* results from a fresh catalyst with those of a pre-reduced catalyst.

In chapter 7, a surface science study using LEED interpretation of phosphorous dosed on a Ni(111) single crystal was discussed. A phase diagram of the surface P adsorbed on Ni(111) was developed showing distinct overlayer structures based on loading and annealing temperature. At low coverage, amorphous P was observed. At annealing temperatures below 400°C and coverages above 0.1 ML, a $\sqrt{7}x\sqrt{7}R19.1$ structure was observed. Above 400°C, another complex structure was created. These structures seemed to correlate with each other and the $\sqrt{7}x\sqrt{7}R19.1$ structure of P adsorbed on Ni(111) was therefore reinterpreted to have a rectangular unit cell. The new rectangular structure has size 0.284 nm × 0.329 nm. This structure can be related to the local structure found in the $(11\bar{2}0)$ surface of the Ni_2P crystal which has a rectangular 0.261 nm × 0. 338 nm lattice.

This $\sqrt{7}x\sqrt{7}R19.1$ structure of P adsorbed on Ni(111) might soon be able to be used to assist in the study of Ni_2P, a catalyst used for hydrodeoxygenation. A few more preliminary comparisons should be run including TPR on P/Ni(111) to see if it is comparable to Ni_2P. Also, the structural determination provided here needs to be confirmed by STM and EXAFS.

Each of these projects have helped to further the scientific knowledge related to the heterogeneous catalysts used for hydrodeoxygenation. Above are just a few suggestions for how this work can be continued.

REFERENCES

[1] A. Wilkinson and A. McNaught, Eds., *Compendium of Chemical Terminology - The Gold Book*, 2nd ed. Blackwell Science, 1997.

[2] G. Rothenberg, *Catalysis: Concepts and Green Applications*. Wiley, 2008.

[3] R. Masel, *Principles of adsorption and reaction on solid surfaces*. New York, USA: Wiley, 1996.

[4] P. Forzatti and L. Lietti, "Catalyst deactivation," *Catal. Today*, vol. 52, no. 2–3, pp. 165–181, 1999.

[5] "Fritz Haber - Biographical." [Online]. Available: nobelprize.org.

[6] "Carl Bosch - Biographical." [Online]. Available: nobelprize.org.

[7] "Irving Langmuir - Biographical."

[8] "Gerhard Ertl - Biographical." [Online]. Available: nobelprize.org.

[9] R. Fortier, "U.S. Net Petroleum Imports Plunging Toward Zero," *Forbes*, 2018. [Online]. Available: https://www.forbes.com/sites/rrapier/2018/03/21/u-s-net-petroleum-imports-plunging-toward-zero/#3d9042dd27ba.

[10] "Oil: Crude and Petroleum Products Explained." [Online]. Available: https://www.eia.gov/energyexplained/index.php?page=oil_home#tab3.

[11] N. Greene, F. E. Celik, B. E. Dale, M. Jackson, K. Jayawardhana, H. Jin, E. D. Larson, M. S. Laser, L. R. Lynd, D. MacKenzie, J. Mark, J. McBride, S. McLaughlin, and D. Saccardi, "Growing Energy: How Biofuels Can Help End America's Oil Dependence," 2004.

[12] T. Searchinger, R. Heimlich, R. a Houghton, F. Dong, A. Elobeid, J. Fabiosa, S. Tokgoz, D. Hayes, and T.-H. Yu, "Use of U.S. croplands for biofuels increases greenhouse gases through emissions from land-use change.," *Science*, vol. 319, no. 5867, pp. 1238–1240, 2008.

[13] U. S. D. of Energy, "U. S. Billion-Ton Update," 2011, no. August.

[14] C. Raphael, *There Is No Energy Problem*. Bloomington, IN: Authorhouse, 2011.

[15] D. M. Alonso, S. G. Wettstein, and J. a. Dumesic, "Bimetallic catalysts for upgrading of biomass to fuels and chemicals," *Chem. Soc. Rev.*, vol. 41, no. 24, 2012.

[16] A. M. R. Galletti, "Biomass pre-treatment: separation of cellulose, hemicellulose, and lignin. Existing technologies and perspectives," 2011.

[17] C. Schädel, A. Blöchl, A. Richter, and G. Hoch, "Quantification and monosaccharide composition of hemicelluloses from different plant functional types," *Plant Physiol. Biochem.*, vol. 48, no. 1, pp. 1–8, 2010.

[18] A. G. Olabi, "Developments in sustainable energy and environmental protection," *Energy*, vol. 39, no. 1. pp. 2–5, 2012.

[19] D. Mohan, C. U. Pittman, and P. H. Steele, "Pyrolysis of Wood/Biomass for Bio-oil: A Critical Review," *Energy & Fuels*, vol. 20, no. 3, pp. 848–889, 2006.

[20] P. McKendry, "Energy production from biomass (part 1): Overview of biomass,"

Bioresour. Technol., vol. 83, no. 1, pp. 37–46, 2002.
[21] H. Olcay, A. V. Subrahmanyam, R. Xing, J. Lajoie, J. a. Dumesic, and G. W. Huber, "Production of renewable petroleum refinery diesel and jet fuel feedstocks from hemicellulose sugar streams," *Energy Environ. Sci.*, vol. 6, p. 205, 2013.
[22] R. Hashaikeh, Z. Fang, I. S. Butler, J. Hawari, and J. a. Kozinski, "Hydrothermal dissolution of willow in hot compressed water as a model for biomass conversion," *Fuel*, vol. 86, no. 10–11, pp. 1614–1622, 2007.
[23] M. S. Luchansky and J. Monks, "Supply and demand elasticities in the U.S. ethanol fuel market," *Energy Econ.*, vol. 31, no. 3, pp. 403–410, 2009.
[24] J. H. Lora and W. G. Glasser, "Recent industrial applications of lignin: A sustainable alternative to nonrenewable materials," *J. Polym. Environ.*, vol. 10, no. 1–2, pp. 39–48, 2002.
[25] G. Goma, *Advances in Biochemical Engineering*, vol. 61, no. 4. 1979.
[26] J. Lessard, J. F. Morin, J. F. Wehrung, D. Magnin, and E. Chornet, "High yield conversion of residual pentoses into furfural via zeolite catalysis and catalytic hydrogenation of furfural to 2-methylfuran," *Top. Catal.*, vol. 53, no. 15–18, pp. 1231–1234, 2010.
[27] H. Olcay, A. V. Subrahmanyam, R. Xing, J. Lajoie, J. a. Dumesic, and G. W. Huber, "Production of renewable petroleum refinery diesel and jet fuel feedstocks from hemicellulose sugar streams," *Energy Environ. Sci.*, vol. 6, no. 1, p. 205, 2013.
[28] F. L. Dryer, "Chemical kinetic and combustion characteristics of transportation fuels," *Proc. Combust. Inst.*, vol. 35, no. 1, pp. 117–144, 2015.
[29] J. R. Regalbuto, "Cellulosic Biofuels—Got Gasoline?," 2011.
[30] Energy Economics Applied Optimization, "an Introduction To Petroleum Refining and the Production of Ultra Low Sulfur Gasoline," pp. 1–33, 2011.
[31] A. Corma, O. Delatorre, and M. Renz, "High-quality diesel from hexose- and pentose-derived biomass platform molecules," *ChemSusChem*, vol. 4, pp. 1574–1577, 2011.
[32] G. W. Huber, S. Iborra, and A. Corma, "Synthesis of transportation fuels from biomass: Chemistry, catalysts, and engineering," *Chem. Rev.*, vol. 106, pp. 4044–4098, 2006.
[33] G. Li, N. Li, J. Yang, A. Wang, X. Wang, Y. Cong, and T. Zhang, "Synthesis of renewable diesel with the 2-methylfuran, butanal and acetone derived from lignocellulose," *Bioresour. Technol.*, vol. 134, pp. 66–72, 2013.
[34] B. Pholjaroen, N. Li, J. Yang, G. Li, W. Wang, A. Wang, Y. Cong, X. Wang, and T. Zhang, "Production of Renewable Jet Fuel Range Branched Alkanes with Xylose and Methyl Isobutyl Ketone," 2014.
[35] L. Faba, E. Díaz, and S. Ordóñez, "One-pot Aldol Condensation and Hydrodeoxygenation of Biomass-derived Carbonyl Compounds for Biodiesel Synthesis," *ChemSusChem*, pp. 2816–2820, 2014.
[36] Q.-N. Xia, Q. Cuan, X.-H. Liu, X.-Q. Gong, G.-Z. Lu, and Y.-Q. Wang, "Pd/NbOPO 4 Multifunctional Catalyst for the Direct Production of Liquid Alkanes from Aldol Adducts of Furans," *Angew. Chemie*, vol. 126, no. 37, pp. 9913–9918, 2014.
[37] A. Corma, O. De La Torre, M. Renz, and N. Villandier, "Production of high-

quality diesel from biomass waste products," *Angew. Chemie - Int. Ed.*, vol. 50, no. 10, pp. 2375–2378, 2011.
[38] G. Li, N. Li, Z. Wang, C. Li, A. Wang, X. Wang, Y. Cong, and T. Zhang, "Synthesis of high-quality diesel with furfural and 2-methylfuran from hemicellulose," *ChemSusChem*, vol. 5, pp. 1958–1966, 2012.
[39] J. Yang, N. Li, G. Li, W. Wang, A. Wang, X. Wang, Y. Cong, and T. Zhang, "Solvent-free synthesis of C10 and C11 branched alkanes from furfural and methyl isobutyl ketone," *ChemSusChem*, vol. 6, pp. 1149–1152, 2013.
[40] F. Chen, N. Li, S. Li, J. Yang, F. Liu, W. Wang, A. Wang, Y. Cong, X. Wang, and T. Zhang, "Solvent-free synthesis of C9 and C10 branched alkanes with furfural and 3-pentanone from lignocellulose," *Catal. Commun.*, vol. 59, pp. 229–232, 2015.
[41] J. Q. Bond, A. a. Upadhye, H. Olcay, G. a. Tompsett, J. Jae, R. Xing, D. M. Alonso, D. Wang, T. Zhang, R. Kumar, A. Foster, S. M. Sen, C. T. Maravelias, R. Malina, S. R. H. Barrett, R. Lobo, C. E. Wyman, J. a. Dumesic, and G. W. Huber, "Production of renewable jet fuel range alkanes and commodity chemicals from integrated catalytic processing of biomass," *Energy Environ. Sci.*, vol. 7, no. 4, p. 1500, 2014.
[42] I. Yati, M. Yeom, J.-W. Choi, H. Choo, D. J. Suh, and J.-M. Ha, "Water-promoted selective heterogeneous catalytic trimerization of xylose-derived 2-methylfuran to diesel precursors," *Appl. Catal. A Gen.*, vol. 495, pp. 200–205, 2015.
[43] C. Wen, E. Barrow, J. Hattrick-Simpers, and J. Lauterbach, "One-step production of long-chain hydrocarbons from waste-biomass-derived chemicals using bi-functional heterogeneous catalysts," *Phys. Chem. Chem. Phys.*, vol. 16, no. 7, pp. 3047–3054, 2014.
[44] N. Ota, M. Tamura, Y. Nakagawa, K. Okumura, and K. Tomishige, "Hydrodeoxygenation of vicinal OH groups over heterogeneous rhenium catalyst promoted by palladium and ceria support," *Angew. Chemie - Int. Ed.*, vol. 54, no. 6, pp. 1897–1900, 2015.
[45] X. Li, D. Wu, T. Lu, G. Yi, H. Su, and Y. Zhang, "Highly efficient chemical process to convert mucic acid into adipic acid and DFT studies of the mechanism of the rhenium-catalyzed deoxydehydration," *Angew. Chemie - Int. Ed.*, vol. 53, no. 16, pp. 4200–4204, 2014.
[46] Y. Nakagawa, S. Liu, M. Tamura, and K. Tomishige, "Catalytic Total Hydrodeoxygenation of Biomass-Derived Polyfunctionalized Substrates to Alkanes," *ChemSusChem*, vol. 8, no. 7, pp. 1114–1132, 2015.
[47] J. R. Dethlefsen and P. Fristrup, "Rhenium-catalyzed deoxydehydration of diols and polyols," *ChemSusChem*, vol. 8, no. 5, pp. 767–775, 2015.
[48] N. Li and G. W. Huber, "Aqueous-phase hydrodeoxygenation of sorbitol with Pt/SiO2-Al2O3: Identification of reaction intermediates," *J. Catal.*, vol. 270, no. 1, pp. 48–59, 2010.
[49] Y. Amada, N. Ota, M. Tamura, Y. Nakagawa, and K. Tomishige, "Selective hydrodeoxygenation of cyclic vicinal diols to cyclic alcohols over tungsten oxide-palladium catalysts," *ChemSusChem*, vol. 7, no. 8, pp. 2185–2192, 2014.
[50] Y. Takeda, T. Shoji, H. Watanabe, M. Tamura, Y. Nakagawa, K. Okumura, and K. Tomishige, "Selective hydrogenation of lactic acid to 1,2-propanediol over highly

active ruthenium-molybdenum oxide catalysts," *ChemSusChem*, vol. 8, no. 7, pp. 1170–1178, 2015.
[51] N. Ota, M. Tamura, Y. Nakagawa, K. Okumura, and K. Tomishige, "Performance, Structure, and Mechanism of ReO_x–Pd/CeO_2 Catalyst for Simultaneous Removal of Vicinal OH Groups with H_2," *ACS Catal.*, vol. 6, no. 5, pp. 3213–3226, 2016.
[52] B. MacQueen, E. Barrow, G. Rivera Castro, Y. Pagan-Torres, A. Heyden, and J. Lauterbach, "Optimum Reaction Conditions for 1,4-Anhydroerythritol and Xylitol Hydrodeoxygenation over a ReOx-Pd/Ceo2 Catalyst via Design of Experiments," *Ind. Eng. Chem. Res.*
[53] X. Huang, B. Wang, E. A. Grulke, and M. J. Beck, "Toward tuning the surface functionalization of small ceria nanoparticles," *J. Chem. Phys.*, vol. 140, no. 7, 2014.
[54] Y. Xi, W. Yang, S. C. Ammal, J. Lauterbach, Y. Pagan Torres, and A. Heyden, "Mechanistic study of the ceria supported, Re-catalyzed deoxydehydration of vicinal OH groups," *Catal. Sci. Technol.*, no. 1, 2018.
[55] I. R. Beattie, T. R. Gilson, and P. J. Jones, "Vapor Phase Vibrational Spectra for Re(2)O(7) and the Infrared Spectrum of Gaseous HReO(4). Molecular Shapes of Mn(2)O(7), Tc(2)O(7), and Re(2)O(7).," *Inorg. Chem.*, vol. 35, no. 5, pp. 1301–1304, 1996.
[56] R. A. Johnson, M. T. Rogers, and G. E. Leroi, "Vibrational Spectra of Ammonium and Other Scheelite-Type Perrhenates," *J. Chem. Phys.*, vol. 56, no. 2, pp. 789–792, 1972.
[57] F. D. Hardcastle, I. E. Wachs, J. A. Horsley, and G. H. Via, "The structure of surface rhenium oxide on alumina from laser raman spectroscopy and x-ray absorption near-edge spectroscopy," *J. Mol. Catal.*, vol. 46, no. 1–3, pp. 15–36, 1988.
[58] M. A. Vuurman, D. J. Stufkens, A. Oskam, and I. E. Wachs, "Structural determination of surface rhenium oxide on various oxide supports (Al2O3, ZrO2, TiO2 and SiO2)," *J. Mol. Catal.*, vol. 76, pp. 263–285, 1992.
[59] B. M. Weckhuysen, J.-M. Jehng, and I. E. Wachs, "In Situ Raman Spectroscopy of Supported Transition Metal Oxide Catalysts: $^{18}O_2 - {}^{16}O_2$ Isotopic Labeling Studies," *J. Phys. Chem. B*, vol. 104, no. 31, pp. 7382–7387, 2000.
[60] S. Lwin, C. Keturakis, J. Handzlik, P. Sautet, Y. Li, A. I. Frenkel, and I. E. Wachs, "Surface ReOxsites on Al2O3and their molecular structure-reactivity relationships for olefin metathesis," *ACS Catal.*, vol. 5, no. 3, pp. 1432–1444, 2015.
[61] Rigaku, "X-ray diffraction." [Online]. Available: https://www.rigaku.com/en/techniques/xrd.
[62] H. Konno, "Chapter 8 - X-ray Photoelectron Spectroscopy," in *Materials Science and Engineering of Carbon*, Scienc Direct Topics, 2016, pp. 153–171.
[63] "x-Ray Photoelectron Spectroscopy (XPS)," *Kratos analytical: Surface Analysis Techniques*. [Online]. Available: https://www.kratos.com/applications/techniques/x-ray-photoelectron-spectroscopy.
[64] J. Moulder, *Handbook of X-ray Photoelectron Spectroscopy*. Perkin-Elmer Corporation, 1992.
[65] H. Kosslick, G. Lischke, B. Parlitz, W. Storek, and R. Fricke, "Acidity and active

sites of Al-MCM-41," *Appl. Catal. A Gen.*, vol. 184, no. 1, pp. 49–60, 1999.
[66] S. Brunauer, P. H. Emmett, and E. Teller, "Adsorption of Gases in Multimolecular Layers," *J. Am. Chem. Soc.*, vol. 60, no. 2, pp. 309–319, 1938.
[67] E. P. Barrett, L. G. Joyner, and P. P. Halenda, "The Determination of Pore Volume and Area Distributions in Porous Substances. I. Computations from Nitrogen Isotherms," *J. Am. Chem. Soc.*, vol. 73, no. 1, pp. 373–380, 1951.
[68] B. Williams and C. Carter, *Transmission Electron Microscopy*. Springer Science & Business Media, 2009.
[69] B. Hafner, "Energy Dispersive Spectroscopy on the SEM: A Primer," *Characterization Facility: University of Minnesota-Twin Cities*. [Online]. Available: http://www.charfac.umn.edu/instruments/eds_on_sem_primer.pdf.
[70] L. H. J. Lajunen and P. Peramaki, *Spectrochemical Analysis by Atomic Absorption and Emission*, 2nd ed. Royal Society of Chemistry, 2007.
[71] S. Kim, E. Sasmaz, and J. Lauterbach, "Effect of Pt and Gd on coke formation and regeneration during JP-8 cracking over ZSM-5 catalysts," *Appl. Catal. B Environ.*, vol. 168–169, pp. 212–219, 2015.
[72] K. Nakamoto, *[No Title]*. 2009.
[73] G. W. Roberts, *The influence of mass and heat transfer on the performance of heterogeneous catalysts in gas/liquid/solid systems*. Elsevier Inc., 1976, pp. 1–48.
[74] V. Meille, C. de Bellefon, and D. Schweich, "Kinetics of α-Methylstyrene Hydrogenation on Pd/Al $_2$ O $_3$," *Ind. Eng. Chem. Res.*, vol. 41, no. 7, pp. 1711–1715, 2002.
[75] P. R. Gogate, A. a. C. M. Beenackers, and A. B. Pandit, "Multiple-impeller systems with a special emphasis on bioreactors: A critical review," *Biochem. Eng. J.*, vol. 6, no. 2, pp. 109–144, 2000.
[76] J. Oldshue, *Fluid Mixing Technology*. McGraw-Hill Publications Co, 1983.
[77] E. Paul, V. Atiemo-Obeng, and S. Kresta, *Handbook of Industrial Mixing: Science and Practice*. John Wiley & Sons, 2004.
[78] C. J. Barrett, J. N. Chheda, G. W. Huber, and J. a. Dumesic, "Single-reactor process for sequential aldol-condensation and hydrogenation of biomass-derived compounds in water," *Appl. Catal. B Environ.*, vol. 66, no. 1–2, pp. 111–118, 2006.
[79] M. Burgener, R. Furrer, T. Mallat, and A. Baiker, "Hydrogenation of citral over Pd/alumina: Comparison of 'supercritical' CO2and conventional solvents in continuous and batch reactors," *Appl. Catal. A Gen.*, vol. 268, no. 1–2, pp. 1–8, 2004.
[80] H. Jeong, T. H. Kim, K. I. Kim, and S. H. Cho, "The hydrogenation of maleic anhydride to γ-butyrolactone using mixed metal oxide catalysts in a batch-type reactor," *Fuel Process. Technol.*, vol. 87, no. 6, pp. 497–503, 2006.
[81] J. P. Mikkola and T. Salmi, "Three-phase catalytic hydrogenation of xylose to xylitol - prolonging the catalyst activity by means of on-line ultrasonic treatment," *Catal. Today*, vol. 64, no. 3–4, pp. 271–277, 2001.
[82] T. Mahmud, J. N. Haque, K. J. Roberts, D. Rhodes, and D. Wilkinson, "Measurements and modelling of free-surface turbulent flows induced by a magnetic stirrer in an unbaffled stirred tank reactor," *Chem. Eng. Sci.*, vol. 64, no. 20, pp. 4197–4209, 2009.

[83] S. Vernuccio, P. R. Von Rohr, and J. Medlock, “General Kinetic Modeling of the Selective Hydrogenation of 2-Methyl-3-butyn-2-ol over a Commercial Palladium-Based Catalyst,” *Ind. Eng. Chem. Res.*, vol. 54, no. 46, pp. 11543–11551, 2015.
[84] G. Ertl, H. Knozinger, F. Schuth, and J. Weitkamp, Eds., *Handbook of Heterogeneous Catalysis*. Wiley.
[85] S. Sakata, Y. Kamiya, Y. Yoshinaga, T. Okuhara, and R. Ohnishi, “Zirconium Phosphate with a High Surface Area as a Water-Tolerant Solid Acid,” *Catal. Letters*, vol. 94, no. 1/2, pp. 45–47, 2004.
[86] N. Gorodylova, P. Šulcová, M. Bosacka, and E. Filipek, “DTA-TG and XRD study on the reaction between ZrOCl2·8H2O and (NH4)2HPO4 for synthesis of ZrP2O7,” *J. Therm. Anal. Calorim.*, vol. 118, no. 2, pp. 1095–1100, 2014.
[87] J. Guo, H. Lou, H. Zhao, X. Wang, and X. Zheng, “Novel synthesis of high surface area MgAl2O4 spinel as catalyst support,” *Mater. Lett.*, vol. 58, no. 12–13, pp. 1920–1923, 2004.
[88] L. N. Stepanova, O. B. Belskaya, M. O. Kazakov, and V. a. Likholobov, “Use of platinum carbonyl complexes in the synthesis of Pt/MgAlO x catalysts,” *Kinet. Catal.*, vol. 54, no. 4, pp. 505–510, 2013.
[89] E. Sasmaz, C. Wang, M. J. Lance, and J. Lauterbach, “In situ spectroscopic investigation of a Pd local structure over Pd/CeO2 and Pd/MnOx–CeO2 during CO oxidation,” *J. Mater. Chem. A*, vol. 5, no. 25, pp. 12998–13008, 2017.
[90] N. Ota, M. Tamura, Y. Nakagawa, K. Okumura, and K. Tomishige, “Performance, Structure, and Mechanism of ReOx-Pd/CeO2Catalyst for Simultaneous Removal of Vicinal OH Groups with H2,” *ACS Catal.*, vol. 6, no. 5, pp. 3213–3226, 2016.
[91] A. J. Schwanke, C. W. Lopes, and S. B. C. Pergher, “Synthesis of Mesoporous Material from Chrysotile-Derived Silica,” *Mater. Sci. Appl.*, vol. 04, no. 08, pp. 68–72, 2013.
[92] C. Y. Chen, S. Q. Xiao, and M. E. Davis, “Studies on ordered mesoporous materials III. Comparison of MCM-41 to mesoporous materials derived from kanemite,” *Microporous Mater.*, vol. 4, no. 1, pp. 1–20, 1995.
[93] J. Čejka, A. Corma, and S. Zones, *Zeolites and Catalysis: Synthesis, Reactions and Applications*, vol. 1–2. 2010.
[94] A. Corma, “Acidity and Stability of MCM-41 Crystalline Aluminosilicates,” *J. Catal.*, vol. 148, no. 2, pp. 569–574, 1994.
[95] P. Horcajada, a. Rámila, J. Pérez-Pariente, and M. Vallet-Regí, “Influence of pore size of MCM-41 matrices on drug delivery rate,” *Microporous Mesoporous Mater.*, vol. 68, no. 1–3, pp. 105–109, 2004.
[96] P. T. Fanson, M. R. Horton, W. N. Delgass, and J. Lauterbach, “FTIR analysis of storage behavior and sulfur tolerance in barium-based NOχstorage and reduction (NSR) catalysts,” *Appl. Catal. B Environ.*, vol. 46, no. 2, pp. 393–413, 2003.
[97] A. Corma, O. de la Torre, and M. Renz, “Production of high quality diesel from cellulose and hemicellulose by the Sylvan process: catalysts and process variables,” *Energy Environ. Sci.*, vol. 5, p. 6328, 2012.
[98] I. Yati, M. Yeom, J.-W. Choi, H. Choo, D. J. Suh, and J.-M. Ha, “Water-promoted selective heterogeneous catalytic trimerization of xylose-derived 2-methylfuran to diesel precursors,” *Appl. Catal. A Gen.*, vol. 495, pp. 200–205, 2015.
[99] D. Tzoulaki, A. Jentys, J. Pérez-Ramírez, K. Egeblad, and J. A. Lercher, “On the

location, strength and accessibility of Bronsted acid sites in hierarchical ZSM-5 particles," *Catal. Today*, vol. 198, no. 1, pp. 3–11, 2012.
[100] Y. Zhao, Y. Fu, and Q. X. Guo, "Production of aromatic hydrocarbons through catalytic pyrolysis of γ-valerolactone from biomass," *Bioresour. Technol.*, vol. 114, pp. 740–744, 2012.
[101] M. Milina, S. Mitchell, Z. Trinidad, D. Verboekend, and J. Perez-Ramirez, "Decoupling porosity and compositional effects on desilicated ZSM-5 zeolites for optimal alkylation performance," *Catal. Sci. Technol.*, vol. 2, pp. 759–766, 2012.
[102] R. Karinen, K. Vilonen, and M. Niemelä, "Biorefining: Heterogeneously catalyzed reactions of carbohydrates for the production of furfural and hydroxymethylfurfural," *ChemSusChem*, vol. 4, no. 8, pp. 1002–1016, 2011.
[103] W. G. Norris and L. C. Krisher, "Microwave Spectrum of 2-Methylfuran," *J. Chem. Phys.*, vol. 51, no. 1, pp. 403–406, 1969.
[104] D. H. Olson, G. T. Kokotallo, S. L. Lawton, and W. M. Meier, "Crystal Structure and Structure-Related Properties of," *Am. Chem. Soc.*, vol. 85, pp. 2238–2243, 1981.
[105] C. J. H. Jacobsen, C. Madsen, J. Houzvicka, I. Schmidt, and A. Carlsson, "Mesoporous zeolite single crystals [2]," *J. Am. Chem. Soc.*, vol. 122, no. 29, pp. 7116–7117, 2000.
[106] M. A. Harmer and Q. Sun, "Solid acid catalysis using ion-exchange resins," *Appl. Catal. A Gen.*, vol. 221, no. 1–2, pp. 45–62, 2001.
[107] E. Furimsky, "Catalytic hydrodeoxygenation," *Appl. Catal. A Gen.*, vol. 199, pp. 147–190, 2000.
[108] Q. N. Xia, Q. Cuan, X. H. Liu, X. Q. Gong, G. Z. Lu, and Y. Q. Wang, "Pd/NbOPO4 multifunctional catalyst for the direct production of liquid alkanes from aldol adducts of furans," *Angew. Chemie - Int. Ed.*, pp. 9755–9760, 2014.
[109] J. Dawody, M. Skoglundh, L. Olsson, and E. Fridell, "Sulfur deactivation of Pt/SiO2, Pt/BaO/Al2O3, and BaO/Al2O3 NOx storage catalysts: Influence of SO2 exposure conditions," *J. Catal.*, vol. 234, no. 1, pp. 206–218, 2005.
[110] J. Wang, L. M. Huang, H. Y. Chen, and Q. Z. Li, "Acid function of Al-MCM-41 supported platinum catalysts in hydrogenation of benzene, toluene and o-xylene," *Catal. Letters*, vol. 55, no. 3–4, pp. 157–163, 1998.
[111] K. C. Park, D. J. Yim, and S. K. Ihm, "Characteristics of Al-MCM-41 supported Pt catalysts: Effect of Al distribution in Al-MCM-41 on its catalytic activity in naphthalene hydrogenation," *Catal. Today*, vol. 74, no. 3–4, pp. 281–290, 2002.
[112] X. Zhu, L. L. Lobban, R. G. Mallinson, and D. E. Resasco, "Bifunctional transalkylation and hydrodeoxygenation of anisole over a Pt/HBeta catalyst," *J. Catal.*, vol. 281, no. 1, pp. 21–29, 2011.
[113] Z. Paál, P. Tétényi, D. Prigge, X. Z. Wang, and G. Ertl, "Study of morphology and composition of Pt-black catalysts III. XPS study of Pt-black," *Appl. Surf. Sci.*, vol. 14, no. 3–4, pp. 307–320, Mar. 1983.
[114] Z. Zhang, Y. Han, L. Zhu, R. Wang, Y. Yu, S. Qiu, D. Zhao, and F. S. Xiao, "Strongly acidic and high-temperature hydrothermally stable mesoporous aluminosilicates with ordered hexagonal structure," *Angew. Chemie - Int. Ed.*, vol. 40, no. 7, pp. 1258–1262, 2001.
[115] R. Mokaya, "Al Content Dependent Hydrothermal Stability of Directly

Synthesized Aluminosilicate MCM-41," *J. Phys. Chem. B*, vol. 104, no. 34, pp. 8279–8286, 2000.
[116] M. Käldström, N. Kumar, T. Heikkilä, M. Tiitta, T. Salmi, and D. Y. Murzin, "Transformation of levoglucosan over H-MCM-22 zeolite and H-MCM-41 mesoporous molecular sieve catalysts," *Biomass and Bioenergy*, vol. 35, no. 5, pp. 1967–1976, 2011.
[117] A. S. Amarasekara, T. B. Singh, E. Larkin, M. A. Hasan, and H. J. Fan, "NaOH catalyzed condensation reactions between levulinic acid and biomass derived furan-aldehydes in water," *Ind. Crops Prod.*, vol. 65, pp. 546–549, 2015.
[118] G. Liang, A. Wang, X. Zhao, N. Lei, and T. Zhang, "Selective aldol condensation of biomass-derived levulinic acid and furfural in aqueous-phase over MgO and ZnO," *Green Chem.*, vol. 18, pp. 3430–3438, 2016.
[119] A. Jain, S. P. Ong, G. Hautier, W. Chen, W. D. Richards, S. Dacek, S. Cholia, D. Gunter, D. Skinner, G. Ceder, and K. a. Persson, "The Materials Project: A materials genome approach to accelerating materials innovation," *APL Mater.*, vol. 1, no. 1, p. 11002, 2013.
[120] A. L. Patterson, "The scherrer formula for X-ray particle size determination," *Phys. Rev.*, vol. 56, no. 10, pp. 978–982, 1939.
[121] R. Nakamura, F. Abe, and E. Echigoya, "Structures of Rhenium (VII) Oxides on alumina and their Catalytic Activities for Metathesis of Olefins," *Chem. Soc. Japan*, pp. 51–54, 1981.
[122] P. Arnoldy, E. M. Oers, van, O. S. L. Bruinsma, de V. H. J. Beer, and J. A. Moulijn, "Temperature-programmed reduction of Al2O3-, SiO2-, and carbon-supported Re2O7 catalysts," *J. Catal.*, vol. 93, pp. 231–245, 1985.
[123] B. J. Tielsch and J. E. Fulghum, "Differential Charging in XPS. Part I: Demonstratio of Lateral Charging in a Bulk Insulator Using Imaging XPS," *Surf. Interface Anal.*, vol. 24, no. August 1995, pp. 28–33, 1996.
[124] D. S. Kim and I. E. Wachs, "Surface Rhenium Oxide-Support Interaction for supported Re2O7 catalysts." pp. 419–429, 1993.
[125] J. Okal, L. Kępiński, L. Krajczyk, and W. Tylus, "Oxidation and redispersion of a low-loaded Re/γ-Al2O3catalyst," *J. Catal.*, vol. 219, no. 2, pp. 362–371, 2003.
[126] I. E. Wachs, "Raman and IR studies of surface metal oxide species on oxide supports: Supported metal oxide catalysts," *Catal. Today*, vol. 27, no. 3–4, pp. 437–455, 1996.
[127] H. Lacheen, P. Cordeiro, and E. Iglesia, "Isolation of Rhenium and ReOx Species within ZSM5 Channels and their Catalytic Function in the Activation of Alkanes and Alkanols," *Chem. - A Eur. J.*, vol. 13, pp. 3048–3057, 2007.
[128] M. Saidy, M. Y. Zhou, and K. A. R. Mitchell, "Tensor LEED analysis for the Ni (111) - (√7×√7) R19 . 1 ° -P surface structure: Comparison with Other √7 Systems," *Surf. Interface Anal.*, vol. 28, no. November 1998, pp. 84–91, 1999.
[129] K. Asakura, S. Konishi, T. Ohta, Y. Kitajima, and H. Kuroda, "EXAFS Studies on the Adsorption Structures of P / Ni (111)," *Jpn. J. Appl. Phys.*, vol. 32, pp. 359–361, 1993.
[130] J. S. Kane and J. H. Reynolds, "Mass Spectrometer Study of the Vapors from Red Phosphorus and Arsenic," *J. Chem. Phys.*, vol. 25, no. 2, pp. 342–349, 1956.
[131] "Stanley MBE rp.pdf." .

[132] M. Susa, K. Kawagishi, N. Tanaka, and K. Nagata, “Diffusion Mechanism of Phosphorus from Phosphorous Vapor in Amorphous Silicon Dioxide Film Prepared by Thermal Oxidation,” *J. Electrochem. Soc.*, vol. 144, no. 7, pp. 2552–2558, 1997.
[133] B. W. Hooton, “The deposition of thin films of red phosphorus,” *Nucl. Instruments Methods*, vol. 27, no. 3, p. 338, 1964.
[134] M. J. Mondry, E. J. Caine, and H. Kroemer, “A GaP decomposition source for producing a dimer phosphorus molecular beam free of gallium and tetramer phosphorus,” *J. Vac. Sci. Technol. A Vacuum, Surfaces, Film.*, vol. 3, no. 2, p. 316, 1985.
[135] K. E. J. Goh, L. Oberbeck, M. J. Butcher, N. J. Curson, F. J. Rueß, and M. Y. Simmons, “Comparison of GaP and PH3 as dopant sources for STM-based device fabrication,” *Nanotechnology*, vol. 18, no. 6, p. 65301, 2007.
[136] J. D. Song, J. M. Kim, and Y. T. Lee, “Molecular Beam Epitaxial Growth of High-Quality InP / InGaAs / InP Heterostructure with Polycrystalline GaAs and GaP Decomposition Sources,” *Jpn. J. Appl. Phys.*, vol. 39, no. 4, pp. L347–L350, 2000.
[137] H. Künzel, J. Böttcher, P. Harde, and R. Maessen, “MBE growth of high-quality InP for GaInAs/InP heterostructures using incongruent evaporation of GaP,” *J. Cryst. Growth*, vol. 175, pp. 175–1762, 1997.
[138] F. X. Xiu, Z. Yang, L. J. Mandalapu, J. L. Liu, and W. P. Beyermann, “P-type ZnO films with solid-source phosphorus doping by molecular-beam epitaxy,” *Appl. Phys. Lett.*, vol. 88, no. 5, pp. 1–3, 2006.
[139] T. Shitara and K. Eberl, “Electronic properties of InGaP grown by solid-source molecular-beam epitaxy with a GaP decomposition source,” *Appl. Phys. Lett.*, vol. 65, no. 3, pp. 356–358, 1994.
[140] N. B. Goodman, L. Ley, and D. W. Bullet, “Valence-band structures of phosphorus allotropes,” *Phys. Rev. B*, vol. 27, no. 12, pp. 7440–4750, 1983.
[141] V. I. Nefedov, Y. V. Salyn, E. P. Domashevskaya, Y. A. Ugai, and V. A. Terekhov, “A STUDY BY XPS AND XRS OF THE PARTICIPATION IN CHEMICAL BONDING OF THE 3d ELECTRONS OF COPPER, ZINC AND GALLIUM,” *J. Electron Spectros. Relat. Phenomena*, vol. 6, pp. 231–238, 1975.
[142] M. Kiskinova and D. W. Goodman, “MODIFICATION OF CHEMISORPTION PROPERTIES BY ELECTRONEGATIVE ADATOMS: H2 AND CO ON CHLORIDED, SULFIDED, AND PHOSPHIDED Ni(100),” *Surf. Sci.*, vol. 108, pp. 64–76, 1981.
[143] G. A. Somorjai, *Introduction to Surface Chemistry and Catalysis*. New York, USA: Wiley Interscience, 1993.
[144] L.-Q. Wang, Z. Hussain, Z. . Huang, A. E. Schach von Wittenau, D. W. Lindle, and D. A. Shirley, “Surface Structure of √ 3x √ 3R 30 Cl / Ni (111) Determined Using Low-temperature Angle- Resolved-Photoemission Extended Fine Structure,” *Phys. Rev. B*, vol. 44, no. 111, pp. 13711–13719, 1991.
[145] W. Erley and H. Wagner, “Chlorine adsorption on Ni(111),” *Surf. Sci.*, vol. 66, no. 1, pp. 371–375, 1977.
[146] Y. Takata, H. Sato, S. Yagi, T. Yokoyama, T. Ohta, and Y. Kitajima, “Site-selective adsorption of Cl atoms on Ni(111) studied by back-reflection x-ray standing-wave method,” *Surf. Sci.*, vol. 265, no. 1, pp. 111–117, 1992.

[147] M. Funabashi, T. Yokoyama, Y. Takata, T. Ohta, Y. Kitajima, and H. Kuroda, "Surface structure of Cl/Ni(111) determined by surface EXAFS spectroscopy and soft X-ray standing-wave method," *Surf. Sci.*, vol. 242, no. 1–3, pp. 59–64, 1991.
[148] Y. K. Wu and K. A. R. Mitchell, "A refined LEED structural determination for the surface designated Ni (111)-(2 x 2)-S," *Can. J. Chem*, vol. 67, pp. 1975–1979, 1989.
[149] D. R. Warburton, P. L. Wincott, G. Thornton, F. M. Quinn, and D. Norman, "Incorporation of sulphur into the (111) surface of nickel?," *Surf. Sci.*, vol. 211, pp. 71–81, 1989.
[150] T. Fauster, H. Dürr, and D. Hartwig, "Determination of the geometry of Sulphur on Nickel surfaces by low-energy ion scattering," *Surf. Sci.*, vol. 178, no. 1, pp. 657–666, 1986.
[151] D. A. Andrews and D. P. Woodruff, "The local adsorption site for sulphur on Ni {111} in the low coverage lattice gas," *Surf. Sci.*, vol. 141, no. 1, pp. 31–39, 1984.
[152] T. W. Capehart, C. W. Seabury, G. W. Graham, and T. N. Rhodin, "Coverage dependent adsorption site for sulfur on Ni(111)," *Surf. Sci.*, vol. 120, no. 2, pp. L441–L446, 1982.
[153] P. M. Marcus, J. E. Demuth, and D. W. Jepsen, "Determination of the structure of ordered adsorbed layers by analysis of LEED spectra," *Surf. Sci.*, vol. 53, no. 1, pp. 501–522, 1975.
[154] J. E. Demuth, D. W. Jepsen, and P. M. Marcus, "Crystallographic Dependence of Chemisorption Bonding for Sulfur on (001), (110),and (111)Nickel," *Phys. Rev. Lett.*, vol. 32, no. 21, pp. 1182–1185, 1974.
[155] D. E. Gardin, J. D. Batteas, M. A. Van Hove, and G. A. Somorjai, "Carbon, nitrogen, and sulfur on Ni(111) : formation of complex structures and consequences for molecular decomposition," *Surf. Sci.*, vol. 296, no. 1, pp. 25–35, 1993.
[156] Y. Kitajima, T. Yokoyama, T. Ohta, M. Funabashi, N. Kosugi, and H. Kuroda, "SURFACE EXAFS AND XANES STUDIES OF (5√3 × 2)S/Ni(111): A PSEUDO-c(2 × 2)S/Ni(100) MODEL WITH SURFACE RECONSTRUCTION," *Surf. Sci. Lett.*, vol. 214, pp. L261–L269, 1989.
[157] M. Yamada, H. Hirashima, and A. Kitada, "Three-Ni-atom cluster formed by sulfer asorption on Ni(111)," *Surf. Sci.*, vol. 602, pp. 1659–1668, 2008.
[158] M. Zharnikov, M. Weinelt, and P. Zebisch, "Holography of clean and sulfer-covered Ni(111)using multiple wave number photoelectron diffraction patterns," *Surf. Sci.*, no. 334, pp. 114–134, 1995.
[159] V. Maurice, N. Kitakatsu, and M. Siegers, "Low-coverage sulfur induced reconstrction of Ni(111)," *Surf. Sci.*, vol. 373, pp. 307–317, 1997.
[160] D. R. Mullins, D. R. Huntley, and S. H. Overbury, "The nature of the sulfur induced surface reconstruction on Ni(111)," *Surf. Sci.*, vol. 323, no. 1–2, pp. L287–L292, 1995.
[161] W. Erley and H. Wagner, "Sulfur poisoning of carbon monoxide adsorption on Ni(111)," *J. Catal.*, vol. 53, no. 3, pp. 287–294, 1978.
[162] P. Delescluse and A. Masson, "Diffuse scattering in RHEED induced by linear disorders of sulphur segregated on nickel (111) surface," *Surf. Sci.*, vol. 100, no. 2, pp. 423–438, 1980.

[163] Y.-S. Ku and S. H. Overbury, “Structure analysis of S adsorbed on Ni(111) by low energy Li+ ion scattering,” *Surf. Sci.*, vol. 276, no. 1, pp. 262–272, 1992.
[164] L. Ruan, I. Stensgaard, F. Besenbacher, and E. Lægsgaard, “Observation of a Missing-Row Structure on an fcc (111) Surface: The (5√3 x 2)S Phase on Ni(111) Studied by Scanning Tunneling Microscopy,” *Phys. Rev. Lett.*, vol. 71, no. 18, pp. 2963–2966, 1993.
[165] S. Rundqvist, “X-ray Investigations of Mn3P, Mn2P, and Ni2P,” *Acta Chem Scand.*, vol. 16, pp. 992–998, 1962.
[166] S. T. Oyama, “Novel catalysts for advaced hydroprocessing: transition metal phosphides,” *J. Catal.*, vol. 216, pp. 343–352, 2003.
[167] W. Robinson, J. Van Gestel, T. Koranyi, and S. Eijsbouts, “Phosphorus promotion of Ni(Co)-containing Mo-free catalysts in quinoline hydrodenitrogenation,” *J. Catal.*, vol. 161, pp. 539–550, 1996.
[168] X. Wang, P. Clark, and S. T. Oyama, “Synthesis, characterization, and hydrotreating activity of several iron group transition metal phosphides,” *J. Catal.*, vol. 208, pp. 321–331, 2002.
[169] K. Li, R. Wang, and J. Chen, “Hydrodeoxygenation of anisole over silica-supported Ni2P, MoP, and NiMoP catalysts,” *Energy Fuels*, vol. 25, pp. 854–863, 2011.
[170] V. Goncalves, P. de Souza, and T. Cabioc’h, “Effects of P/Ni ratio on the performance of nickel phosphide phases supported on zirconia for the hydrodeoxygenation of m-cresol,” *Catal. Commun.*, 2018.
[171] A. Berenguer, T. Sankaranarayanan, and G. Gomez, “Evaluation of transition metal phosphides supported on ordered mesoporous materials as catalysts for phenol hydrodeoxygenation,” *Green Chem.*, vol. 18, pp. 1938–1951, 2016.
[172] V. Goncalves, P. de Souza, and V. da Silva, “Kinetics of the hydrodeoxygenation of cresol isomers over Ni2P/SiO2: proposals of nature of deoxygenation active sites based on an experimental study,” *Appl. Catal. B Environ.*, vol. 205, pp. 357–367, 2017.
[173] Y. Shi and B. Zhang, “Recent advances in transition metal phosphide nanomaterials: synthesis and applicaitons in hydrogen evolution reaction,” *Chem. Soc. Rev.*, vol. 45, pp. 1529–1541, 2016.
[174] E. Popczun, J. McKone, and C. Read, “Nanostructured nickel phosphide as an electrocatalyst for the hydrogen evolution reaction,” *J. Am. Chem. Soc.*, vol. 135, pp. 9267–9270, 2013.
[175] T. Kawai, K. Bando, and Y. Lee, “EXAFS measurements of a working catalyst in the liquid phase: an in situ study of a Ni2P hydrodesulfurization catalyst,” *J. Catal.*, vol. 241, pp. 20–24, 2006.
[176] K. Bando, T. Wanda, and T. Miyamoto, “Combined in situ QXAFS and FTIR analysis of a Ni phosphide catalyst under hydrodesulfurization conditions,” *J. Catal.*, vol. 286, pp. 165–171, 2012.
[177] T. Wada, K. Bando, and T. Miyamoto, “Operando QEXAFS studies of Ni2P during thiopene hydrodesulfurization: direct observation of Ni-S bond formation under reaction conditions,” *J. Synchrotron Radiat.*, vol. 19, pp. 205–209, 2012.
[178] T. Wada, K. Bando, and S. Oyama, “Operando observation of Ni2P structural changes during catalytic reaction: effect of H2S pretreatment,” *Chem. Lett.*, vol.

41, pp. 1238–1240, 2012.
[179] K. Edamoto, H. Inomata, and T. Shimada, “Valence and core-level photoelectron spectroscopy study of the electronic structure of Ni2P(0001),” *e-Journal Surf. Sci. Nanotechnol.*, vol. 7, no. 1, 2009.
[180] K. Edamoto, H. Inomata, and N. Yasuno, “Angle resolved and rosonant photoelectron spectroscopy study of Ni2P (101b0),” *Hyomen Kagaku*, vol. 31, p. 324, 2010.
[181] S. Suzuki, G. M. Moula, T. Miyamoto, Y. Nakagawa, K. Kinshthita, K. Asakura, S. T. Oyama, and S. Otani, “Scanning Tunneling Microscopy and Photoemission Electron Microscopy Studies on Single Crystal Ni2P Surfaces,” *J. Nanosci. Nanotechnol.*, vol. 9, no. 1, pp. 195–201, 2009.
[182] K. Edamoto, Y. Nakadai, and H. Inomata, “Soft XPS study of Ni2P(0001),” *Solid State Commun.*, vol. 148, no. 135, 2008.
[183] H. Ariga, M. Kawashima, and S. Takakusagi, “Density functional theoretical investigation on the Ni3PP structure and its hydrogen adsorption property of Ni2P(0001) surface,” *Chem. Lett.*, vol. 42, pp. 1481–1483, 2013.
[184] M. G. Moula, S. Suzuki, W.-J. Chun, S. Otani, S. T. Oyama, and K. Asakura, “The First Atomic-scale Observation of a Ni_2P(0001) Single Crystal Surface,” *Chem. Lett.*, vol. 35, no. 1, pp. 90–91, 2006.
[185] P. Liu, J. Rodriquez, T. Asakura, and J. Gomes, “Desulfurization reactions on Ni2P(0001) and a-Mo2C(001) surfaces: complex role of P and C sites,” *J. Phys. Chem. B*, vol. 109, p. 4575, 2005.
[186] A. Hernandez, H. Ariga, S. Takakusagi, K. Kinoshita, S. Suzuki, S. Otani, S. T. Oyama, and K. Asakura, “Dynamical LEED Analysis of Ni2P (0001)-1x1: Evidence for P-covered Surface Structure,” *Chem. Phys. Lett.*, vol. 513, pp. 48–52, 2011.
[187] D. Guo, Y. Nakagawa, and H. Ariga, “STM studies on the reconstruction of the Ni2P ($10\bar{1}0$) surface,” *Surf. Sci.*, vol. 604, pp. 1347–1352, 2010.
[188] K. Edamoto, H. Inomata, and O. K, “Electronic structure of the Ni2P(101b0) surface: angle-resolved photoemission study,” *Solid State Commun.*, vol. 150, pp. 1120–1123, 2010.
[189] S. Imanishi, S. Munakata, and Y. Kakefuda, “Characterization of Ni2P(10-10): soft X-ray photoelectron spectroscopy study,” *e-Journal Surf. Sci. Nanotechnol.*, vol. 10, pp. 45–49, 2012.
[190] K. Kinoshita, G. Simon, T. Konig, and M. Heyde, “A Scanning Tunneling Microscopy Observation of ($\sqrt{3}\times\sqrt{3}$) R30° Reconstructed Ni2P(0001),” *Jpn. J. Appl. Phys.*, vol. 47, pp. 6088–6091, 2008.
[191] Q. Yuan, H. Ariga, and K. Asakura, “An investigation of Ni2p single crystal surfaces; structure, electronic state and reactivity,” *Top. Catal.*, vol. 58, pp. 194–200, 2015.
[192] J. Contreras-Mora, H. Ariga-Miwa, S. Takakusagi, C. T. Williams, and K. Asakura, “Phosphorous Diffusion Through Ni_2P—Low Energy Diffusion Path and Its Unique Local Structure,” *J. Phys. Chem. C*, vol. 122, no. 11, pp. 6318–6322, 2018.
[193] K. Herman and M. Van Hove, “LEEDpat 4.2,” 2014. [Online]. Available: http://www.fhi-berlin.mpg.de/KHsoftware/LEEDpat/.

[194] G. Ertl, J. Küppers, and R. L. Park, “ Low-Energy Electrons and Surface Chemistry ,” *Phys. Today*, vol. 29, no. 3, pp. 57–57, 2009.
[195] M. Saidy and K. A. R. Mitchell, “Tensor LEED analysis for the Cu(111)-(√7 × √7)R19.1°-S surface structure,” *Surf. Sci.*, vol. 441, no. 2–3, pp. 425–435, 1999.
[196] Y. Kitajima, T. Yokoyama, Y. Takata, S. Ninama, A. Mishra, M. C. Feiters, A. Longo, D. Banerjee, K. Namikawa, S. Hosoya, A. Mishra, P. Singh, Z. Wu, K. Nakamura, S. Honda, T. Fujikawa, and S. Usami, “Surface Structure of (√7×√7) R19.1°S/Cu(111) Studied by Surface EXAFS and Back-Reflection X-Ray Standing-Wave Method,” *Jpn. J. Appl. Phys*, vol. 32, pp. 377–379, 1993.
[197] W. Liu, K. C. Wong, and K. A. R. Mitchell, “LEED crystallographic analysis for the Rh(111)-(√7 × √7)R19.1 degrees-P surface structure,” *Surf. Sci.*, vol. 372, no. 1–3, pp. 312–322, 1997.
[198] W. Liu, K. C. Wong, and K. A. R. Mitchell, “Novel Surface Structure: Rh(111)-(√7 × √7)R19.1.degree.-P,” *J. Am. Chem. Soc.*, vol. 117, no. 49, pp. 12344–12345, 2005.
[199] A. Shard, V. Dhanak, and C. Muryn, “SEXAFS and NIXSW investigation of the Rh(111)-(√7 × √7)R19.1-P surface,” *Surf. Sci.*, vol. 433–435, pp. 267–271, 1999.
[200] J. Forbes, A. Gellman, and J. Dunphy, “Imaging of sulfur overlayer structures on the Pd(111) surface,” *Surf. Sci.*, vol. 279, pp. 68–78, 1992.
[201] M. Grillo, C. Stampfl, and W. Berndt, “Low-energy electron-diffraction analysis of the (√7 × √7)R19.1°-S adsorbate structure on the Pd(111) surface,” *Surf. Sci.*, vol. 317, pp. 84–98, 1994.
[202] T. Ohta, Y. Kitajima, P. Stefan, M. S. Stefan, N. Kosugi, and H. Kuroda, “SURFACE EXAFS AND XANES STUDIES OF S / Ni (110) AND S / Ni (111),” *J. Phys. Colloq.*, vol. 47, no. 110, pp. C8-503-C8-508, 1986.

APPENDIX A

PERMISSION TO REPRINT

Chapter 7 is a reprint of a manuscript accepted by Science and Technology of Advanced Materials. This journal is an open access journal published by Taylor & Francis.